Aalto University
School of Science and Technology
Faculty of Electronics, Communications and Automation

Kimmo Karaste

Spin-on siloxane polymers in image sensor applications

Master’s Thesis

Espoo, February 16th, 2010

Supervisor: Professor Seppo Honkanen

Instructor: Ph.D. Juha Rantala

Aalto University
School of Science and Technology

Aalto University School of Science and Technology Faculty of Electronics, Communications and Automation Degree programme of Electronics		ABSTRACT OF THE MASTER'S THESIS
Author: Kimmo Karaste		
Title: Spin-on siloxane polymers in image sensor applications		
Number of pages: 88	Date: 16.2.2010	Language: English
Professorship: Micro and Nanosciences		Code: S-104
Supervisor: Professor Seppo Honkanen		
Instructor(s): Ph.D. Juha Rantala		

Abstract: The feasibility of siloxane based spin-on polymers in a complementary metal oxide semiconductor (CMOS) image sensor application is studied in this thesis. After an introduction to the fundamental characteristics of light and how it behaves when propagating in matter and through interfaces, the basic operation principles of the most commonly used modern image sensors are reviewed. The experimental part of the thesis will demonstrate the improvements achieved in image sensor performance when replacing conventional dielectrics with siloxane based polymers having specifically tuned refractive indices. Results from optical modeling as well as measurement data from fully functional devices are used to demonstrate the enhanced device performance. Silecs' high refractive index spin-on polymers are shown to significantly improve the quantum efficiency and reduce crosstalk of a small pixel size image sensor utilizing a lightpipe structure. Up to 24% quantum efficiency and 19% crosstalk improvement was achieved in an IBM 2.2 µm pixel size sensor when comparing to a conventional structure. Silecs' low refractive index polymer films used as passivation and anti-reflection coatings on the image sensor microlens array were also studied. Lower reflectance from the microlens surface was achieved by properly tuning the overcoat film thickness and refractive index. Additionally, the overcoat provides mechanical protection to the soft microlens material which can result in improved manufacturing yield. Finally, photosensitized siloxane polymers are demonstrated to yield excellent photopatternability with using industry standard lithographic techniques thus simplifying the device process flow and increasing wafer throughput.

Keywords: CMOS image sensor, spin-on, polymer, lightpipe, pixel

Aalto-yliopisto
Teknillinen korkeakoulu

Aalto-yliopisto Teknillinen korkeakoulu Elektroniikan, tietoliikenteen ja automaation tiedekunta Elektroniikan- ja sähkötekniikan tutkinto-ohjelma		DIPLOMITYÖN TIIVISTELMÄ
Tekijä: Kimmo Karaste		
Työn nimi: Siloksaanipohjaisten spin-on polymeerien käyttö kuvakennojen valmistuksessa		
Sivumäärä: 88	Päiväys: 16.2.2010	Julkaisukieli: Englanti
Professuuri: Mikro- ja Nanotekniikka		Professuurikoodi: S-104
Työn valvoja: Professori Seppo Honkanen		
Työn ohjaaja(t): FT Juha Rantala		

Tiivistelmä: Tässä työssä esitellään siloksaani-pohjaisten spin-on polymeerien tuomia etuja CMOS-kuvakennojen toimintaan. Ensimmäisessä osassa tutustutaan valon perusominaisuuksiin ja kuinka se käyttäytyy kulkiessaan väliaineessa sekä rajapintojen yli. Lisäksi käydään läpi nykyisin yleisimmin käytössä olevien kuvakennojen toimintaa sekä rakennetta. Työn kokeellisessa osuudessa tullaan osoittamaan mitä etuja siloksaani-pohjaisilla polymeereillä on kennojen valmistuksessa tavallisesti käytettyihin eristekerroksiin verrattuna. Työn aikana tutkittiin erityisesti Silecsin valmistamien korkean taitekertoimen spin-on polymeerikalvojen soveltuvuutta kennon valokanavarakenteeseen. Parannukset erityisesti pieniä pikseleitä hyödyntävien CMOS-kuvakennojen kvanttihyötysuhteeseen sekä pikselien väliseen ylikuulumiseen havainnollistetaan sekä optisen mallinnuksen että käytännön mittausten avulla. IBM:n 2.2 μm pikselikoon CMOS-kuvakennossa saavutettiin valokanavarakenteen avulla 24% parannus kvanttihyötysuhteessa ja 19% parannus ylikuulumisessa. Lisäksi työssä arvioidaan matalan taitekertoimen omaavien polymeerikalvojen soveltuvuutta kennojen passivointiin ja heijastuksenestoon. Havaittiin, että mikrolinssin pinnasta syntyviä heijastuksia pystyttiin merkittävästi vähentämään säätämällä kalvon paksuus ja taitekerroin sovellukseen sopivaksi. Lopuksi havainnollistetaan suorakuvioitavien polymeerien tuomia etuja kennon valmistusprosessiin.

Asiasanat: CMOS-kuvakenno, spin-on, polymeeri, valokanava, pikseli

Preface

This thesis was done in conjunction with Silecs' spin-on polymer material development for image sensor applications.

I would like to thank Dr. Juha Rantala for the opportunity to work in the field of spin-on polymers and guidance over the years. His support and comments during the writing of this thesis are also greatly appreciated. I thank Professor Seppo Honkanen for supervising the progress of this thesis and William Martin for providing assistance with linguistic matters.

Special thanks to all the Silecs co-workers, present and past, for the inspiration.

Kimmo Karaste

Espoo, 16.2.2010

Table of Contents

PREFACE IV
TABLE OF CONTENTS V
SYMBOLS AND ABBREVIATIONS VII
1 INTRODUCTION 1
2 ELECTROMAGNETIC RADIATION 2
3 LIGHT AT PLANE INTERFACES 4
3.1 THE REFRACTIVE INDEX AND REFRACTION OF LIGHT 4
3.2 REFLECTANCE 7
3.2.1 Anti-reflection coatings 9
4 INTERACTION OF LIGHT WITH MATTER 13
4.1 RAYLEIGH AND MIE SCATTERING 13
4.2 ABSORPTION AND DISPERSION 14
5 PROPAGATION OF LIGHT IN OPTICAL FIBERS 16
6 DETECTION OF LIGHT 19
6.1 THE PHOTOELECTRIC EFFECT 19
6.2 SILICON-BASED TECHNOLOGIES FOR LIGHT DETECTION 20
7 THE DIGITAL CAMERA 23
7.1 IMAGE SENSORS IN DIGITAL IMAGING 23
7.1.1 The charge coupled device 25
7.1.2 CMOS image sensor 28
7.2 COLOR SEPARATION AND LIGHT FOCUSING 30
7.3 IMAGE SENSOR PERFORMANCE 32
7.3.1 Sensitivity and spectral response 32
7.3.2 Noise 34
7.3.3 Crosstalk between pixels 34
8 RECENT DEVELOPMENTS IN MODERN CMOS IMAGE SENSORS 36
8.1 PIXEL DOWNSCALING 36
8.2 DIELECTRIC STACK OPTIMIZATION 39
8.3 BACKSIDE ILLUMINATION 40
8.4 LIGHTPIPE ARCHITECTURE 42
9 OPTICAL MODELING OF CMOS IMAGE SENSORS 46
9.1 THE LIGHTPIPE STRUCTURE 46
9.2 MICROLENS OVERCOAT LAYER 52

10 SILOXANE POLYMERS IN OPTICAL APPLICATIONS 54

10.1 FUNDAMENTALS OF SILOXANE POLYMERS 54
10.2 SILECS HIGH REFRACTIVE INDEX POLYMERS 56
10.3 SILECS POLYMERS IN CIS LIGHTPIPE APPLICATION 58
10.3.1 Quantum efficiency and angular response measurements 58

11 MICROLENS OVERCOAT LAYER 64

11.1 ANTI-REFLECTION COATING 64
11.2 SILECS SPIN-ON OVERCOAT MATERIALS 66
11.3 PHOTOPATTERNABLE OVERCOAT 70

12 STABILITY OF POLYMER FILMS 74

13 SUMMARY 78

14 CONCLUSIONS 81

REFERENCES 83

Symbols and abbreviations

Symbols

a	fiber core radius [m]
c	speed of light ~ 3×10^8 [m/s]
CT	crosstalk [%]
d	optical thickness [m]
E_{ph}	photon energy [eV]
f	frequency [Hz]
$f/\#$	f-number
h	Planck's constant ~ 6.626×10^{-34} [J*s]
n	refractive index
NA	numerical aperture
r	reflection coefficient
r_{TE}	reflection coefficient for transverse electric polarized light
r_{TM}	reflection coefficient for transverse magnetic polarized light
R	reflectance
R_{TE}	reflectance for transverse electric polarized light
R_{TM}	reflectance for transverse magnetic polarized light
S	time-averaged Poynting vector
$S^{(inc)}$	time-averaged Poynting vector of the incident field
V	V-number
α_{max}	maximum acceptance angle [°]
ε_r	relative permittivity
η	collection efficiency [%]
θ_c	critical angle [°]
θ_i	angle of incidence [°]
θ_t	angle of refraction [°]
λ	wavelength [m]
v	speed of light in matter [m/s]

Abbreviations

AFM	atomic force microscopy
APS	active pixel sensor
ARC	anti-reflection coating
BCCD	buried channel charge coupled device
BPSG	borophosphosilicate glass
BSI	backside illuminated
CCD	charge coupled device
CCM	conventional camera module

CFA	color filter array
CIS	CMOS image sensor
CMOS	complementary metal oxide semiconductor
CMP	chemical mechanical polishing
CSCM	chip scale camera module
CTE	coefficient of thermal expansion
CVD	chemical vapor deposition
DSLR	digital single lens reflex
FDTD	finite difference time domain
FFTCCD	full-frame transfer charge coupled device
FPN	fixed pattern noise
FSI	front side illuminated
FTCCD	frame transfer charge coupled device
FTIR	fourier transform infrared spectroscopy
FTIR	frustrated total internal reflection
HSQ	hydrogen silsesquioxane
ILD	interlayer dielectric
IR	infrared
ITCCD	interline transfer charge coupled device
ITO	indium tin oxide
ITRS	international technology roadmap for semiconductors
LCD	liquid crystal display
LED	light emitting diode
LP	linearly polarized
MOS	metal oxide semiconductor
MSQ	methyl silsesquioxane
NIR	near-infrared
OLPF	optical low pass filter
PCB	printed circuit board
PECVD	plasma enhanced chemical vapor deposition
PMMA	polymethylmethacrylate
PPS	passive pixel sensor
RMS	root mean square
SCCD	surface channel charge coupled device
SEM	scanning electron microscope
SNR	signal-to-noise ratio
SOI	silicon-on-insulator
STI	shallow trench isolation
TE	transverse electric
TEM	tunneling electron microscope
TEOS	tetraethyl orthosilicate
TM	transverse magnetic
TMAH	tetramethylammonium hydroxide

TIR	total internal reflection
TSV	through silicon via
UV	ultraviolet

1 Introduction

An increasing number of consumer and industrial electronics applications, such as mobile phones, webcams and security cameras, require digital imaging capability. This demand has led the way for rapid development of the CMOS image sensor (CIS) which is now challenging the traditionally used charged coupled device (CCD) also in high end digital still cameras. To increase image resolution, the pixel size has been significantly reduced during the past decade but as the dimensions approach the wavelength of light, several problems such as reduced sensitivity and increased crosstalk have emerged as it has become increasingly difficult for the light to reach the image sensor's photoactive area due to diffraction limitations and device geometry related issues. A vast amount of research has been conducted to address the problem and some significant improvements have recently been made in small pixel sensor performance.

This thesis will introduce the reader to the fundamental phenomenon related to the propagation of light and to the basic operation of modern image sensors. The CMOS image sensor and the effects of pixel downscaling will be addressed with more detail along with the structural modifications used to improve the device performance. Silecs' siloxane based spin-on polymers are introduced and the advantages they can offer to the image sensor performance are presented by reviewing both optical simulation and actual measurement results from fully functional devices.

2 Electromagnetic radiation

The natural phenomenon of electromagnetic radiation has found many uses in a wide range of modern applications. Microwave ovens, cellular phones, televisions, x-ray machines, radars among others all use electromagnetic radiation of different wavelengths to transmit information or energy from one place to the other. The visible spectrum of the electromagnetic radiation between 400 to 700 nm wavelengths is perhaps the easiest to understand due to the sensitivity of the human eye at that range. In fact, the highest sensitivity of the eye lies at just above 500 nm which coincidentally is also where the Sun's radiation reaches its peak intensity. Figure 2-1 shows the full electromagnetic spectrum ranging from gamma rays to microwaves. The corresponding color for each wavelength in the visible range is also illustrated. [1, 2]

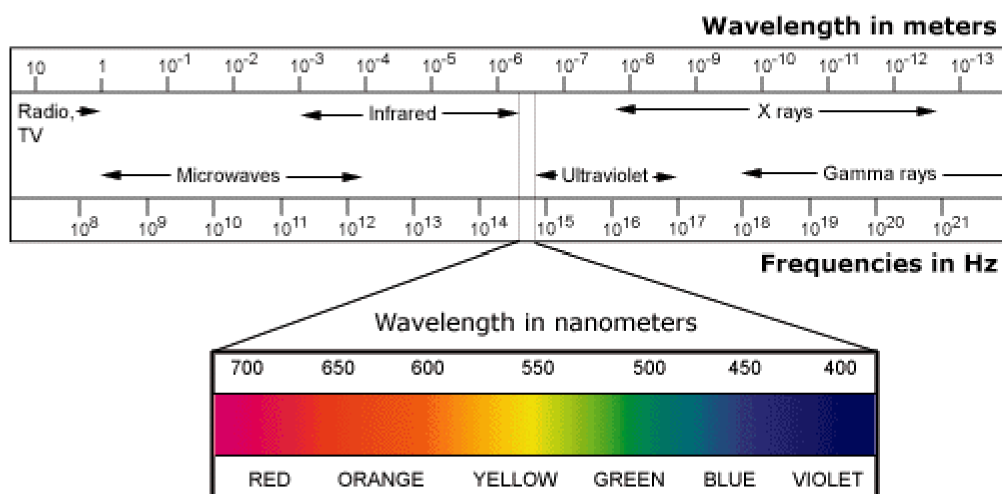

Figure 2-1. The electromagnetic spectrum [3].

An electromagnetic wave in its simplest form is a plane wave with varying electric and magnetic fields traveling through free space. It can be either transverse electric (TE) or transverse magnetic (TM) polarized depending on how the electric and magnetic field components are positioned relative to the plane of incidence. The electromagnetic wave carries energy within itself which can be seen as light or detected as a radio signal depending on the wavelength. The Poynting vector is often used to describe the energy flow per unit time and unit area and irradiance or intensity is used to describe its magnitude. This is the classical view of electromagnetic radiation but light has also a particle nature which is used to describe many of its fundamental properties. The particle nature of light can be

understood by thinking of light as a collection of photons. Photons are massless particles carrying electromagnetic energy which move at the speed of light in vacuum and were originally introduced to explain the photoelectric effect. The photoelectric effect and how it relates to image sensors will be discussed in more detail in Chapter 6. The classical electromagnetic theory relies on Maxwell's equations which have been used to mathematically explain the propagation of light and how it behaves at interfaces of two dissimilar materials. Although a detailed analysis of Maxwell's equations is beyond the scope of this work, it is noteworthy to mention that many of the laws presented in the following chapters have originated from them. [1, 2, 24]

3 Light at plane interfaces

The behavior of electromagnetic waves at interfaces is of great importance in understanding how light can be manipulated by various optical layers. Some of the basic phenomenon such as reflection, refraction, scattering and absorption are introduced in this chapter.

3.1 The refractive index and refraction of light

The refractive index, given by Equation 3.1, is a measure of how much the speed of light in a medium is reduced compared to the speed of light in a vacuum.

$$n = \frac{c}{v} = \sqrt{\varepsilon_r} \ , \tag{3.1}$$

where n is the refractive index, c is the speed of light in a vacuum, v is the speed of light in the medium and ε_r the relative permittivity.

Since the speed of light in a vacuum is constant, light must travel slower in optically denser materials, i.e. materials with a higher refractive index. The refractive index is wavelength dependent and typically decreases as a function of wavelength in the visible spectrum of light for most dielectric materials. For non-transparent or absorbing materials, such as metals, the refractive index is given in complex form where the real and imaginary parts represent the refractive index and extinction coefficient, respectively. The extinction coefficient k is directly related to the absorption coefficient of the material. Equation 3.1 also shows the connection between the refractive index and the relative permittivity or dielectric constant. As both refractive index and dielectric constant are wavelength dependent, the relationship is applicable only when quoting values at the same wavelength.

When crossing an interface between materials with dissimilar refractive indices, the frequency of light remains constant but the wavelength changes. This condition satisfies Equation 3.2 which shows the relationship between wavelength λ and frequency f.

$$\lambda = \frac{c}{f} \tag{3.2}$$

As can be seen from Equations 3.1 and 3.2, light not only travels slower in an optically denser material but it also has a shorter wavelength compared to free space.

Consider light arriving at an interface of two materials with dissimilar refractive indices ($n_1 < n_2$) as depicted in Figure 3-1.

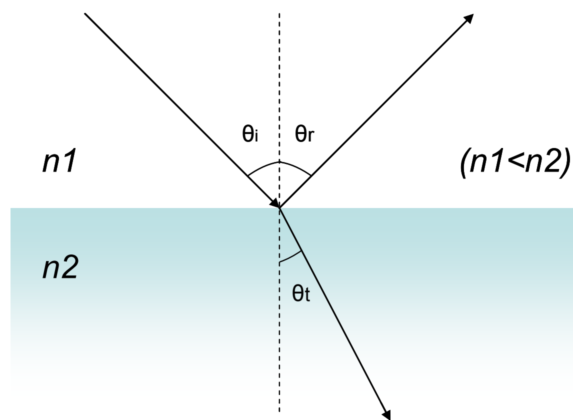

Figure 3-1. Light incident on a plane interface with $n_1 < n_2$.

According to the law of reflection, the angle of incidence is identical to the angle of reflection. The angle of the refracted or transmitted ray θ_t can be calculated using Snell's law.

$$n_1 \sin\theta_i = n_2 \sin\theta_t, \qquad (3.3)$$

where n_1 and n_2 are the refractive indices of the two mediums forming the interface, θ_i is the angle of incidence and θ_t the angle of refraction.

For example, when light traveling in air (n_1 = 1.003) reaches a glass sheet surface (n_2 = 1.5) with angle of incidence θ_i = 35.0°, the transmitted wave refracts according to Snell's law and continues to propagate through the glass surface with an angle θ_t = 22.5°. The angle of the reflected wave is identical to the incident wave as noted earlier. Since the refractive index varies with wavelength, the angle of refraction is also wavelength dependent. This is most commonly seen in prisms where white light is dispersed into different spectral components as the angle of refraction is different for each wavelength or color.

Snell's law applies also when light traveling in an optically denser material crosses an interface to an optically less dense material ($n_1 > n_2$). In this case certain angles of incidence can however lead to total internal reflection (TIR) where the wave is not transmitted across the interface and all light is reflected as shown in Figure 3-2 (a). For this to happen, the angle of incidence must be equal to or greater than the critical angle θ_c, which is given by Equation 3.4.

$$\sin\theta_c = \frac{n_2}{n_1} \tag{3.4}$$

Total internal reflection is widely used in many applications for guiding light along optical fibers and waveguides. The higher refractive index material where light is confined in is typically called a core while the outer layer with lower refractive index is called a cladding. In some cases, especially when dimensions approach the wavelength of light, it is important to take into account that an evanescent wave travels parallel to the interface where total internal reflection occurs. Suppose another layer of material with refractive index n_1, for example, is placed within close proximity to the n_1/n_2 interface, it is possible that light escapes from the high refractive index layer even if the incident angle exceeds the critical angle. This phenomenon, illustrated in Figure 3-2 (b), is called frustrated total internal reflection (FTIR). [1, 2]

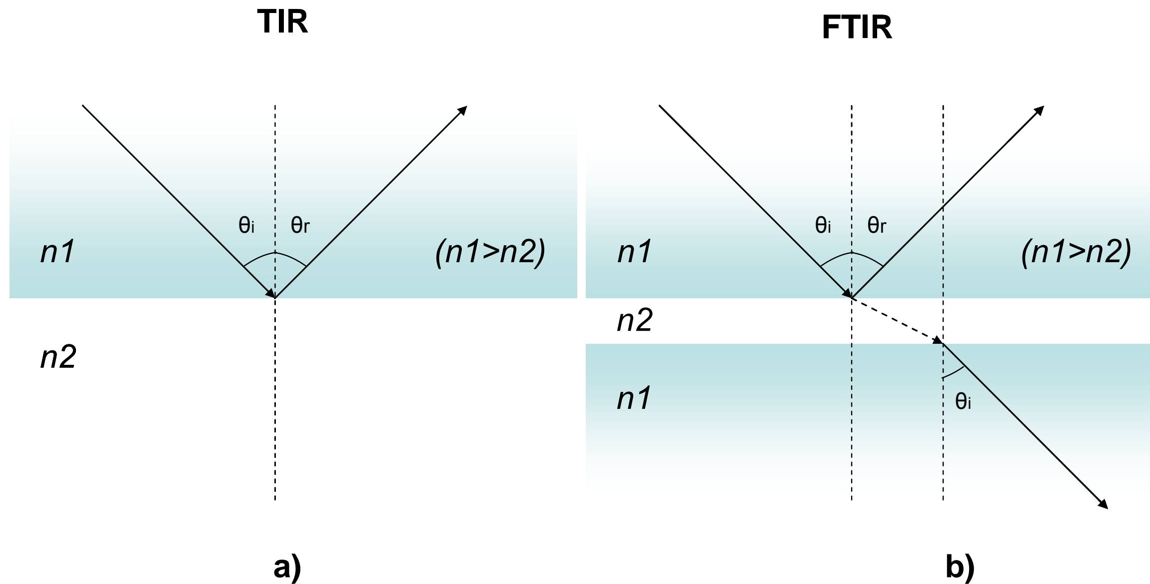

Figure 3-2. Ray tracing illustration of a) total internal reflection and b) frustrated total internal reflection.

Since the amplitude and intensity of the evanescent wave fall off exponentially with distance, the evanescent field typically extends only to approximately one wavelength away from the interface where total internal reflection occurs. Therefore the thickness of layer n_2 in Figure 3-2 (b) has to be very thin to allow light to escape or tunnel across it.

3.2 Reflectance

The amount of light reflected from a given surface depends on the polarization of light, the angle of incidence and the refractive indices n_1 and n_2. Fresnel's equations for calculating the reflectance for TE and TM polarizations are shown below in Equations 3.5 and 3.6, respectively.

$$R_{TE} = \left|r_{TE}\right|^2 = \left|\frac{n_1 \cos\theta_i - n_2 \cos\theta_t}{n_1 \cos\theta_i + n_2 \cos\theta_t}\right|^2 \tag{3.5}$$

$$R_{TM} = \left|r_{TM}\right|^2 = \left|\frac{n_2 \cos\theta_i - n_1 \cos\theta_t}{n_1 \cos\theta_t + n_2 \cos\theta_i}\right|^2 \tag{3.6}$$

At normal incidence where both θ_i and θ_t are zero, Equations 3.5 and 3.6 simplify for both polarizations into Equation 3.7.

$$R = \left|r\right|^2 = \frac{(n_1 - n_2)^2}{(n_1 + n_2)^2} \tag{3.7}$$

Figure 3-3 shows the reflectance as a function of incident angle when light propagating in air is reflected from a glass surface. Equations 3.5 and 3.6 were used in the calculations.

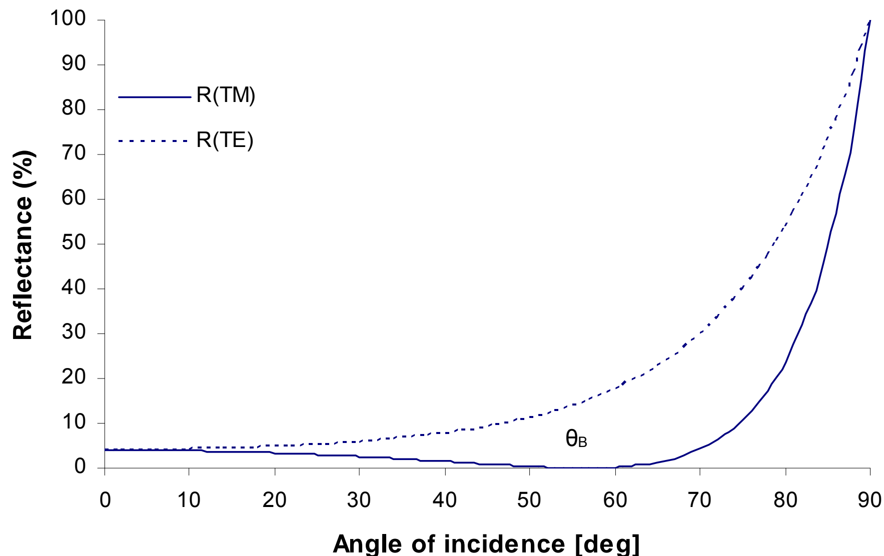

Figure 3-3. Reflectance in an air-glass interface (n_1 = 1, n_2 = 1.5).

As can be seen from Figure 3-3, the reflectance increases with the angle of incidence for TE polarized light. For TM polarized light the reflectance first decreases and reaches zero at the so called Brewster's angle and then starts to rapidly increase. At Brewster's angle (56° in this case), all of the TM polarized light is transmitted through the air-glass interface since reflectance is zero. This phenomenon can be used, for instance, to separate the two polarizations with consecutively placed glass plates inclined at Brewster's angle. TM polarized light will pass the plates unaffected if absorption is neglected, while the TE polarized light will eventually vanish due to reflection losses at each interface.

Figure 3-4 shows the reflectance as a function of angle of incidence for a glass-air interface. Similarly, there is an angle where reflectance reaches zero for the TM polarized wave. The sudden increase in reflectance for both polarizations at angles greater than approximately 42° is due to total internal reflection. [1, 2]

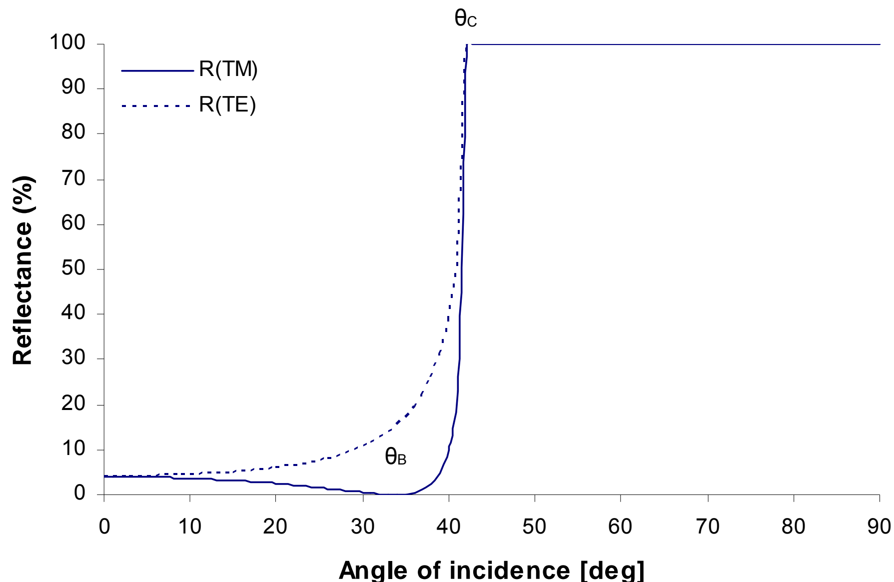

Figure 3-4. Reflectance in a glass-air interface (n_1 = 1.5, n_2 = 1).

When light reflects from a smooth surface, as in the above examples, it is called specular reflection. Diffuse reflection on the other hand occurs when light is reflected from rough surfaces. The law of reflection still applies for diffuse reflections but due to surface roughness the reflected light is scattered in many different directions. Glossy and matt paints are good examples where specular and diffuse reflections can be seen.

3.2.1 Anti-reflection coatings

Anti-reflection coatings (ARC) are used in many applications to minimize reflections from a surface. When the refractive index of the coating material is chosen so that it is lower than the refractive index of the surface layer but higher than the refractive index of the medium where light is incident from, reflectance is reduced. For example, the reflectance of light traveling in air normally incident on a glass surface (n_2 = 1.5) has a reflectance of 4.0% according to Equation 3.7. If a layer of magnesium fluoride with a refractive index of 1.38 is coated on top of the glass surface the reflectance is reduced. From the air-MgF_2 and MgF_2-glass interfaces the reflectances are 2.5% and 0.2% respectively, summing to a total reflectance of only 2.7%. To further minimize the reflectance, single layer ARC films can take advantage of destructive interference which occurs when light reflected from the ARC film and from the bottom layer surfaces are out of phase by exactly half a wavelength or 180°. This can be achieved by coating the surface where reflections are to be minimized with a low refractive index film which has an optical thickness of exactly one quarter of a wavelength or a multiple of it. The optical thickness *d* of a quarter wavelength thick film depends on the material's refractive index and can be calculated with using Equation 3.8.

$$d = \frac{\lambda_0}{4n_1}, \tag{3.8}$$

where λ_0 is the wavelength of light in a vacuum and n_1 the refractive index of the anti-reflection coating.

The destructive interference between two waves with 180° phase difference is illustrated in Figure 3-5.

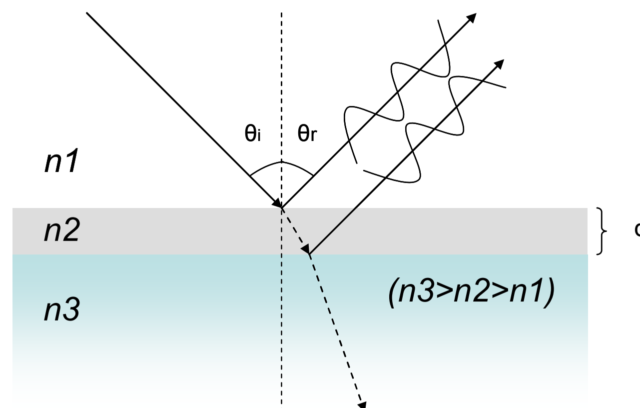

Figure 3-5. Destructive interference between reflected waves.

When light reflects from layer n_2 with a higher refractive index it undergoes a phase shift of 180°. If the thickness of the ARC film is one quarter of a wavelength, the wave reflecting from surface n_3 experiences a phase shift of half a wavelength and travels a half a wavelength longer distance than the wave reflected from the ARC layer surface. The reflected waves are then out of phase by 180° and interfere destructively. If the amplitudes of the reflected waves are equal they cancel each other completely and all incident light is transmitted into layer n_3. The general solution for calculating the reflectance for light which is normally incident when using a quarter wavelength thick single layer anti-reflective coating is given by Equation 3.9.

$$R = |r|^2 = \frac{\left(n_2 - n_1^{\,2}\right)^2}{\left(n_2 + n_1^{\,2}\right)^2}, \qquad (3.9)$$

where n_2 and n_1 are the substrate and ARC refractive indices, respectively.

From Equation 3.9 it can be seen that if the refractive index of the ARC layer is the square root of the substrate's refractive index, reflectance will be zero. Using Equations 3.8 and 3.9 the optimum anti-reflective coating for 550 nm light normally incident on a glass substrate (n = 1.5) can be calculated to be a 113 nm thick with a refractive index of 1.22. Figures 3-6 and 3-7 show reflectance as a function of angle of incidence when light is incident from air to glass and from glass to air with using the optimum ARC layer to suppress reflections. Reflectance without an anti-reflective coating is also shown for reference. For low angles of incidence, the quarter wavelength thick ARC layer with a refractive index of 1.22 reduces the reflectance very effectively compared to the case where no ARC is used.

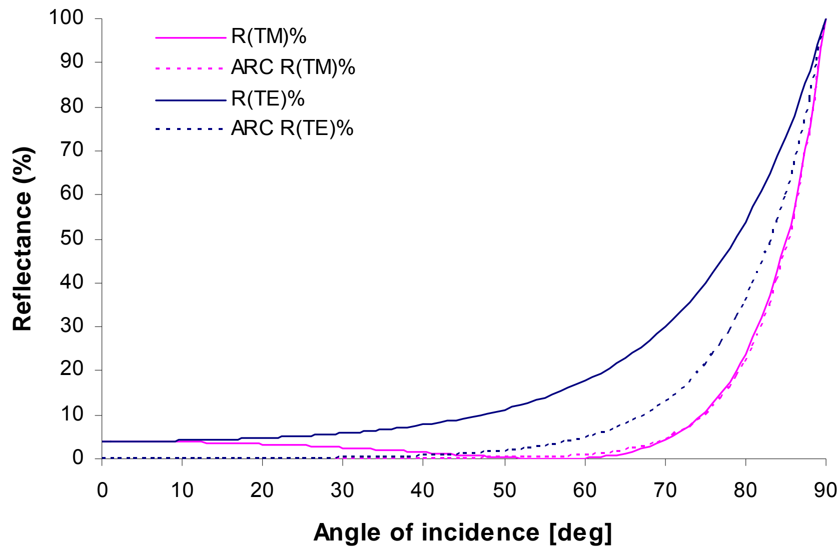

Figure 3-6. Reflectance for 550 nm light in air-glass interface with and without an anti-reflective coating (n_1 = 1, n_2 =1.22, n_3 = 1.5, ARC thickness = 113 nm).

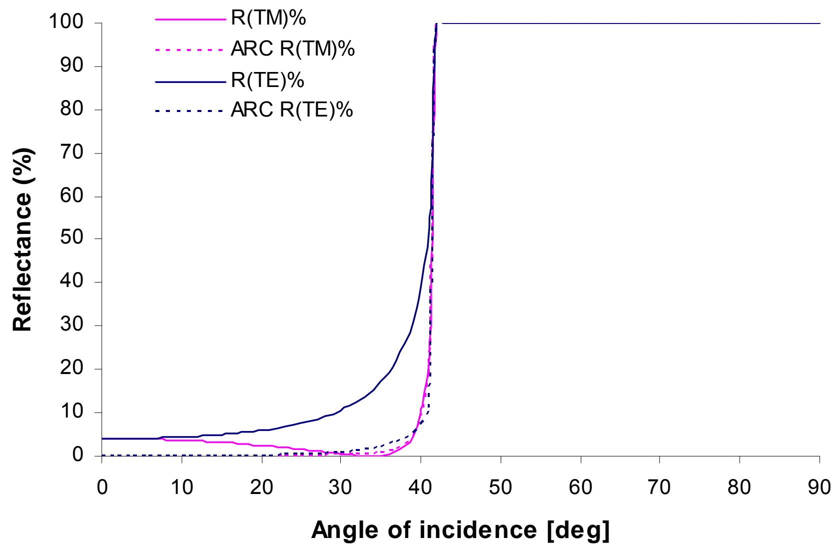

Figure 3-7. Reflectance for 550 nm light in glass-air interface with and without an anti-reflective coating (n_1 = 1.5, n_2 =1.22, n_3 = 1.0, ARC thickness = 113 nm).

The same principle can be used to design highly reflective coatings, but in this case the reflected waves have to be in matching phase for constructive interference to occur.

The difficulty with single layer anti-reflective coatings is that they can be designed to give zero reflectance only for a certain wavelength. Also finding a suitable material with a refractive index of exactly the square root of the substrate's refractive index can be challenging, if not impossible. Multiple layer anti-reflective coatings with alternating high and low refractive index layers can be used to increase the bandwidth for which the reflectance is minimized. These multilayer coatings are often called Bragg gratings but they are beyond the scope of this work and will not be discussed in detail. [1, 2, 7, 8]

4 Interaction of light with matter

As light travels through matter it interacts with the atoms and molecules creating electric dipoles which are aligned, i.e. polarized by the electric field component. This interaction between light and matter leads to attenuation of the electromagnetic wave by scattering, absorption and dispersion which are discussed next.

4.1 Rayleigh and Mie scattering

Scattering occurs when light propagating in a given direction is deviated from its original path. For instance, when light from the Sun goes through the Earth's atmosphere it is scattered by gas molecules. The gas molecule first absorbs the light and is polarized by it oscillating with the field of the electromagnetic wave. The oscillating molecule then re-emits light in all directions with an angular distribution typical to electrical dipoles as shown in Figure 4-1 (a). As the light is re-emitted in several directions it loses intensity in its original direction and is attenuated. Such scattering can take place not only from molecules but also from dielectric particles or from local variations in the refractive index of a material. Scattering from particles smaller than approximately one tenth of the wavelength of light is called Rayleigh scattering of which the blue sky is a typical example. The scattering intensity is strongly wavelength dependent so that short wavelengths scatter more effectively compared to long wavelengths. For larger particles the predominant scattering mechanism is called Mie scattering. Compared to Rayleigh scattering, Mie scattering is very insensitive to wavelength. Mie scattering can be observed in clouds where light across the visible range is evenly scattered by large water droplets thus giving the cloud a white color. The distribution of scattering intensity for Mie scattering is shown in Figure 4-1 (b). [1, 4, 24]

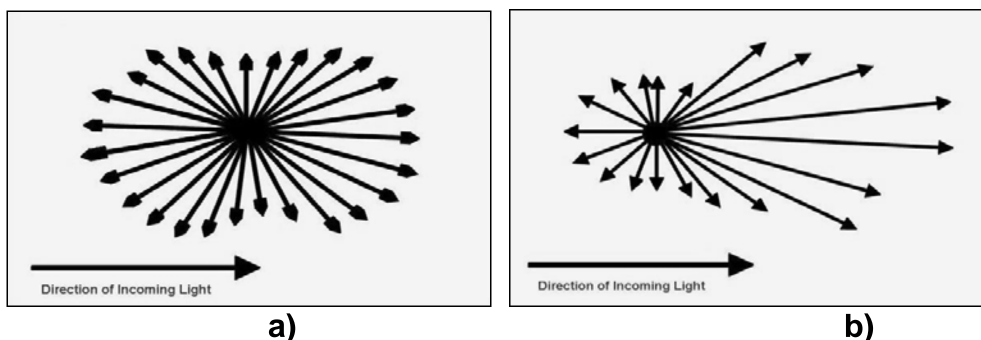

Figure 4-1. The distribution of light intensity upon a) Rayleigh scattering and b) Mie scattering [6].

In a homogeneous dielectric medium, coherent scattering takes place from atoms and molecules. When the scattered light interferes with un-scattered light, the wave diffracts and experiences a reduction in its velocity. Coherent scattering of light is the fundamental reason why the speed of light and, therefore, the refractive index varies between materials. [1, 4, 24]

4.2 Absorption and dispersion

As all materials absorb electromagnetic radiation by their atoms and molecules, the intensity of the wave is reduced as it propagates through matter. In dense materials absorption occurs in a broad wavelength range and the energy absorbed is generally converted into heat. The absorption of ultraviolet and visible light causes excitation of electrons while the absorption of visible and infrared light excite molecular vibrations and rotations in atoms. In optically transparent materials, there is no absorption in the visible spectrum of light but light in the UV and IR ranges can still be absorbed.

Absorption in matter is strongly related to the refractive index. The variation of refractive index or variation in the velocity of light as a function of wavelength is called dispersion. Sharp absorption peaks are commonly found at wavelengths where the refractive index shows rapid changes. The absorption coefficient and refractive index as a function of wavelength for a typical dielectric material are shown in Figure 4-2. Notice that for each oscillation of the refractive index, there is a sharp increase in the absorption coefficient.

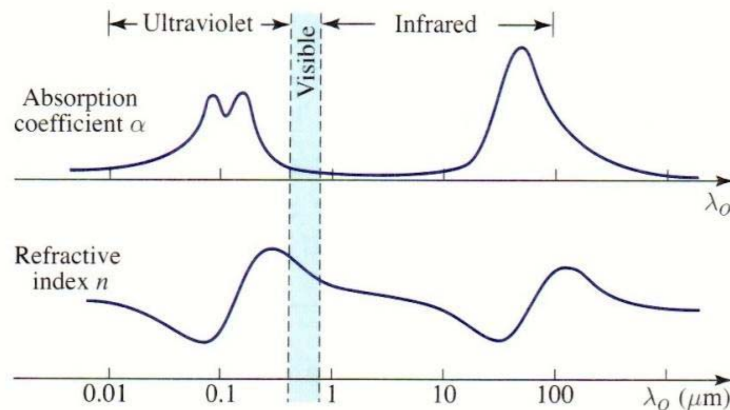

Figure 4-2. Absorption coefficient and refractive index as a function of wavelength for a typical dielectric material [7].

The refractive index of a material as a function of wavelength can be calculated using the Sellmeier Equation 4.1 provided that optical constants B_i and C_i characteristic to each material are known.

$$n^2 = 1 + \frac{B_1}{\lambda^2 - C_1} + \frac{B_2}{\lambda^2 - C_2} + \frac{B_3}{\lambda^2 - C_3} \tag{4.1}$$

The refractive index between 130 – 1000 nm wavelengths for Corning 7980 silica glass calculated using the Sellmeier equation is shown in Figure 4-3 below. The rapid increase in refractive index at short wavelengths indicates increased absorption.

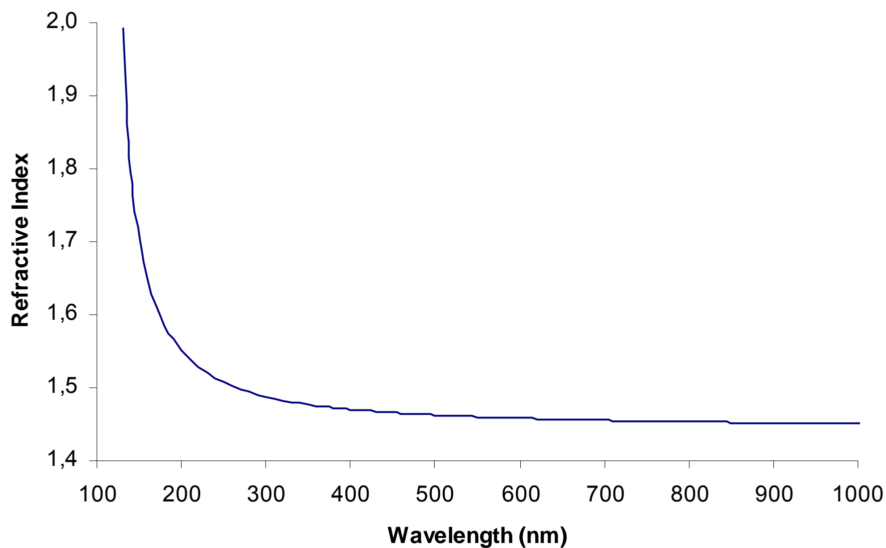

Figure 4-3. The dispersion curve for Corning 7980 silica glass.

The Abbe number, also known as the V-number, is often used as a measure of dispersion for transparent materials and to classify different glasses. The higher the Abbe number, the lower the dispersion, which means that the refractive index changes very little as a function of wavelength in the visible spectrum of light. For the Corning 7980 silica glass the Abbe number is approximately 68 which indicates that it has low dispersion and is a fairly good quality crown glass. [1, 5, 8]

5 Propagation of light in optical fibers

The propagation of light in an optical fiber is based on total internal reflection from the core-cladding interface. To satisfy the condition for total internal reflection the refractive index of the core has to be higher than the refractive index of the cladding and the angle of incidence must be higher than the critical angle. In typical step index fibers where the refractive index changes abruptly at the core-cladding interface, the refractive index difference between n_1 and n_2 is less than a few percents. Figure 5-1 shows a cross-section view of a typical step index fiber which is cylindrically symmetrical and has a high refractive index core and a low refractive index cladding. Due to the cylindrical nature of the fiber, light reflecting from the core-cladding interface can be a meridional ray that always crosses the fiber axis, a skew ray that never crosses the axis or an axial ray traveling along the center axis of the fiber. The differences between the meridional, skew and axial rays propagating along the fiber are also illustrated in Figure 5-1.

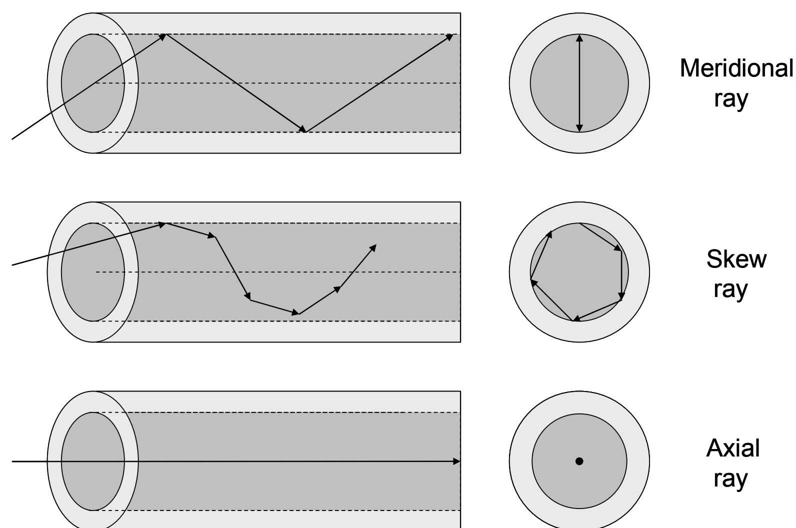

Figure 5-1. Meridional, skew and axial rays in a step index fiber [24].

Because of the wave nature of light the wave propagating inside the core interferes with itself and with other co-propagating waves. The interference must be constructive to allow the waves to propagate successfully as destructive interference will result in cancellation of the waves. The constructive interference creates standing wave patterns inside the fiber which are electric field patterns also called modes of propagation. In circular step index fibers, the modes of propagation are a mix of TE and TM waves and are generally called LP modes

where LP stands for linearly polarized. Each of the modes has a different electric field distribution as can be seen from Figure 5-2 which shows the electric field distribution for the LP_{01} mode and the light intensity distributions for the first three modes in a cylindrical fiber. The LP_{01} mode is also called the fundamental mode.

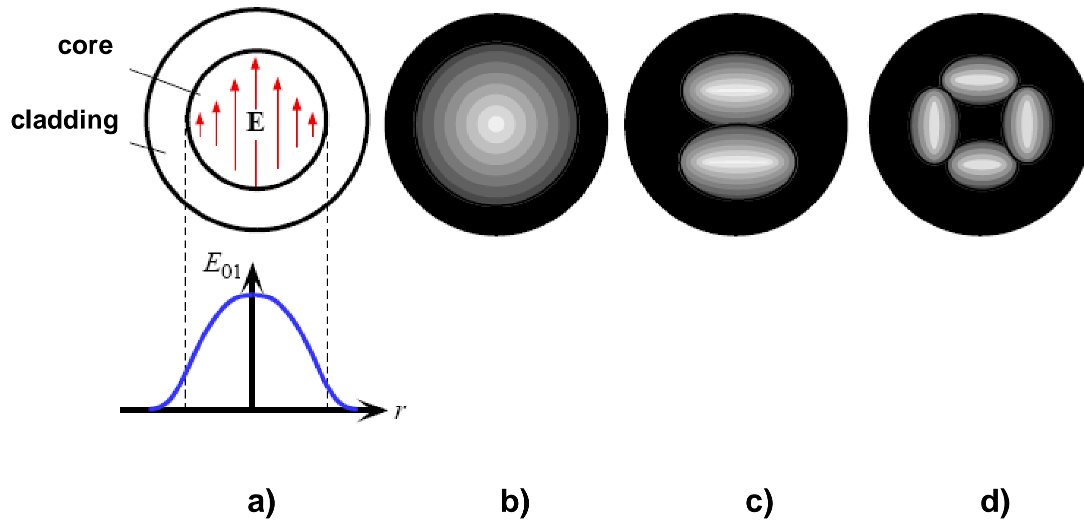

Figure 5-2. Illustrations of a) LP_{01} electric field distribution b) LP_{01} light intensity pattern c) LP_{11} light intensity pattern d) LP_{21} light intensity pattern in a step index fiber [24].

As described in Chapter 3, an evanescent wave travels parallel to the core-cladding interface. This wave extends slightly into the fiber cladding and can result in light loss due to frustrated total internal reflection if the cladding layer is not sufficiently thick. The electric field distribution for the fundamental LP_{01} mode in Figure 5-2 (a) shows how the evanescent wave extends the electric field from the core to the cladding. Since light propagating along a fiber is divided into modes which each travel at a different group velocity, the modes arrive at the end of the fiber at different times. This causes broadening of the light pulse also known as intermodal dispersion which can be removed by allowing only the fundamental mode to propagate in the fiber. A fiber with only one mode is called a single mode fiber while a fiber with multiple modes is called a multimode fiber. As the intermodal dispersion is eliminated from a single mode fiber it can transmit information at a much higher rate compared to multimode fiber. For this reason the single mode fiber is preferred for long haul communications. The number of modes allowed in a fiber can be defined with the *V*-number which is a characteristic parameter for a fiber and is given by Equation 5.1.

$$V = \frac{2\pi a}{\lambda}\sqrt{(n_1{}^2 - n_2{}^2)}\ , \tag{5.1}$$

where *a* is the fiber core radius.

The fiber is single mode and supports only the fundamental LP_{01} mode when the V-number is below 2.405. After the V-number exceeds 2.405 the number of modes increases rapidly and can be up to several thousands for multimode fibers. As seen from Equation 5.1, the number of modes that can propagate in a fiber depends on the core radius, the refractive indices of the core and cladding and the wavelength of light. As a result, single mode fibers have a much smaller core radius compared to multimode fibers.

To successfully launch a signal into an optical fiber the light entering the core has to have a certain angle or otherwise it will not be totally reflected from the core-cladding interface resulting in rapid signal loss. The maximum acceptance angle can be calculated using Snell's law and it depends on the refractive indices of the core, the cladding and the medium where the light is launched from. Equation 5.2 gives the maximum acceptance angle α_{max} which is further illustrated in Figure 5-3.

$$\alpha_{\max} = \sin^{-1}\left(\frac{\sqrt{n_1^2 - n_2^2}}{n_0}\right) = \sin^{-1}\left(\frac{NA}{n_0}\right) \tag{5.2}$$

The nominator in Equation 5.2 is also called the numerical aperture or NA.

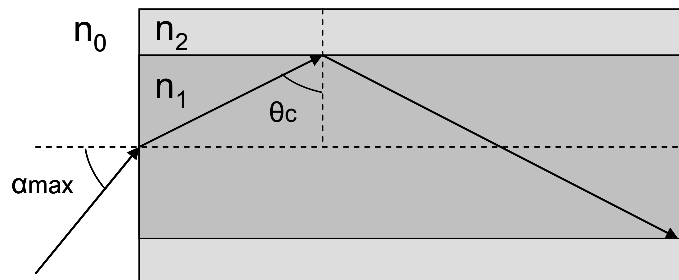

Figure 5-3. The maximum acceptance angle for an optical fiber [24].

The concept of optical fibers will be further discussed in Chapter 8.4 where a CMOS image sensor utilizing a lightpipe to guide light to the photodiode is introduced. [1, 24]

6 Detection of light

The most common silicon-based techniques used for detecting visible light are reviewed in this chapter along with the fundamental physical phenomenon behind them.

6.1 The photoelectric effect

A photon can excite an electron from the lower energy valence band to the higher energy conduction band if the energy of the photon is equal to or greater than the bandgap energy of silicon. The number of charge carriers generated by the absorbed photons is proportional to the intensity of light. This generation of an electron-hole pair via photon absorption is called the photoelectric effect. It should be noted that the photoelectric effect is not limited to only silicon as it can take place in other semiconducting materials and also in metals. Since the photon energy is wavelength dependent there exists a threshold value above which the photons are no longer absorbed regardless of the photon intensity. Equation 6.1 shows the relationship between the photon energy E_{ph} and the wavelength.

$$E_{ph} = \frac{hc}{\lambda}, \tag{6.1}$$

where h is Planck's constant.

For intrinsic silicon the bandgap between valence and conduction bands is 1.12 eV, which corresponds to a threshold wavelength of 1.1µm. In other words, intrinsic silicon can absorb light only at below 1.1µm wavelengths. As the absorption coefficient of silicon is highly wavelength dependent, the photon flux decays exponentially from the silicon surface. As a result, photons with high energy (short wavelength) are absorbed closer to the surface than photons with low energy (long wavelength). For blue light at 450 nm the penetration depth is approximately 0.4 µm as for red light at 600 nm the equivalent penetration depth is approximately 2.4 µm. The penetration depth is defined as the distance in which the photon flux has decayed by 1/e. After the photon with a sufficient amount of energy has excited an electron to the conduction band via the photoelectric effect, the electron is free to participate in charge transfer. The free carrier will however eventually recombine with a hole in the valence band or with a defect site in the silicon crystal and become immobilized. The recombination lifetime depends on the silicon doping concentration and crystal quality. In image sensors, a long carrier lifetime is preferred so that the electron can be captured and read as a signal before it recombines and is lost. [1, 8]

6.2 Silicon-based technologies for light detection

The photodiode and photogate are two of the most common structures used in detecting light with silicon-based technologies. A photodiode is made by forming a pn-junction between p-type and n-type semiconductors with doping impurity atoms such as boron or arsenic into the silicon substrate. As the p-type and n-type regions come into contact, electrons diffuse from the n-type side to the p-type side and holes diffuse from the p-type side to the n-type side thus forming a depletion region free of mobile charge carriers in the junction. As a consequence, under equilibrium conditions a built-in voltage in the range of 0.6 - 0.8 V will be generated creating an electric field across the depletion region. The width of the depletion region is typically in the range of 0.1 – 1.0µm depending on the doping concentrations. Pn photodetectors are typically reverse biased so that a positive voltage is connected to the n-type and a negative voltage to the p-type region. This increases the voltage across the junction and widens the depletion region to a typical range of 1-3µm. Figure 6-1 (a) below shows the structure of a reverse biased pn photodetector. The depletion region reaches farther into the n-type layer due to its lower doping concentration.

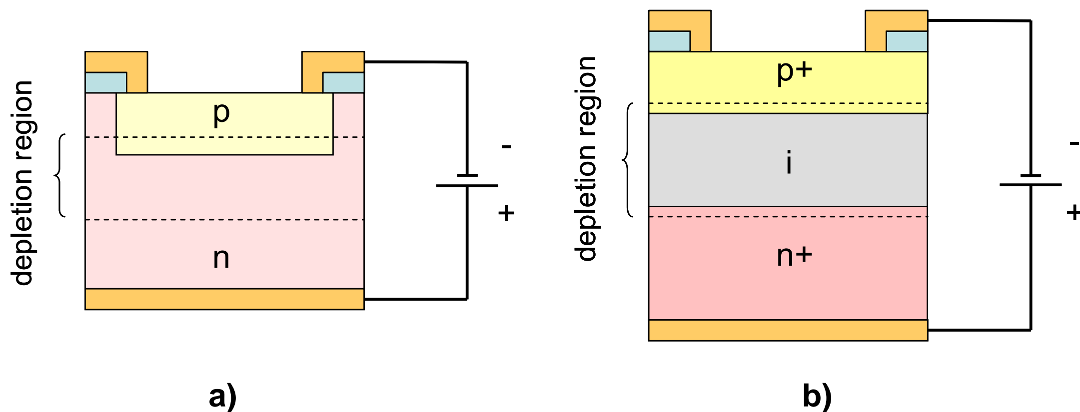

Figure 6-1. Schematic illustrations of a) pn photodetector and b) pin photodetector under reverse bias [22].

When photons with sufficiently high energy are absorbed inside the depletion region which acts as a potential well, the electrons start to build up until the full well capacity is reached. Since the number of electrons created is directly proportional to the amount of photons absorbed, the device can be used to detect the intensity of light. If a photon is absorbed outside the depletion region, it has to diffuse through the bulk silicon to reach the pn-junction in order to be collected by the electric field. The diffusion of electrons and holes in silicon is random and limited by the carrier lifetime. Photon absorption inside the depletion region is therefore

preferred as it increases the quantum efficiency of the detector. Quantum efficiency is the ratio of photogenerated electrons to incident photons and will be discussed in more detail in Chapter 7.3. The pn-junction can also be forward biased by changing the polarity of the external bias voltages so that a positive voltage is connected to the p-type region and a negative voltage to the n-type region. Forward biasing is commonly used in light emitting diodes (LED) and lasers to generate light instead of detecting it.

An improved version of the pn photodetector is the so called pinned or pin photodetector, which has an insulating intrinsic silicon layer between the p-type and n-type regions. The pinned photodetector is shown in Figure 6-1 (b). The insulating layer is used to control the depth of the depletion region making it possible to absorb more of the incident photons inside the depletion region rather than in the bulk silicon. This increases the quantum efficiency of the detector especially at longer wavelengths which penetrate deeper into the silicon substrate. The top surface of the pinned diode is highly doped to reduce dark current. [8, 22]

The photogate functions in a very similar manner to the pn photodetector, but instead of a pn-junction the photogate employs a MOS-capacitor structure. The depletion region used to collect the charge carriers is created in silicon when a positive voltage is applied to the metal electrode or gate. Figure 6-2 shows a cross-section view of a basic photogate structure. The insulating layer between the gate and silicon is typically silicon dioxide (SiO_2).

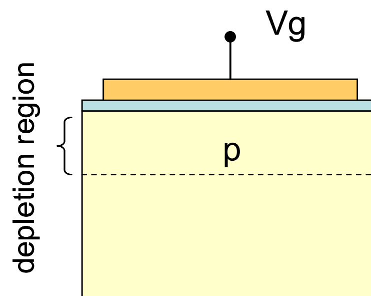

Figure 6-2. Schematic illustration of a photogate on a silicon substrate [23].

Both pn-junctions and photogates are used in image sensors to convert light into an electric signal using the photoelectric effect. The photogenerated charges are collected by the depletion region or potential well and stored until the well capacity is reached or the signal is read out. Under high illumination conditions the well capacity can be exceeded, in which case, the charges can leak to the neighboring pixel and create a so called blooming effect which is seen as oversaturation of bright areas. Large well capacity gives the sensor a wider dynamic range. The

photogate has a somewhat lower sensitivity compared to pn-type photodetectors due to the gate electrode which absorbs and blocks some of the incident light. Both pn-junctions and photogates are used in CCD sensors depending on the application but modern CMOS image sensors most commonly use the pinned photodiode structure. [8, 23, 25]

7 The digital camera

After the first digital still camera which was able to store images in a digital form was presented by Fuji in 1988, there have been remarkable improvements in the image quality and data storage capability of digital cameras. These technological advances have enabled the digital camera to almost completely replace its conventional silver halide counterpart. Instead of capturing and storing the image on a photographic film, the digital camera uses an image sensor to convert light into an electrical signal and a memory chip to store the information. Even though the digital camera could not for a long time match the image quality of a conventional film camera, the possibility of viewing the images instantly on the camera's LCD screen made digital cameras very popular among consumers. After significant improvements were made in image quality, the digital camera found its way also into scientific and professional use. Recently, the low cost and small size of image sensors have made it possible to integrate digital camera modules into many electronic devices such as cellular phones, computers and even toys. This chapter will focus on the image sensor technologies used in today's digital still and video cameras. [8]

7.1 Image sensors in digital imaging

The image sensor, along with the lens optics, is the most important component in a digital imaging system when considering image quality. It is used to convert incident photons into an electrical signal which can be then read-out, processed and converted into digital form. Figure 7-1 shows a cross-section view of a conventional camera module (CCM) and a chip scale camera module (CSCM) used, for example, in mobile applications. In the conventional camera module, the image sensor is attached to a PCB board with wire-bonds providing electrical connections to other passive components on the circuit board. The chip scale camera module on the other hand is a more advanced packaging method where through silicon vias (TSV) connected to solder balls on the backside of the image sensor chip are used instead of bonding wires for providing electrical connections. The CSCM approach has the advantage of smaller module size and lower cost.

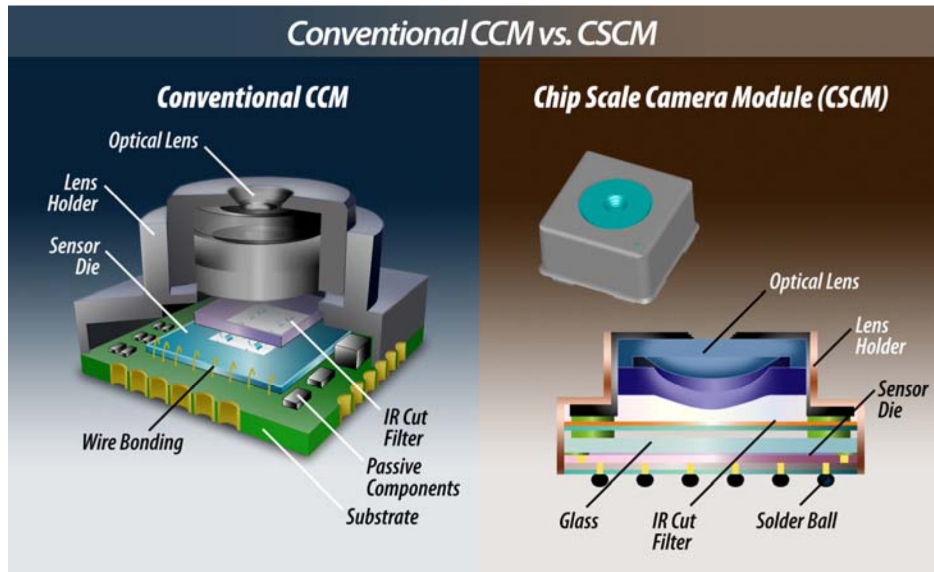

Figure 7-1. Image sensor in CCM and CSCM camera module assemblies [54].

Above the image sensor there can commonly be found a cover glass, an infrared cut filter, an optical low pass filter and finally the lens optics. The IR-cut filter is used to block infrared light which can otherwise distort image colors. The optical low-pass filter (OLPF) is used to eliminate the Moiré effect which creates interference patterns on images. The OLPF can also include an IR-cut filter function thus removing the need for a separate infrared filter. [8, 13, 17, 43]

The charge coupled device (CCD) has been the image sensor of choice for decades after its invention in 1969. Compared to other solid-state imagers, the CCD has had the advantage of higher sensitivity and lower noise. It wasn't until the 1990's that the CMOS image sensor (CIS) became a viable alternative to CCD although performance limitations made it initially suitable only for applications where the image quality was not a critical factor. Lower power consumption, cost-effectiveness, high speed and small size however gave the CIS an advantage over CCD sensors in certain applications. Currently, the CMOS image sensor has matured to a stage where it can challenge the CCD based sensor and even outperform it. However, in high quality digital imaging the CCD is still the dominant image sensor. Both technologies are based on pixel arrays which are used to convert incident light or photons into electrons via the photoelectric effect. For visible light imaging the substrate is typically silicon due to its band gap energy (E_g = 1.12 eV), which is suitable for absorbing light in the visible spectrum of light. Both CCD and CIS are so called monochrome sensors as they are inherently incapable of detecting colors. Only the intensity of light can be determined from the amount of photons reaching the sensor. A color filter array functioning as a band-pass filter is

typically used to filter different wavelengths of light to specific pixels making it possible to detect colors. For small pixel sizes a microlens array is typically used to focus light into the photoactive area of the pixel to increase the light collection efficiency and reduce optical crosstalk.

The manufacturing of a CCD image sensor requires processes which are not typically found in common integrated circuit production lines. For this reason, three or four additional chips are typically needed to create a complete CCD camera system. The CIS on the other hand can be built using the industry standard CMOS manufacturing process used for logic devices. This allows integration flexibility as other basic camera functionalities can be included on the same CIS chip. The functional differences between CCD and CIS are illustrated in Figure 7-2.

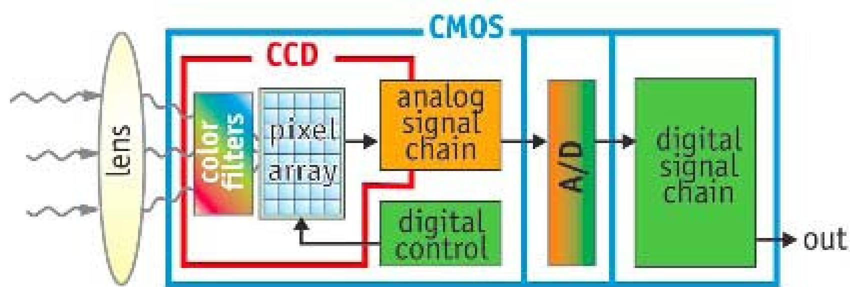

Figure 7-2. Functional differences between CCD and CIS based sensors [12].

A short introduction to both CCD and CMOS image sensor technologies is given in the following chapters, but the main focus for the remainder of this work will be on the CMOS image sensor. [8, 20]

7.1.1 The charge coupled device

The charge coupled device can use either photogates or photodiodes to perform the signal generation and collection. In the photogate approach, a large number of metal oxide semiconductor (MOS) structures are formed side by side which allows electrons collected in the potential wells under each electrode to be transferred across the array by simply controlling the gate voltages. The collected charge packets can then be transferred to an amplifier and converted into a voltage signal. The above described surface channel CCD (SCCD) is however sensitive to electrons being trapped in surface and interface states in the Si-SiO_2 junction. Electrons trapped in these defect sites are lost and unable to participate in the charge transfer process. A buried channel CCD (BCCD) where the charges are transferred deeper in the silicon was introduced to avoid this problem. The electrodes or gates in photogate based CCDs are typically made of polysilicon or

indium tin oxide (ITO). Polysilicon starts to absorb light at below 600 nm and becomes fully opaque for light below 400 nm. This significantly reduces the image sensor sensitivity especially for blue light. Thinner polysilicon gates or ITO are preferred due to better transparency. Photodiodes can be used instead of photogates to increase sensitivity as there are no gate metals in the optical path of light.

The three main CCD array architectures, chosen depending on the application, are called the frame transfer CCD (FTCCD), full-frame transfer CCD (FFTCCD) and interline transfer CCD (ITCCD). The FTCCD and FFTCCD employ the photogate for light detection while the ITCCD uses photodiodes instead. Figure 7-3 shows top view schematics of these three architectures.

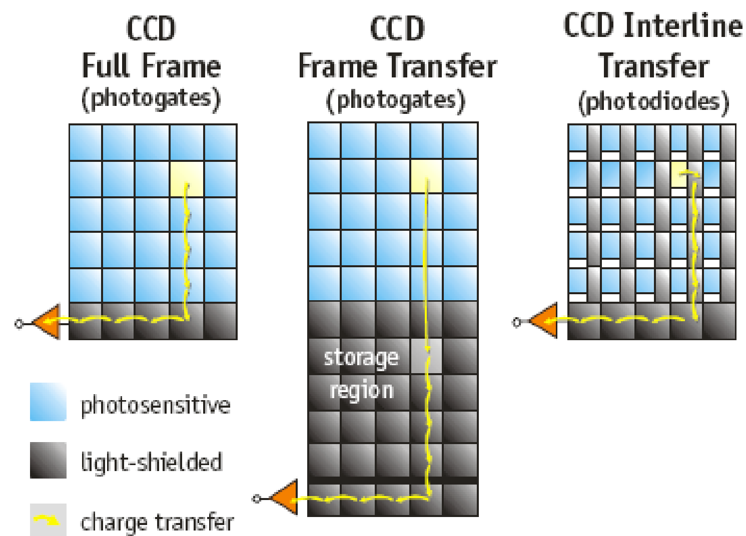

Figure 7-3. FFCCD, FTCCD and ITCCD architectures [25].

The frame transfer CCD has the photoactive area under a light absorbing gate layer as described earlier and suffers from low sensitivity especially for blue light. In FTCCD the charges are generated during an exposure cycle after which they are transferred row by row to a separate light shielded storage area. This allows fast frame rates as the new exposure cycle can start already during signal read-out. The FTCCD, however, requires a lot of silicon area resulting in higher cost. The full-frame transfer CCD (FFTCCD) operates much like the FTCCD but the storage area is removed which simplifies the sensor structure and reduces chip size and cost. FFTCCD is popular especially in professional digital still cameras since it can offer very high resolution although it suffers from low frame rate due to the lack of the charge storage area. A new exposure cycle cannot start before the read-out is complete. Also a mechanical shutter needs to be used to prevent the

generation of additional charge carriers during charge transfer. The fill factor for both FTCCD and FFTCCD is typically around 100%. Fill factor is the ratio of the photosensitive area in the pixel to the overall pixel area. Higher fill factor increases the light collection efficiency and the sensitivity of the pixel especially under low light conditions. Figure 7-4 shows a cross-section SEM image of a full-frame transfer CCD with 6.8 µm pixel size. Indium tin oxide gates and a metal aperture are used for improved transmittance and reduced crosstalk.

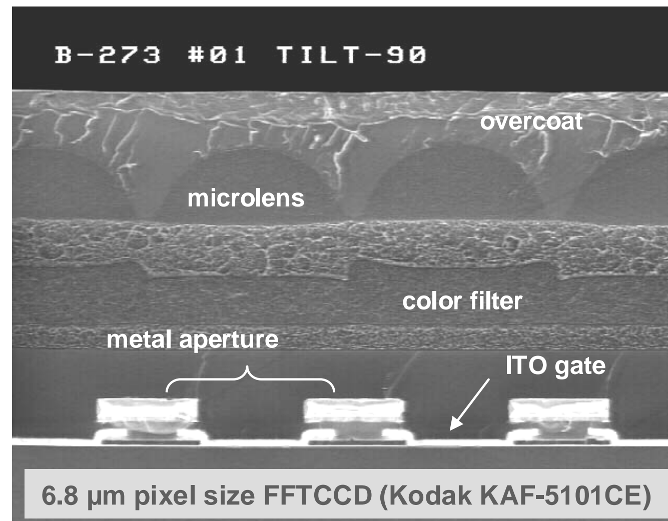

Figure 7-4. Cross-section view of a Kodak 5 megapixel FFTCCD image sensor with 6.8 µm pixel size [37].

In consumer applications the most popular structure is the so called interline transfer CCD (ITCCD) in which a photodiode is placed next to the charge transferring register where it is not optically blocked by the gate electrode. A major disadvantage of ITCCD is the reduced fill factor which is often compensated with microlenses. In ITCCD the electrons formed in the photodiode are first transferred to the vertical CCD or interline transfer register. From there the electrons move to the horizontal CCD and are amplified at the output amplifier where the charge is converted into a voltage signal. There is no need for a separate charge storage area as in FFTCCD. A light shield above the ITCCD gate electrodes is used to prevent the formation of charge carriers during charge transfer which eliminates the need for a mechanical shutter.

To further improve sensor performance such techniques as UV enhancement coatings and backside illumination can be used. The UV enhancement coating, which is transparent to visible light, absorbs UV and deep-blue light and re-emits it at a longer wavelength via fluorescence which increases the sensor sensitivity. A

more detailed description of backside illumination will be given in Chapter 8.3 for CIS but the same basic principles apply also to CCD sensors. [8, 20, 23, 37]

7.1.2 CMOS image sensor

Similarly to CCDs the CMOS image sensor has an array of pixels used to convert light into an electrical signal. The first generation of CIS was based on passive pixel sensors (PPS) which had no signal amplification inside the pixel. The fill factor in PPS was high, but due to low sensitivity and high noise, it has been mostly replaced by the active pixel sensor (APS) which is the dominant pixel type in current CIS devices. The main benefit of the APS is that the signal is less susceptible to noise as the charge is converted into a voltage or a current signal and amplified by a built-in transistor already inside the pixel. The most significant drawback of the APS is a low fill factor as there is less room for the photodiode since each active pixel contains typically three or four transistors. Sub-micron CMOS process technologies and the so called shared pixel design where neighboring pixels share transistors to decrease the non-photosensitive area in each pixel have been introduced to increase fill factor. After charge generation and conversion the signal in CIS is read by an X-Y addressing scheme where vertical and horizontal scanners are used to read out the rows and columns, respectively. This type of system allows a more flexible readout as the pixels to be read can be selected independently. In CCD image sensors all the pixels are read continuously which also leads to higher power consumption.

The photodiode in modern CIS devices is typically a pinned photodiode which effectively reduces noise and dark current compared to a standard pn-junction diode. Dark current is the current that flows in the device under no illumination and is a major limitation to the sensor’s low light performance. Standard photodiode structures and photogates can also be used in CIS but their performance does not match the pinned photodiode. Top view schematic and a cross-section SEM image of a typical CMOS image sensor are shown in Figure 7-5.

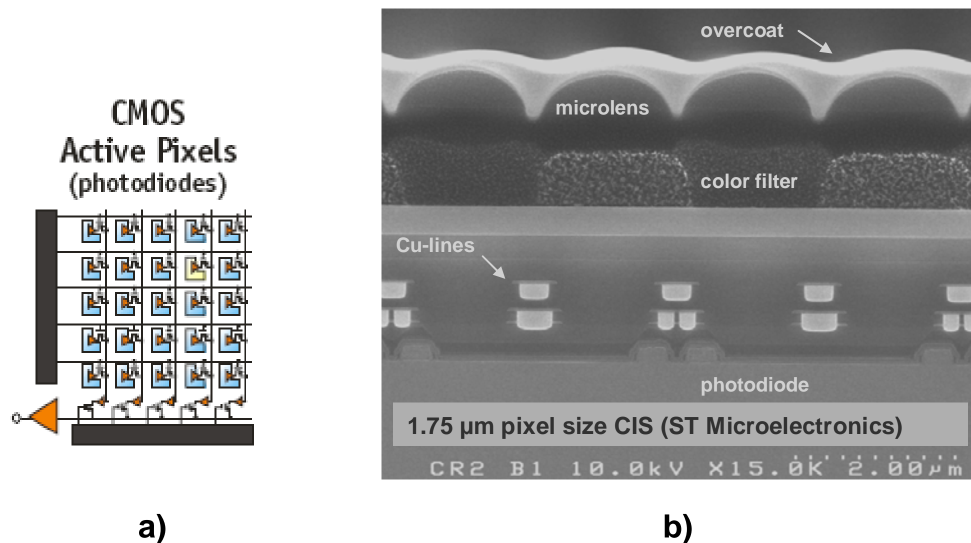

Figure 7-5. Active pixel CIS: a) top view schematic and b) cross-section SEM of a 3 megapixel ST Microelectronics sensor with 1.75 µm pixel size [19, 25].

Compared to CCD, there are multiple metallization layers in CIS pixels and the dielectric stack between the color filter and silicon surface is thicker. This increases the optical path length of light as well as optical crosstalk. The dielectric stack typically consists of silicon dioxide and silicon nitride films which are used to electrically isolate the metal lines and act as passivation layers against humidity and impurities. Borophosphosilicate glass (BPSG) and tetraethyl orthosilicate (TEOS) films can also be used. Although the dielectric layers are typically highly transparent to visible light, the large refractive index mismatches between SiO_2, Si_3N_4 and silicon can create high losses through reflections which is why it is important to optimize the dielectric stack structure. Silicon oxy-nitride buffer layers with refractive indices between that of oxide and nitride as well as selective removal of the nitride layers from the optical path can be used to reduce the reflections. Also adopting copper metallization technology enables the reduction of the metal layer height due to copper's low resistivity and shortens the optical path length compared to the traditionally used aluminum back-end process. The recent advances in CIS design are discussed in greater detail in Chapter 8.

One of the main advantages of CIS over CCD is lower power consumption making it highly suitable for portable applications. The power consumed by a CIS chip is 50-90% lower compared to a CCD chip-set with the same functionalities. This is mostly due to low operating voltages reducing power dissipation, the X-Y readout scheme and on-chip functionalities using the same power supply as the CIS. Additionally, the CIS is much more suitable for high speed imaging compared to CCD and is less sensitive to blooming effects. The noise performance of CIS has traditionally been inferior compared to CCD imagers but recently this problem has been reduced to a level that CMOS image sensors can also be used in

professional cameras. Also the fill factor for a typical CIS is significantly lower compared to, for example, full frame CCD which can achieve a fill factor of close to 100%. [8, 10, 12, 17, 18, 29, 41]

7.2 Color separation and light focusing

Both CCD and CIS sensors typically have a color filter and a microlens above each pixel as shown in Figures 7-4 and 7-5. Since both sensors are monochrome by nature, a color filter layer deposited above the photodiode is used to transmit only certain wavelengths so that different colors can be separated. Microlenses are used especially with smaller pixel sizes to focus light on the photodiode to increase fill factor and reduce optical crosstalk. Figure 7-6 shows cross-section and tilted view scanning electron microscope (SEM) images of the color filter and microlens layers.

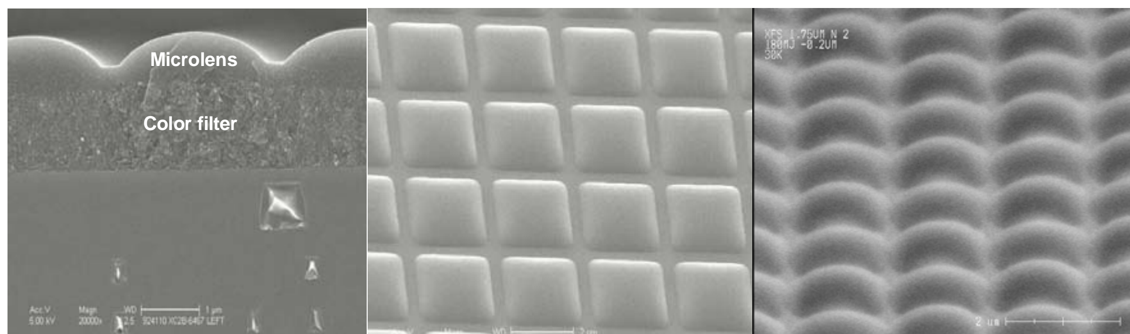

Figure 7-6. Color filters and microlens array in CMOS image sensor [17, 19].

The color filter array (CFA) is typically arranged according to the so called Bayer pattern which has twice the number of green pixels to the number of blue or red pixels. The amount of green pixels is high since the human eye is most sensitive to green color and detects luminance in the green spectrum. The color filter material is either a pigment or a dye-based photosensitive organic polymer, such as polymethylmethacrylate (PMMA), designed to have high transmittance only at a certain wavelength range. The color filter transmittance is typically only approximately 70-90% in the pass-band making the CFA a significant source of losses in the image sensor. Instead of using the primary colors red, green and blue, complementary colors yellow, cyan and magenta are sometimes used in color filters mainly due to their improved transmittances. The complementary color pattern however suffers from poorer color reproducibility and has been used mainly in CCD imagers for movie application. Figure 7-7 shows the Bayer primary color pattern and typical transmittance curves for color filter materials for the three primary colors.

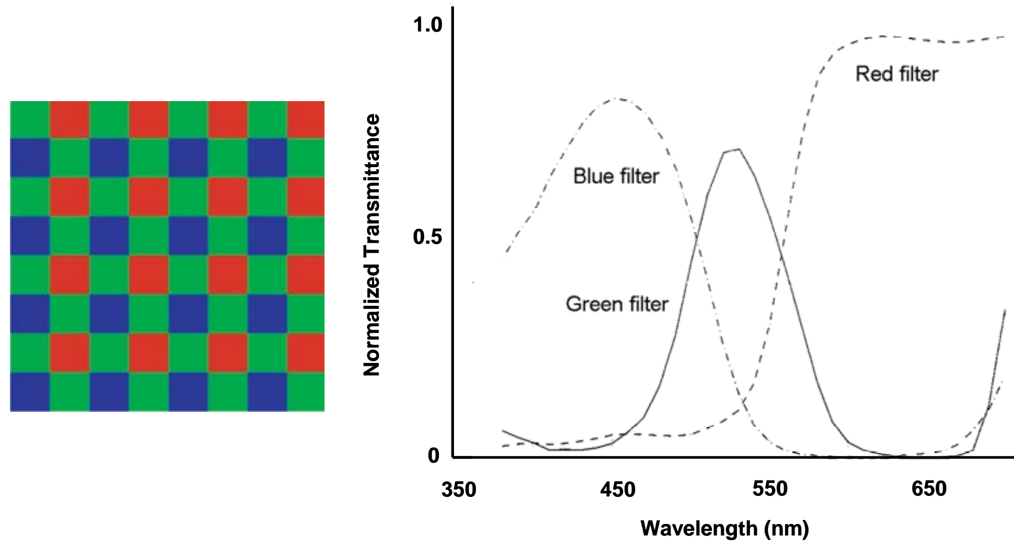

Figure 7-7. The Bayer pattern and typical color filter transmittance curves [11, 18].

Recently, white pixels which are sensitive to light over the entire visible spectrum have also been added to the Bayer pattern to increase the signal-to-noise ratio of the image sensor. Although the CFA approach is the most popular one, other color separation techniques exist. Prisms and beam splitters can be used to separate colors but a dedicated image sensor chip is then required for each color. The resolution is improved but the cost is higher and it is not suitable for mobile applications due to requiring a lot of space. A triple well structure with three vertically stacked photodiodes has been also demonstrated. This design takes advantage of the different absorption depth of blue, green and red light which eliminates the need for color filtering layers.

The microlenses are made from an organic photopatternable material and shaped into the planoconvex form after patterning using a thermal reflow step. By controlling the shape and radius of curvature of the microlens the focal length and spot size can be adjusted to match the sensor structure so that the light is effectively focused on the photodiode area. Both square and circular shaped lenses are commonly used as shown in Figure 7-6. The gap between adjacent lenses is typically minimized to increase light collection efficiency. Some imagers can also have an inner microlens below the color filter array to further enhance the optical sensitivity as shown in Figure 8-3 on page 39. There are, however, drawbacks with using microlenses to improve fill factor and sensitivity as the sensor performance becomes more dependent on the angle of incident light and lens aperture size. To reduce reflectance from the air-microlens interface, a thin oxide layer can be deposited on top of the microlens array. The capping layer also

helps to prevent surface contamination which has been found to be one of the most significant yield issues in image sensor fabrication. During the die sawing process silicon dust is created which can adhere to the organic microlens layer. A protective coating makes the surface of the sensor easier to clean reducing the amount of particles. The thermal budget for the capping layer deposition is limited as the organic color filter and microlens materials cannot typically withstand temperatures above 250°C without degradation. A combination of the microlens and color filter array has also been suggested. In this approach the color filter itself is shaped into a planoconvex lens form thus eliminating the need for a separate microlens layer. [8, 13, 17, 25, 28, 34, 41]

7.3 Image sensor performance

The performance of an image sensor, whether it is CCD or CIS, is typically measured by such parameters as sensitivity, spectral response, dynamic range and noise. These parameters and their influence on image quality and sensor performance is discussed next.

7.3.1 Sensitivity and spectral response

Sensitivity is a measure of how well the image sensor performs under low light conditions and is mainly dependent on the pixel fill factor and quantum efficiency. The fill factor in APS CIS is limited by the relatively small photodiode surface area and shadowing effects by metal interconnects. The wavelength dependent quantum efficiency is the ratio of photogenerated electrons to photons incident on the pixel and defines the efficiency of the photoelectric conversion. Ideally every photon would be absorbed in the depletion region and generate a charge carrier but due to non-idealities such as reflections, absorption and recombination the quantum efficiency can never reach unity. A typical graph showing the spectral response by a measure of quantum efficiency for blue, green and red light is shown in Figure 7-8.

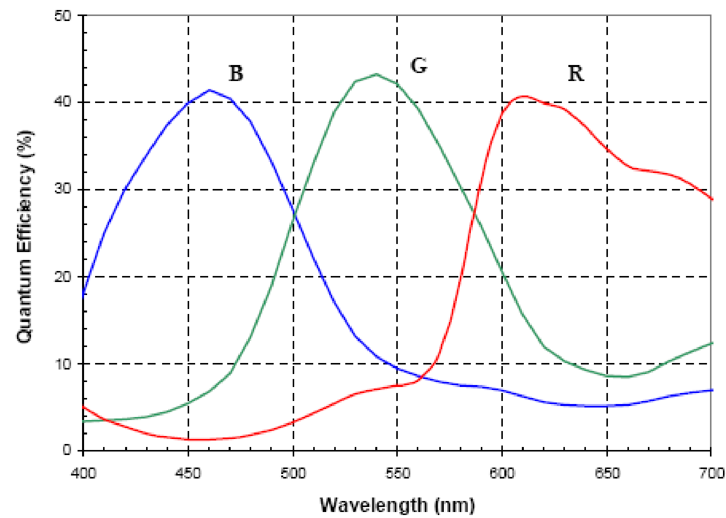

Figure 7-8. Quantum efficiency of a Micron Technology 3.1 megapixel CMOS image sensor with 3.2 µm pixel size [17].

Several methods have been introduced to increase quantum efficiency and sensitivity. Some of these methods, including backside illumination and a lightpipe structure, will be further discussed in Chapter 8.

Another important parameter for characterizing an image sensor is angular response which is used to demonstrate how well the sensor can detect light incident with an angle. Figure 7-9 shows a typical angular response graph for a few different pixel sizes.

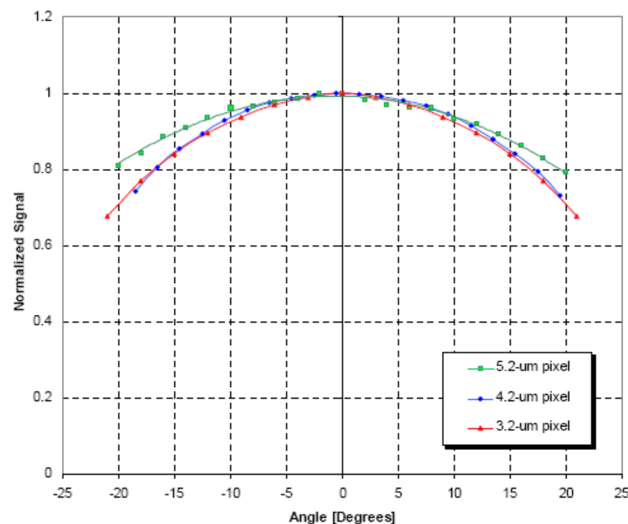

Figure 7-9. Angular response of a Micron Technology CMOS image sensors with 3.2 µm, 4.2 µm and 5.2 µm pixel size [17].

As seen from Figure 7-9, the signal intensity is highest at normal incidence and quickly decreases for off-axis light. This is a result of increased reflectance from dielectric interfaces and due to device geometry which further limits the collection ability. Light incident at an angle may not reach the photodiode if the microlens cannot sufficiently refract the beam. Furthermore, reflections can occur from the metal interconnect layers in the CIS dielectric stack. Smaller pixel sizes typically have poorer performance at high angles of incidence. [8, 20]

7.3.2 Noise

Noise degrades image sensor performance and determines the sensitivity and dynamic range. Noise in CIS can be divided into fixed pattern noise (FPN) and temporal noise. Fixed pattern noise originates from pixel-to-pixel variations and is mostly due to dark current nonuniformity and threshold voltage variations between transistors. As a result of FPN, the output signal varies from pixel to pixel. Pixels with higher output compared to others are called white pixels and can be seen as white spots on the image. FPN has been and still is one of the major limiting factors for active pixel CMOS image sensors. Temporal noise refers to noise which varies with time and consists mainly of thermal noise, shot noise and flicker noise. The temporal and fixed pattern noise together determine the dynamic range, i.e. the illumination range that can be detected by the sensor and the signal-to-noise ratio (SNR) for that range. Having a wide dynamic range is important especially when taking pictures of scenes with large variations in illumination. The dark current is temperature dependent and originates mainly from thermal generation of charge carriers. Due to heat generated by power dissipation in metal and semiconductor junctions, proper device cooling is essential in reducing dark current. Image sensors used for scientific applications typically have thermoelectric coolers and heat sinks in order to minimize dark current and improve the signal-to-noise ratio. In consumer applications the photodiode and pixel design are optimized to reduce dark current. Dark pixels shielded from light located at the periphery of the photodiode array can be used to set a reference dark current level. The reference signal from the dark pixels is reduced from the signal detected in the real pixels which as a result gives only the photogenerated signal. [10, 17, 20, 41]

7.3.3 Crosstalk between pixels

Crosstalk in an image sensor can be divided into optical, spectral and electrical crosstalk. Crosstalk is detrimental to the sensor performance as it generally reduces the sensor quantum efficiency and causes color mixing. Crosstalk increases significantly when pixel size is decreased.

Optical crosstalk occurs when light passing through a color filter at an angle gets absorbed by a photodiode in an adjacent pixel. This is illustrated in Figure 7-10 (a). Spectral crosstalk arises from imperfections in the color filter layer as shown in Figure 7-10 (b) where red light is transmitted through a green color filter. Using microlenses and reducing the dielectric stack height above the photodiode can efficiently reduce the optical crosstalk component. Also metal shields surrounding the photodiodes can be used. In this case the quantum efficiency however decreases as a portion of light will be reflected by the metal shield. In electrical crosstalk, the photogenerated charge carrier in silicon diffuses to the neighboring pixel as shown in Figure 7-10 (c).

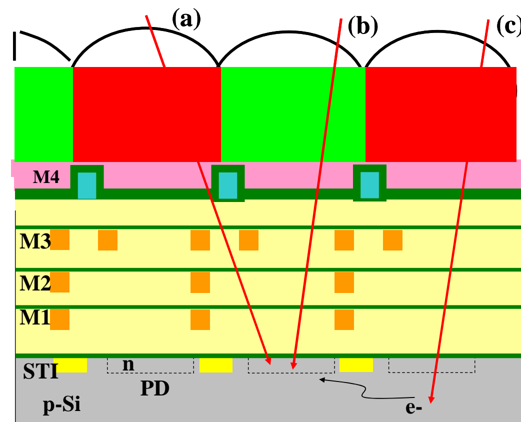

Figure 7-10. Crosstalk in CMOS image sensors: a) optical b) spectral c) electrical [21].

Electrical crosstalk can be minimized by increasing both fill factor and collection efficiency and isolating neighboring pixels electrically by using, for example, shallow trench isolation (STI) or implants between the pixels. [16, 41]

8 Recent developments in modern CMOS image sensors

Several advances have been made in increasing the CMOS image sensor performance during the last decade, but the drive towards even smaller dimensions has created a need for new design solutions. Some of the most effective methods used to increase especially small pixel sensor performance are presented in this chapter.

8.1 Pixel downscaling

Deep sub-micron CMOS process technologies have enabled significant pixel size reduction in CMOS image sensors during the last decade. The downscaling of pixel size has been beneficial especially in the relatively inexpensive point-and-shoot compact cameras and in other applications such as mobile devices where the image sensor chip size cannot be increased mainly due to cost related issues and lack of space. The cost of an image sensor is directly related to the size of the chip as larger chips consume more of the valuable silicon wafer area. Although higher pixel amount increases resolution, the number of pixels should not to be taken as a direct measure of the image sensor quality. In fact, applications where image quality is a key parameter favor sensors with larger pixel sizes due to their better performance and the downscaling has been mainly used to reduce in-pixel transistor size to increase the fill factor. For example, in high-end digital single lens reflex (DSLR) cameras, small pixel size is not essential and the image sensor size can even match the conventional 35-mm film size. High performance and low noise also in low illumination conditions are more important parameters for DSLR cameras than low cost and small chip size.

The evolution of the smallest pixel size available for CIS and the correspondingly used CMOS technology node is shown in Figure 8-1. A clear correlation can be found between pixel size and technology node. The curve for ITRS roadmap shows the development of the minimum feature size for logic devices and shows that process nodes used for CIS are approximately three generations behind the most advanced CMOS logic process. This is because modifications are needed to make the processes suitable for imaging applications. Currently, the smallest pixel size in production is 1.4 µm and active research is ongoing for pixel sizes around 1.0 µm.

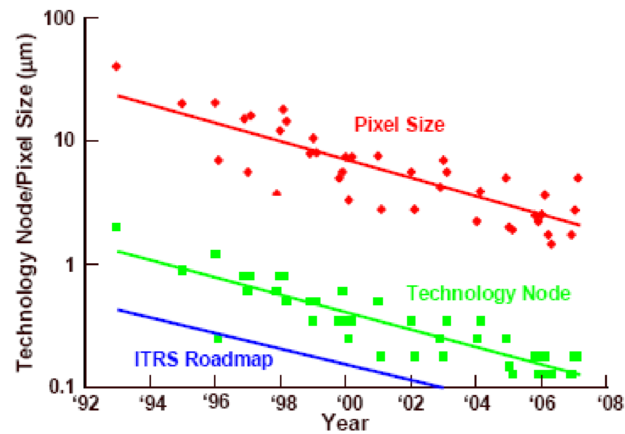

Figure 8-1. Evolution of pixel size and technology node for CIS [44].

While the higher pixel amount achieved with decreased pixel size increases the resolution of the sensor, parameters such as sensitivity, dynamic range and light collection efficiency are reduced as it becomes increasingly difficult for the light to reach the photodiode. Even if the fill factor remains the same, smaller pixels will have lower sensitivity. Low f-number lenses can be used to compensate for the reduced sensitivity but they are more expensive and have more aberrations which degrade image quality. F-number is the ratio of the lens focal length to the diameter of its aperture. Noise, crosstalk and angular dependency also increase with reducing pixel size and diffraction starts to limit the sensor performance when dimensions scale down towards the wavelength of light. The main challenge in reducing pixel size is in keeping the pixel performance on an acceptable level. Figure 8-2 shows a wave optics simulation for pixel sizes between 5µm to 1µm illustrating the effects of diffraction and the difficulties arising from pixel size reduction. Color is used to indicate the intensity of light.

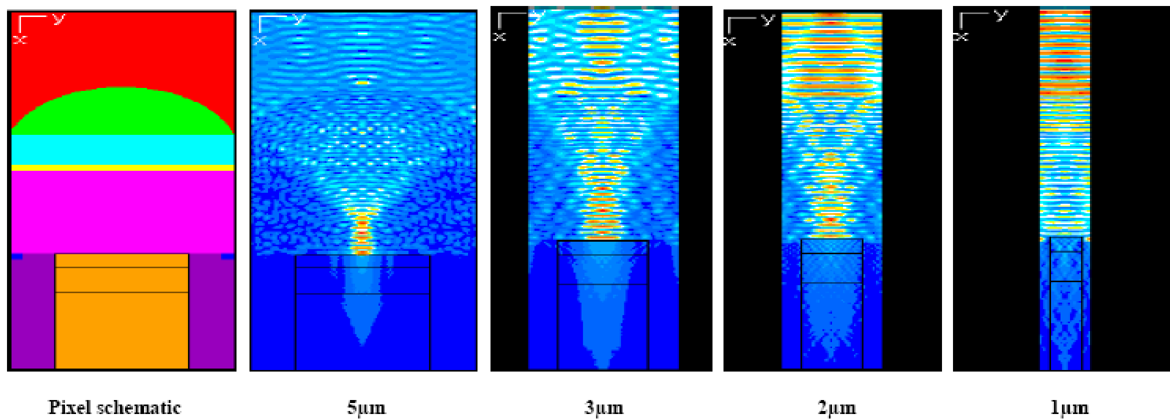

Figure 8-2. Wave-optics simulation of the effect of pixel size reduction [17].

As seen from Figure 8-2, the microlens can still effectively function with large pixels but as the pixel size shrinks to 2 μm and below less light is focused on the photodiode decreasing the fill factor and quantum efficiency. This is because light passing through a small circular aperture, such as a microlens, is diffracted and does not focus on a specific spot. Instead, a diffraction pattern is formed in the shape of a so called Airy disc which has a central bright spot where 84% of the light falls and alternating dark and bright rings surrounding it. The diameter of the Airy disc resulting from diffraction can be calculated by Equation 8.1 and is the smallest point that a beam of light can be focused.

$$d = 2.44\lambda(f/\#)\,, \tag{8.1}$$

where *f/#* is the f-number of the lens which is the ratio of focal length to the lens diameter.

For example, a microlens with an f-number of 2.8 gives a diffraction limited spot diameter of approximately 3.8 μm at 550 nm wavelength when lens aberrations are not taken into account. If the pixel size is smaller than the diffraction limited spot diameter, some of the light is focused outside the pixel area which reduces light collection efficiency and increases crosstalk. Due to longer wavelength, diffraction effects are more severe in the red end of the visible spectrum. Smaller pixels also suffer from small full well capacity which can create problems such as blooming effects when taking images under high illumination. [8, 13, 17, 25, 38, 41, 44, 46]

8.2 Dielectric stack optimization

The height of the dielectric stack above the photodiode has a significant impact on the sensor angular response especially with small pixels. If the pixel size is reduced and the dielectric stack height remains the same, light has to pass through a narrower opening which makes it difficult for the off-axis light to reach the photodiode. To reduce the height of the dielectric stack many image sensor manufacturers have moved from the traditional subtractive aluminum to copper metallization technology. Due to lower resistivity, copper lines can be made thinner than aluminum lines which enables the reduction of the dielectric stack height as shown in the cross-section SEM images in Figure 8-3. In this example a 40% reduction in the optical path length and a 20% increase in sensitivity was achieved by moving to Cu interconnect technology.

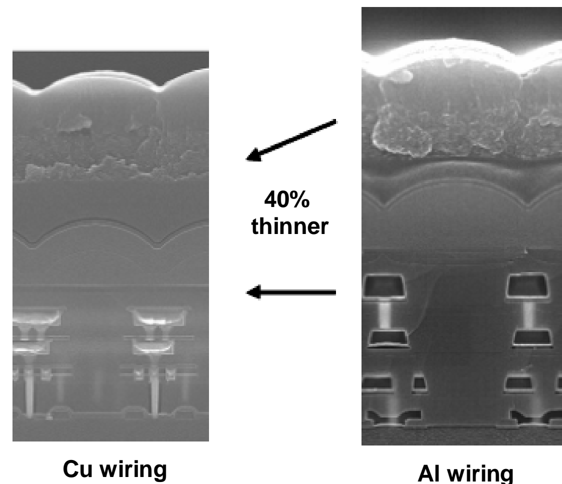

Figure 8-3. Aluminum versus copper interconnect technologies [45].

The drawback of copper is that it is easily oxidized during wafer processing. To prevent oxidation and diffusion into the surrounding dielectric films and into the transistor level, a barrier layer is needed. Typically, thin layers of silicon nitride (Si_3N_4), or sometimes silicon carbide (SiC), are used for this. Due to the refractive index mismatch between SiO_2 (n = 1.46 @ 633 nm) and, for example, Si_3N_4 (n = 2.0 @ 633 nm) there are significant reflections occurring in the SiO_2-Si_3N_4-SiO_2 interface. For this reason the nitride passivation layers are often removed from the optical path above the photodiode. Alternatively silicon oxy-nitride films with refractive index values between that of SiO_2 and Si_3N_4 can also be deposited between the oxide and nitride films to reduce reflections. Another way to address the reflectance issue is to passivate copper with cobalt tungsten phosphide

(CoWP) which can be deposited selectively only on copper and, therefore, no etch step is needed to remove the layer from the optical path. [14, 18, 29, 33]

8.3 Backside illumination

In modern active pixel CMOS image sensors, metal and dielectric films as well as transistor structures in pixels can block or deflect light from reaching the photodiode. This can significantly reduce the image sensor's sensitivity especially when using small pixel pitches. In backside illuminated image sensors the dielectric stack and metal layers are removed from the optical path by turning the sensor upside down thus allowing light a free path to the photodiodes through the silicon substrate. The silicon wafer must however be thinned down significantly (to the range of 5-15 µm) or otherwise the photons will be absorbed in the bulk silicon too far away from the active photodiodes. Figure 8-4 shows a comparison of a front side illuminated (FSI) and a backside illuminated (BSI) CMOS image sensor structure.

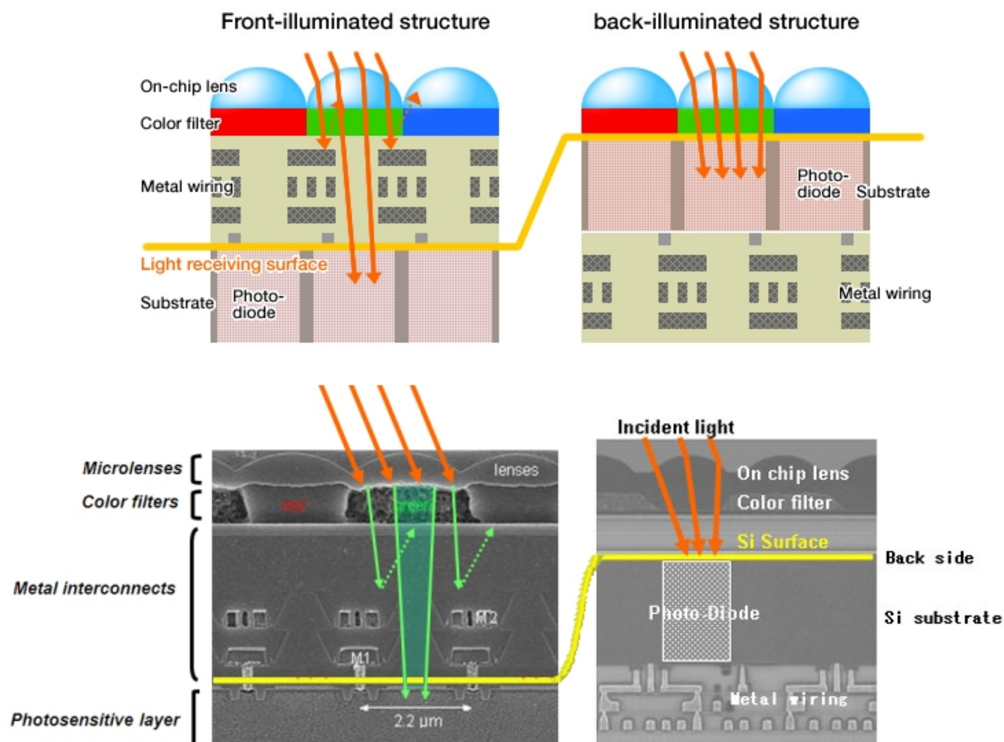

Figure 8-4. Frontside and backside illuminated sensor structures [38].

As shown in Figure 8-4, BSI sensors still utilize the traditional color filter and microlens layers for color separation and light focusing but they are deposited on the backside of the wafer after substrate thinning. An anti-reflective coating is

typically deposited between the silicon substrate and color filter layer to reduce reflections from the Si surface. The greatest benefit of the BSI architecture is the 100% fill factor and shorter optical path between the microlens and photodiode. This allows significant improvements in sensitivity and reduction in angular dependency as light does not have to be guided to the photodiode through a narrow opening between metal interconnects as is the case in FSI sensors. Additionally, crosstalk is reduced and there is more freedom in designing the interconnect layout. Also the number of interconnect layers can be increased without affecting the sensor's optical performance which allows smaller die sizes as the wiring levels can be stacked. Figure 8-5 shows a comparison in quantum efficiency and angular response between front side and backside illuminated Sony 1.3 megapixel CMOS image sensors with 3.75 µm pixel size.

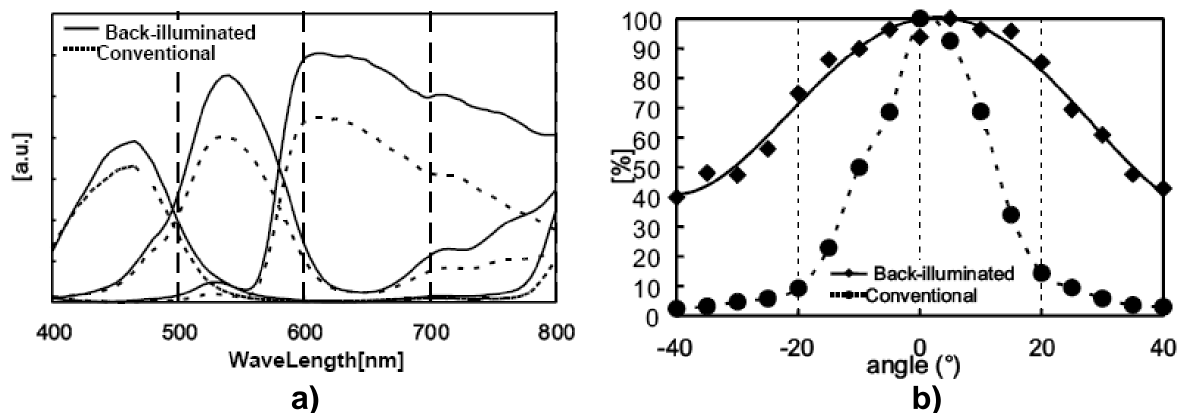

Figure 8-5. Comparison between FSI and BSI sensor a) quantum efficiency b) angular response [26].

A clear improvement in quantum efficiency was achieved with a backside illuminated sensor. This increases the sensor sensitivity making it highly suitable for use under low light conditions. A significant improvement can also be seen in the angular response. The conventional front side illuminated sensor is incapable of detecting light incident at high angles as the dielectric stack and metal wirings above the photodiode effectively prevent light from reaching the photodiode. A BSI sensor, on the other hand, allows a higher chief ray angle as light does not need to be focused on the photodiode through a narrow aperture between metal interconnects.

The main disadvantages of the BSI sensor are increased manufacturing cost and difficulties arising from wafer thinning. Before the backside of the wafer can be thinned, a handle wafer needs to be attached to the front for mechanical support during processing. The handle wafer is typically bonded using an adhesive or an oxide-oxide bond. A Silicon-on-insulator (SOI) wafer where a buried oxide layer

near the front surface of the silicon wafer acts as an etch stop layer can be used to simplify the thinning process. The substrate thickness plays an important part in BSI sensor design as it directly affects quantum efficiency and crosstalk performance. If the substrate is made too thin, longer wavelengths will not be absorbed due to the long penetration depth which consequently decreases quantum efficiency. On the other hand, if the substrate is too thick, shorter wavelengths are absorbed far away from the photodiodes which can also increase electrical crosstalk. [8, 20, 26, 27, 28]

8.4 Lightpipe architecture

Lightpipes can be used in image sensors to increase quantum efficiency and reduce angular dependency and optical crosstalk. A lightpipe in CIS functions similarly to a step index fiber discussed in Chapter 5 and can be achieved by utilizing a high refractive index core and a low refractive index cladding. The lightpipe structure is realized directly over the photodiode so that light is efficiently guided to the photoactive area via total internal reflection provided that the angle of incidence is higher than the critical angle. A high refractive index mismatch between the lightpipe and the surrounding dielectric is preferred as that will increase the lightpipe's acceptance angle. The lightpipe also reduces the focal length required from the microlens as light can be focused on the top of the lightpipe instead of on top of the photodiode. Thin and highly reflective metal cladding layers such as aluminum, copper, gold and silver deposited on the etched lightpipe walls acting as mirror surfaces have also been proposed. In this case the lightpipe fill material does not need to have a high refractive index as the light guiding effect relies on reflectance from the metal walls rather than total internal reflection. Cross-section illustrations of the three aforementioned lightpipe structures are shown in Figure 8-6 (a)-(c).

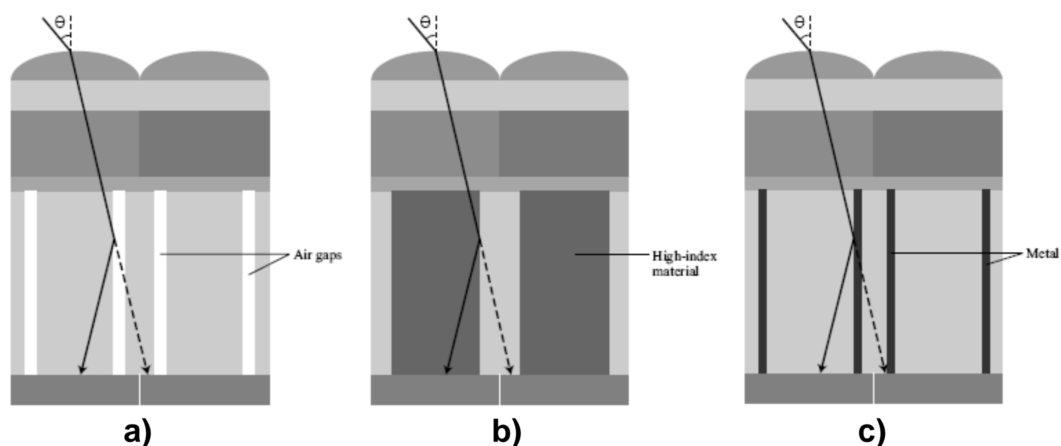

Figure 8-6. Illustrations of a) low refractive index cladding b) high refractive index core and c) metal cladding lightpipe structures [46].

Optical FDTD simulations done by Fesenmaier *et al*. for 1.75 μm pixel size for normally and 20° incident light showed that the low refractive index cladding approach was effective in terms of optical efficiency and crosstalk only when the air gap width was greater than 150 nm. Narrower gaps suffered from high crosstalk for off-axis light which can be explained by light escaping the core region via frustrated total internal reflection. Simulation results for the high refractive index core approach had a clear dependency on the core refractive index as expected. When the refractive index of the core material was above 1.60, the pixel performance was improved compared to the conventional structure without a lightpipe. Finally, the metal cladding which was modeled to be 100 nm thick, showed no improvement in optical efficiency while the crosstalk performance was superior. The biggest issue with the metal cladding approach is that, unlike typical dielectrics, metal absorbs light. In summary, the best overall performance in terms of optical efficiency and crosstalk was achieved with either using a 200 nm wide low refractive index cladding (air) around the pixel area or a high refractive index core. When comparing the low refractive index cladding and high refractive index core approaches, the latter has the additional benefit of better index matching to the color filter and silicon nitride films. Furthermore the high refractive index core does not require additional space inside the pixel as is the case with the low refractive index cladding which consumes valuable space on the pixel periphery. Although the crosstalk performance was by far the best with the metal cladding approach, optical efficiency was not very high which reduced the overall performance.

In addition to the optical performance one needs also to evaluate the manufacturability of the lightpipe structure. The low refractive index air cladding approach can have structural stability issues and contaminant diffusion from the color filter layer to the transistor areas can become a problem. Filling the air gaps with a low refractive index material greatly improves the device reliability but decreases the refractive index difference between the core and cladding leading to poorer optical performance. The high refractive index core approach is limited by the selection of materials available since the core material has to have a high refractive index, very low absorption and be able to fill deep via structures. Depositing a thin uniform layer of metal on the lightpipe sidewalls can also be challenging. Additionally, the metal deposited on the bottom of the lightpipe needs to be etched off and the lightpipe has to be re-filled with a dielectric material. A literature search on this subject revealed that the high refractive index core structure seems to be the most popular approach already adopted by CIS manufacturers, while only a few references were found on the low refractive index and metal cladding lightpipe structures. For this reason, a closer look will be taken on the high refractive index lightpipe design.

The lightpipe fill, or core, can basically be of any material that is optically transparent and has a higher refractive index than the surrounding dielectric which typically consists of alternating layers of SiO_2 and Si_3N_4. Core materials such as silicon nitride, polyimide and organic polymers have previously been reported. PECVD used for nitride deposition is however not a very effective method to fill up to several micrometer deep via structures as the deposition rate is slow and can end up having voids and keyhole defects. To prevent voiding during the deposition process, the lightpipe can be etched and filled sequentially after each ILD layer instead of using a single deep etch after the whole dielectric stack has been formed. This way the deposition of the nitride film becomes easier although it adds more steps to the device manufacturing process. Spin coating is inherently a much more suitable method for filling deep via structures as in addition to good gapfill performance it can also give a highly planarized surface. In the case of using a polyimide film as the lightpipe fill material, a liner material such as silicon nitride is needed to prevent metal impurity diffusion from the polyimide to the transistor areas. A hydrogen anneal is often used with the silicon nitride films allowing hydrogen to diffuse to the photodiode and reduce the amount of crystal defects. Color filter materials have also reportedly been used to fill the lightpipe eliminating the need for a separate CFA layer and reducing the optical path length as the microlens can be formed directly over the lightpipe. Figure 8-7 shows a cross-section image of a Tower Semiconductor 2.2 μm pixel size CMOS image sensor utilizing an organic polymer lightpipe with a refractive index of 1.54 at 650 nm wavelength. The lightpipe was etched through the dielectric stack after which a silicon nitride passivation layer was deposited and the lightpipe was filled with an organic polymer using spin coating.

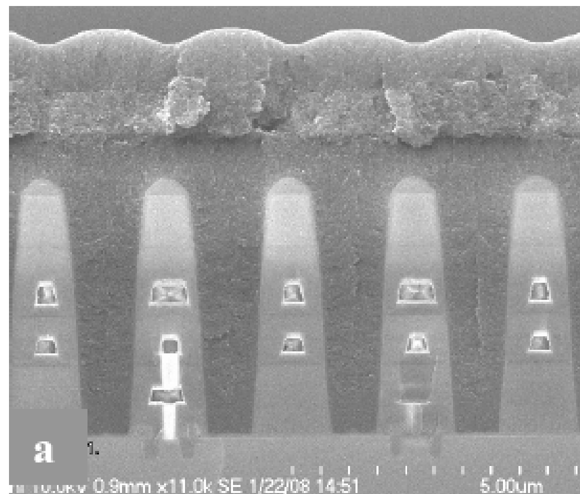

Figure 8-7. Cross-section SEM image of a CIS utilizing a lightpipe structure [42].

As seen from Figure 8-7, the lightpipe establishes a direct optical path from the focusing microlens to the photodiode. The shape of the lightpipe is slightly forward tapered so that the top of the lightpipe is wider than the bottom allowing more efficient light collection. The lightpipe layer can be planarized using, for example, chemical mechanical polishing (CMP), etch-back process or by applying a planarizing coating. A passivation layer can be deposited on top of the lightpipe to prevent outgassing from the lightpipe fill material during subsequent processing step or diffusion of contaminants to the photodiode and transistors from the color filter material which typically contains metallic impurities. [21, 29, 30, 31, 32, 33, 35, 42, 46]

9 Optical modeling of CMOS image sensors

The optical performance of a CMOS image sensor utilizing a lightpipe structure was modeled at Valtion Teknillinen Tutkimuskeskus (VTT) using the finite difference time domain (FDTD) method. The FDTD method numerically solves the time dependent Maxwell equations and can be used to model the propagation or energy flow of light. The benefits gained with a high refractive index lightpipe will be demonstrated at various pixel sizes by comparing the modeling results against a conventional CIS structure. Furthermore, a comparison will be made between different lightpipe structures which have been recently suggested for the CIS application. Finally, the effect of a microlens overcoat layer to the optical performance of an image sensor will be reviewed. The lightpipe and overcoat layer modeling parameters are based on the optical properties of Silecs' siloxane based polymers.

9.1 The lightpipe structure

As discussed in Chapter 8, the light collection efficiency of a pixel decreases due to downscaling. Several lightpipe based structures have been proposed to increase the amount of light reaching the photodiode thus improving the device performance. The basic structure of a CMOS image sensor unit cell used in the FDTD modeling to determine the effectiveness of a lightpipe is shown in Figure 9-1 below.

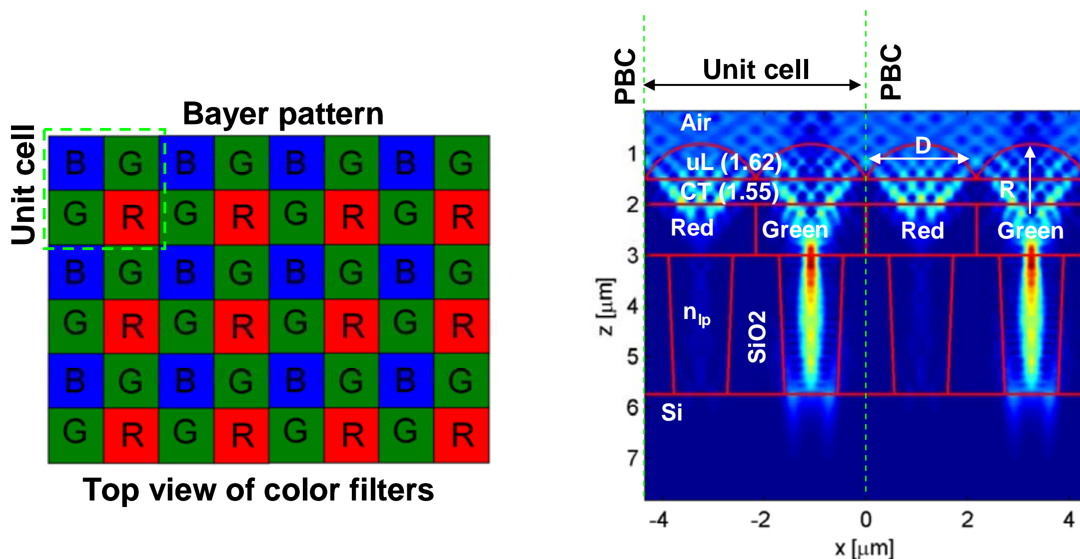

Figure 9-1. CIS structure used in FDTD Simulation [36].

The pixel's light collection efficiency and crosstalk are modeled for a TE-polarized plane wave at 530 nm wavelength. The equations used for defining the collection efficiency η and crosstalk CT are shown in Equations 9.1 and 9.2, respectively.

$$\eta = \frac{\int_{photodiode} S \cdot dA}{\int_{microlens} S^{(inc)} \cdot dA} , \tag{9.1}$$

where S is the time-averaged Poynting vector of the total field and $S^{(inc)}$ the time-averaged Poynting vector of the incident field.

$$CT = \frac{\int_{red\ photodiode} S \cdot dA}{\int_{green\ photodiode} S \cdot dA} = \frac{P_R}{P_G} \tag{9.2}$$

Figure 9-2 illustrates the effects of pixel size reduction on the propagation of light and the benefit of using a lightpipe structure especially with small pixels. Color is used to indicate the amplitude of the Poynting vector. Light is assumed to be normally incident and the microlens radius of curvature is kept constant at 3.0 μm.

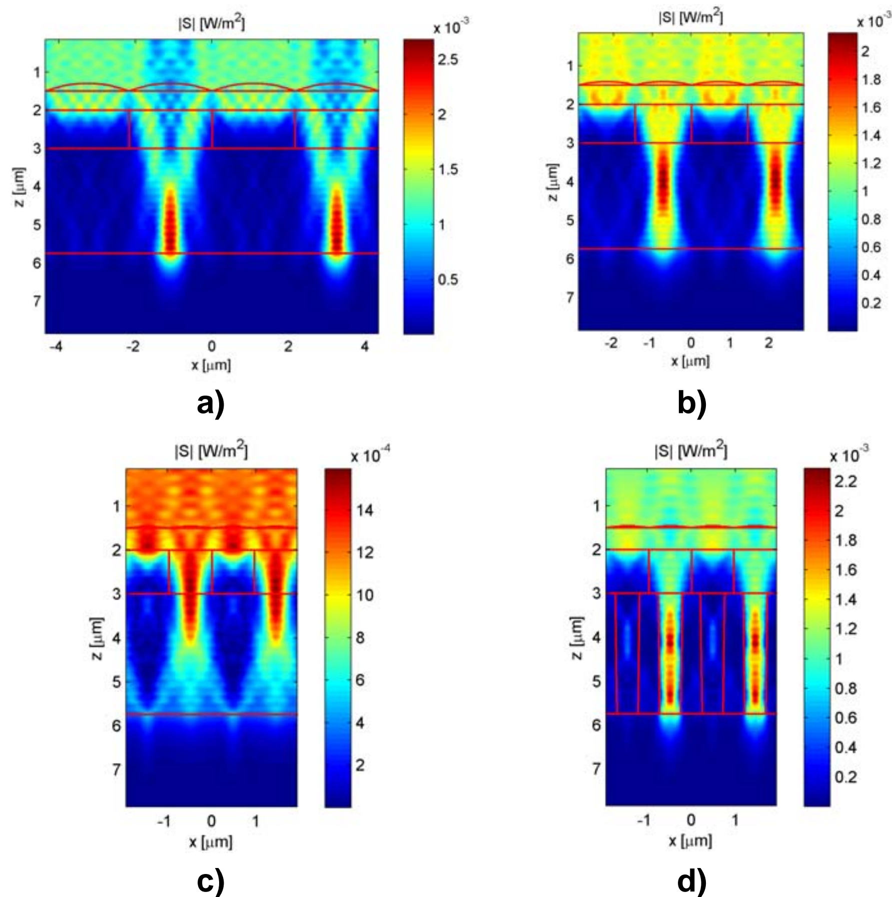

Figure 9-2. Simulated effects of pixel downscaling: a) 2.175 µm pixel b) 1.450 µm pixel c) 0.970 µm pixel and d) 0.970 µm pixel with a lightpipe [36].

The modeling results clearly show that pixel size reduction leads to poorer light collection efficiency and with 0.970 µm pixel size there is hardly any light reaching the photodiode. This is due to diffraction limitations when the pixel size is approaching the wavelength of light. The modeling result when using a high refractive index (n_{lp} = 1.670) lightpipe is shown in Figure 9-2 (d) for 0.970 µm pixel size. A significant improvement can be seen compared to the conventional structure due to the light guiding effect of the lightpipe. The calculated light collection efficiency and crosstalk as a function of angle of incidence for conventional and lightpipe structures are shown in Figure 9-3 for various pixel sizes.

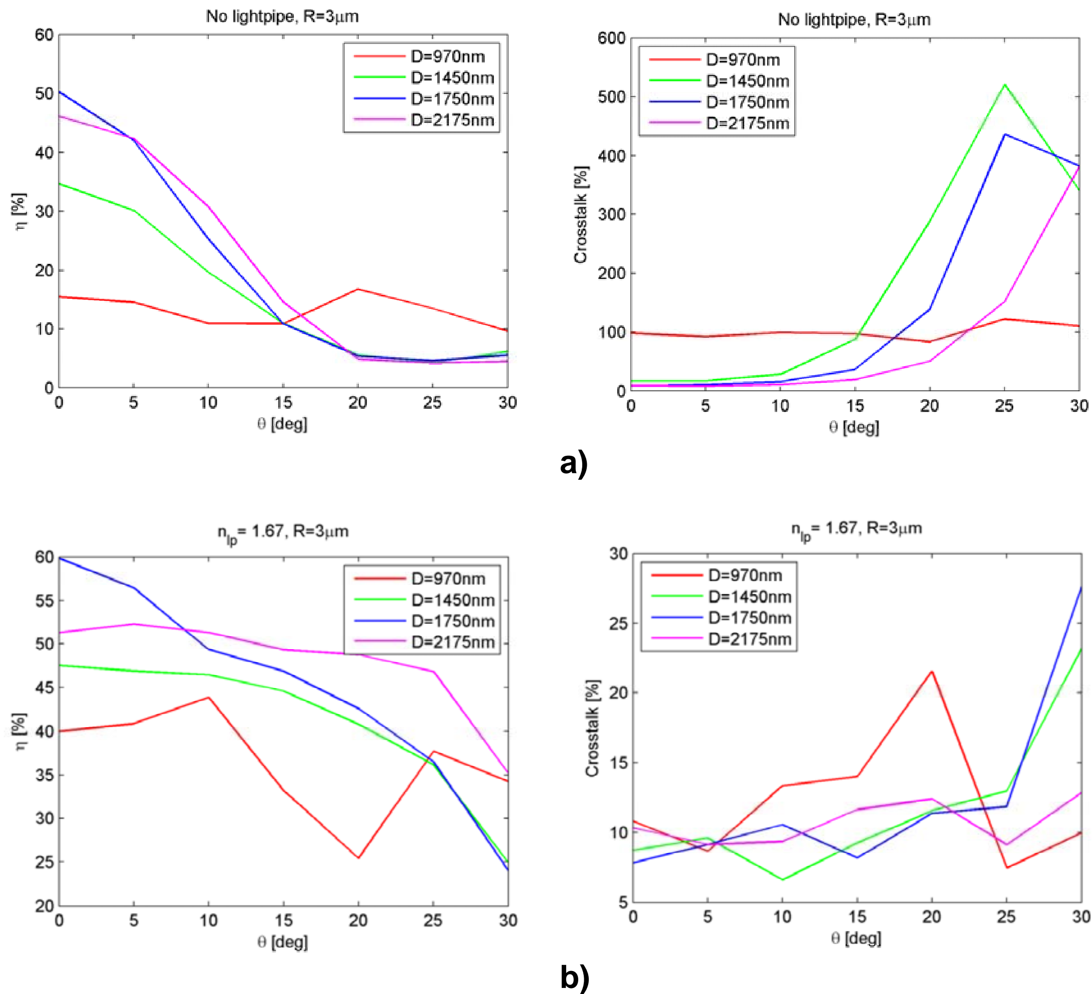

Figure 9-3. Simulated collection efficiency and crosstalk for a) conventional and b) lightpipe (n_{lp} = 1.67) structure CIS with various pixel sizes [36].

In a conventional CIS structure the light collection efficiency shown in Figure 9-3 (a) decreases rapidly with angle of incidence and pixel size. Crosstalk is higher for small pixels and increases sharply when the angle of incidence exceeds 15°. Higher than 100% crosstalk means that the amount of red light exceeds the amount of green light detected by a green pixel as shown by Equation 9.2. The 0.970 μm pixel size can be seen to be effectively non-usable for any imaging application due to its low collection efficiency and high crosstalk even for normally incident light. By employing a high refractive index lightpipe structure the collection efficiency can however be significantly increased especially for small pixel sizes as illustrated in Figure 9-3 (b). Angular dependency is reduced as the collection efficiency remains high also for off-axis light. A significant decrease in crosstalk,

especially for high angles of incidence, is achieved with the lightpipe structure which prevents the leakage of light through the dielectric stack to adjacent photodiodes. These improvements arise mainly from the reduction in the refractive index mismatches between the various layers in the optical path and due to the light guiding effect via total internal reflection.

A comparison was also made between different lightpipe structures. A highly reflective aluminum coating on the lightpipe walls as well as a low refractive index cladding layer and a lightpipe with higher refractive index were simulated. The idea behind the aluminum wall is to increase reflectance at the lightpipe-dielectric interface to improve the lightguiding effect. The low refractive index cladding, on the other hand, is used to increase the refractive index contrast and to lower the critical angle. Figure 9-4 shows the optical simulation results for the four different lightpipe designs. Light is incident at 25° angle on a 0.970 μm pixel with a microlens radius of curvature of 1.5 μm.

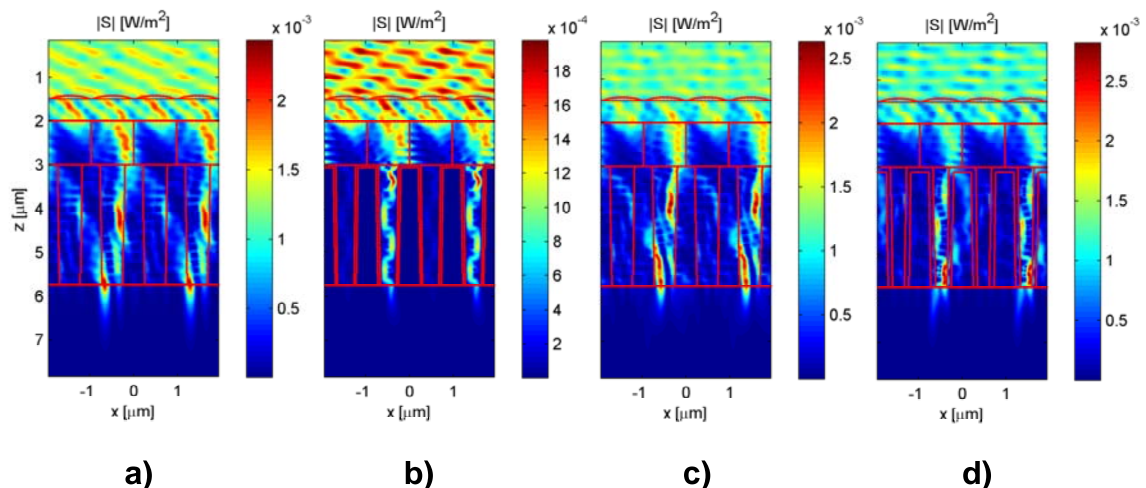

Figure 9-4. Simulation results for a) lightpipe with n_{lp} = 1.67 b) lightpipe with n_{lp} = 1.67 and 50 nm Al walls c) lightpipe with n_{lp} = 1.85 d) lightpipe with n_{lp} = 1.85 and 100 nm n = 1.28 cladding [36].

The light guiding effect can be clearly seen in Figure 9-4 (a)-(d) as light is reflected from the lightpipe sidewalls and travels towards the photodiode. Significant differences between the four lightpipe structures are observed as the amplitude of the Poynting vector at different locations are quite non-similar. The respective light collection efficiencies and crosstalk for the four lightpipe designs are shown in Figure 9-5. Results without using a lightpipe are included as reference.

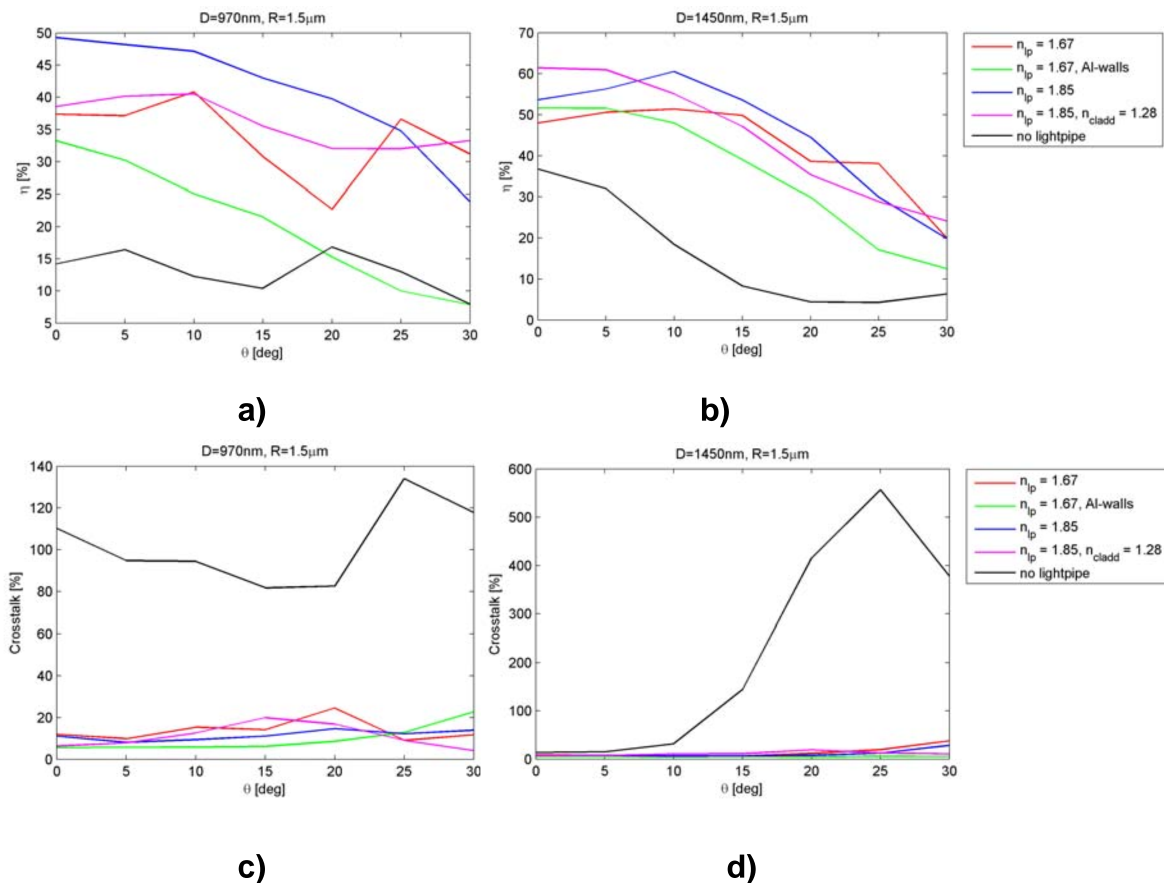

Figure 9-5. Simulated collection efficiencies for a) 0.970 µm and b) 1.450 µm pixel sizes and crosstalk for c) 0.970 µm and d) 1.450 µm pixel sizes with different lightpipe designs [36].

The highest collection efficiency was reached when the refractive index of the lightpipe was increased to 1.85. Crosstalk was also simulated to be low. Adding a low refractive index cladding layer (n_{cladd} = 1.28) on the other hand decreased collection efficiency, although some improvement was seen at high angles of incidence. The reduced performance is believed to be because the cladding layer was simulated to be only 100 nm thick and light managed to escape the lightpipe via frustrated total internal reflection. The structure where aluminum walls were used to increase reflectance from the lightpipe walls resulted also in lower collection efficiency. Although aluminum is highly reflective it also absorbs light leading to reduced performance. Crosstalk was however reduced as the aluminum layer effectively prevents light from escaping the lightpipe. Similar results were modeled for a larger 1.450 µm pixel size but compared to the conventional structure the difference was not as significant indicating that the lightpipe is more effective with smaller pixel sizes.

The optical simulation results showed the high refractive index lightpipe structure to be highly effective in increasing the collection efficiency and reducing crosstalk especially for small pixel sizes. Adding highly reflective metal walls or a low dielectric constant cladding to the lightpipe did not give any additional benefit and, in fact, resulted in poorer performance.

9.2 Microlens overcoat layer

A protective coating on top of the microlens layer has several benefits such as mechanical protection and reflectance reduction as was discussed in Chapter 7. Planar microlens overcoating layers with various refractive indices were modeled with the FDTD method to gain knowledge of the effects on optical performance.

In a typical CIS device light is incident from air to the microlens and the focal length is controlled by the shape of the lens. Depositing a protective coating on the lens array changes the focal length as light is incident on the lens from a layer with *n* > 1.0. Figure 9-6 illustrates the effect of having a planar overcoating layer with a refractive index between 1.1-1.4 deposited over the microlens array.

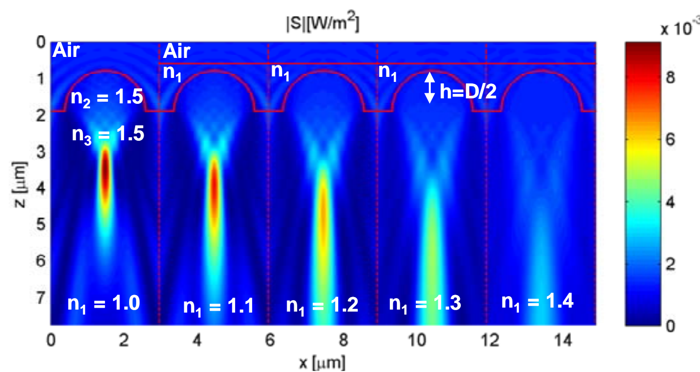

Figure 9-6. The effect of an overcoat layer to microlens focal length [36].

The focal length in Figure 9-6 can be seen to increase as a function of the overcoat refractive index. This is because the angle of refraction reduces according to Snell's law as the refractive index difference between the overcoat and microlens decreases. The corresponding collection efficiencies and crosstalk for 1.450 µm pixel size are shown in Figure 9-7.

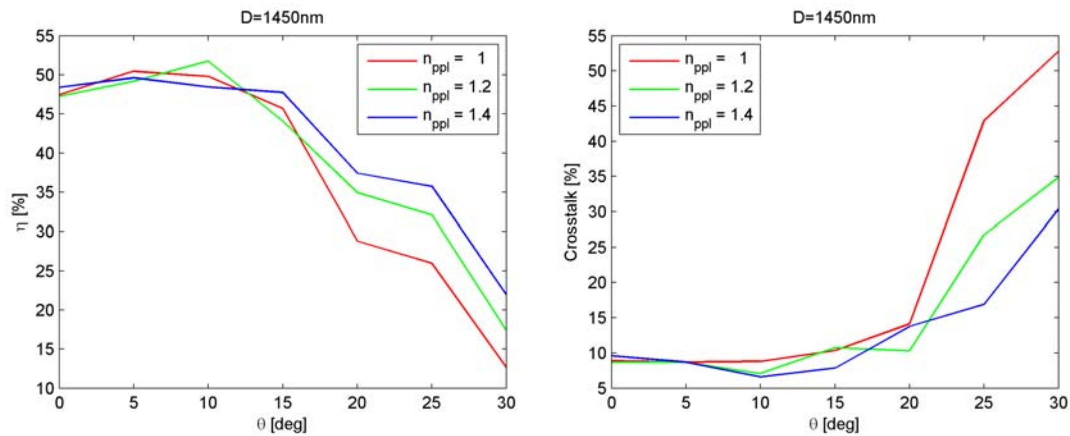

Figure 9-7. Collection efficiency and crosstalk for a 1.450 µm pixel size sensor when using an overcoat layer [36].

The simulation results show a slight increase in collection efficiency and a decrease in crosstalk at high angles of incidence with increasing overcoat refractive index. This can be explained by the focal spot of the microlens being closer to the photodiode and due to reduced reflectance as the overcoat acts also as an anti-reflective coating.

10 Siloxane polymers in optical applications

The benefits of using Silecs' spin-on dielectric materials in a CMOS image sensor lightpipe structure will be demonstrated in this chapter. After a short introduction to siloxane based polymers, some basic properties of Silecs' high refractive index materials are presented. Wafer level optical measurements from CMOS image sensors utilizing Silecs' polymers in the lightpipe are included to verify the simulation results presented in Chapter 9 and demonstrate the key advantages of the high refractive index lightpipe structure.

10.1 Fundamentals of siloxane polymers

The microelectronics industry uses a variety of polymers for applications ranging from interlayer dielectrics to passivation and packaging. The most commonly used types of polymers include acrylics, epoxies, polyimides and silicones among others. The polymer film properties such as thermal stability, electrical and mechanical performance and cost typically determine whether the polymer is suitable for a given application.

Siloxane or silsesquioxane polymers are widely used in photonic applications due to their good thermal and environmental stability, low moisture absorption, low optical loss and possibility to cover a wide range of refractive indices. Low absorption in the UV-visible-near infrared range and tunable refractive index makes these types of materials especially attractive as, for example, planar waveguide core and cladding layers. The monomer selection and polymer synthesis can be used to adjust material properties to meet the application specific requirements, while the spin-on deposition method offers fast and cost-effective wafer processing. The possibility for direct photolithographic patterning further increases material functionality.

The basic structure of a siloxane polymer with the empirical formula $R_1SiO_{3/2}$ is shown in Figure 10-1. It is an organic-inorganic hybrid polymer with a silicon-oxygen backbone which can form either ladder or cage like structures. By controlling the amount of hydrogen atoms or hydrocarbon groups R such as methyl (CH_3) and phenyl (C_6H_5) attached to the silicon-oxygen backbone, the polymer can be made polymeric or glass-like depending on the application requirements.

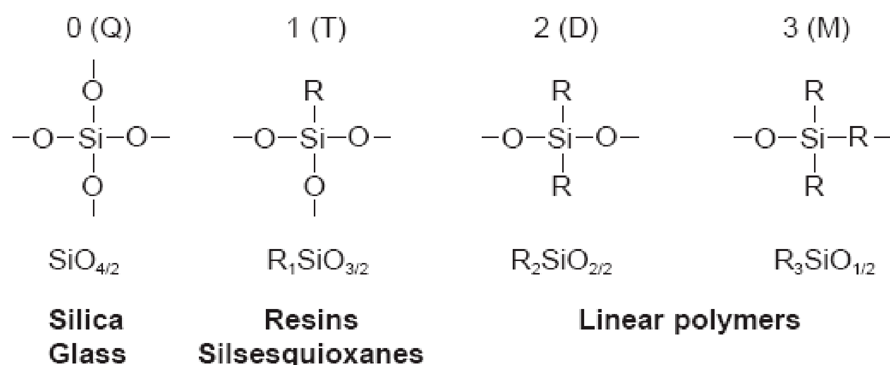

Figure 10-1. The basic structure of a siloxane polymer [40].

After polymer synthesis the material is dissolved into a solvent to enable deposition by spin-coating. Various surfactants, curing catalysts and other additives can be added to enhance the coating performance and facilitate cross-linking. The solid content along with wafer spin speed can be used to control the resulting film thickness which can range from tens of nanometers to tens of micrometers. Directly after spin-coating, the film is baked and cured either by thermally or by using ultraviolet radiation (or both) provided that suitable UV-curable functional groups are present in the polymer matrix. UV-curing is sometimes preferred over thermal curing due to faster cycle times. The main purposes of the bake and curing process steps are to remove the remaining solvents and to crosslink and densify the film to its final stable form. The two basic cure mechanisms for siloxane polymers are the condensation cure and addition cure. The bake and cure process play a significant role in determining the final film properties and need to be adjusted based on the material and application requirements for best performance.

The most commonly used siloxane based materials in the microelectronics industry are the hydrogen-silsesquioxane (HSQ) and methyl-silsesquioxane (MSQ) which are used as interlayer dielectric materials due to their low dielectric constant. These materials are typically cured or cross-linked at temperatures above 400°C through conversion of silicon hydride (Si-H) bonds to silanol (Si-OH) groups which in turn degrade and form the networked siloxane (Si-O-Si) structure. Curing is typically done in an inert atmosphere to prevent oxidation and decomposition of the polymer. The excellent planarization and gapfill properties of these types of polymers make them a highly attractive alternative to CVD oxides. [39, 40, 47, 49, 50, 53]

10.2 Silecs high refractive index polymers

There are several optical and thermo-mechanical requirements for the lightpipe material used in CMOS image sensors. The refractive index must be higher than that of the surrounding material to enable total internal reflection and the material must be optically highly transparent. Sufficient thermal and environmental stability is required for the material to be able to withstand the subsequent process steps and pass device reliability testing. Since the material will be within close proximity to the pixel's photodiode and transistor structures, it also has to be free of any contaminants which could degrade the device performance. Table 10-1 below shows basic film properties of Silecs' high refractive index siloxane polymers from the SC-product series. The materials have been specifically tailored to meet the requirements of the lightpipe application.

Table 10-1. Silecs SC300, SC400 and SC800 basic material properties.

	SC300(1)	***SC400***(2)	***SC800***(3)
Refractive Index @ 632.8nm	1.665	1.647	1.816(4)
Extinction coefficient (λ > 400nm)	<1.0E-3	<1.0E-3	<2.0E-3
Dielectric constant @ 100 kHz	3.6	3.2	7.5
Leakage current density @ 1.0 MV/cm field (nA/cm^2)	0.3	0.1	NA
Young's Modulus (GPa) (5)	7.0	8.3	18.9
Hardness (GPa) (5)	0.41	0.50	0.79
Stress @ RT (MPa)	37	49	NA
Film Shrinkage (%) (6)	2	4.5	9

(1) Film cured at 200°C / 5 min, (2) Film cured at 400°C / 60 min, (3) Film cured at 300°C / 10 min, (4) Refractive index is tunable, (5) Measured with nanoindentation, (6) Measured between softbake and final cure.

The film thickness, refractive index and extinction coefficients were measured with a Woollam M-2000D spectroscopic ellipsometer. Agilent 4294A precision impedance analyzer and 4155B semiconductor parameter analyzer were used to determine the dielectric constant and leakage current of the films from a metal-insulator-semiconductor structure. The nanoindentation measurements for determining the Young's modulus and hardness were performed using an MTS System Corp. Nano Indenter DCM with a Berkovich tip. A Tencor FLX-2320 thin film stress measurement tool was used to measure the film stress after cure.

The dispersion curves for SC300, SC400 and SC800 materials are plotted in Figure 10-2. The refractive indices can be seen to be significantly higher than what

is typically achieved with siloxane based polymers. The SC300 and SC400 materials have fairly similar refractive indices, while SC800 offers much higher values across the visible spectrum.

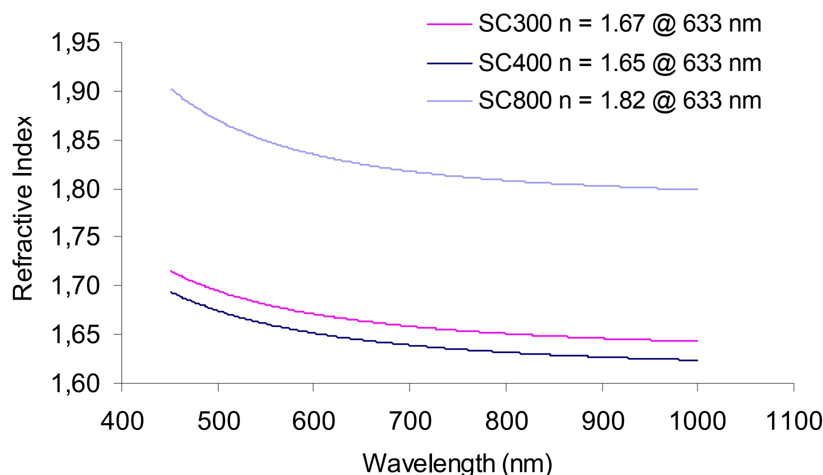

Figure 10-2. SC300, SC400 and SC800 dispersion curves.

Despite the similarities in optical properties, the SC300 and SC400 materials are quite different from each other. SC300 is a low temperature curable material which can be fully crosslinked at approximately 200°C making it a suitable material for both color filter planarization and lightpipe applications. The SC400 material on the other hand is typically cured via polycondensation at between 250°C – 450°C depending on the device process flow and can withstand typical CIS back-end process temperatures. Low outgassing during cure comprising mainly of residual solvents, water and low-molecular weight organic components yields low film shrinkage and low residual stress. Both materials are highly transparent in the visible spectrum and have excellent gapfill performance required to successfully fill the lightpipe structures without defects such as voids. They also provide good electrical insulation due to low leakage current. The SC800 polymer is fairly similar to the SC400 but has metal oxide nanoparticles incorporated into the polymer matrix to increase the film refractive index. By controlling the nanoparticle loading, the refractive index of the SC800 can be effectively tuned between 1.7 – 1.9. A fairly linear relationship exists between the nanoparticle loading concentration and refractive index. A higher refractive index is beneficial to the lightpipe performance as discussed previously in Chapter 9. The nanoparticles also have a significant effect to the mechanical and electrical properties of the polymer as seen from Table 10-1. [49, 53]

10.3 Silecs polymers in CIS lightpipe application

An IBM 2.2 µm pixel size CMOS image sensor device utilizing 4T-shared pixel architecture and Cu interconnects was used to test the Silecs high refractive index polymers device level performance. After opening the lightpipe cavity above the photodiode, the SC400 and SC800 films were spin-coated on the 200 mm test wafers to fill the lightpipe. The polymer films were cured according to conditions in Table 10-1 after which the color filter and microlens layers were formed to complete the sensor. Figure 10-3 shows a cross-section image of a pixel array after completing the sensor process. The lightpipe structure etched through the dielectric stack with alternating layers of SiO_2 and Si_3N_4 is slightly forward tapered and has a thin silicon nitride capping layer deposited for passivation purposes.

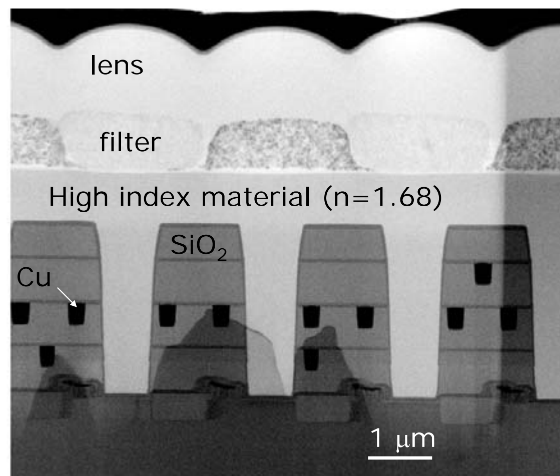

Figure 10-3. Cross-section image of SC400 in IBM 2.2 µm pixel size CIS [21].

The aspect ratio of the approximately 2.7 µm deep lightpipe is 4:1 and shows the excellent planarization and gapfill properties of SC400. No voiding, delamination or other defects are seen. The thickness of the material can be further adjusted by spin speed or material solid content to give a minimum amount of material on top of the lightpipe to reduce the optical path length and to avoid additional etch-back or CMP process steps.

10.3.1 Quantum efficiency and angular response measurements

After color filter and microlens formation, wafer level optical performance of the IBM 2.2 µm pixel size sensor utilizing the SC400 and SC800 lightpipe structures

was tested. A monochromator with varying wavelength (400 nm - 750 nm) was used to determine the image sensor quantum efficiency. Figure 10-4 shows the measured quantum efficiencies for an image sensor with the conventional dielectric stack structure with comparison to the SC400 and SC800 lightpipe structures.

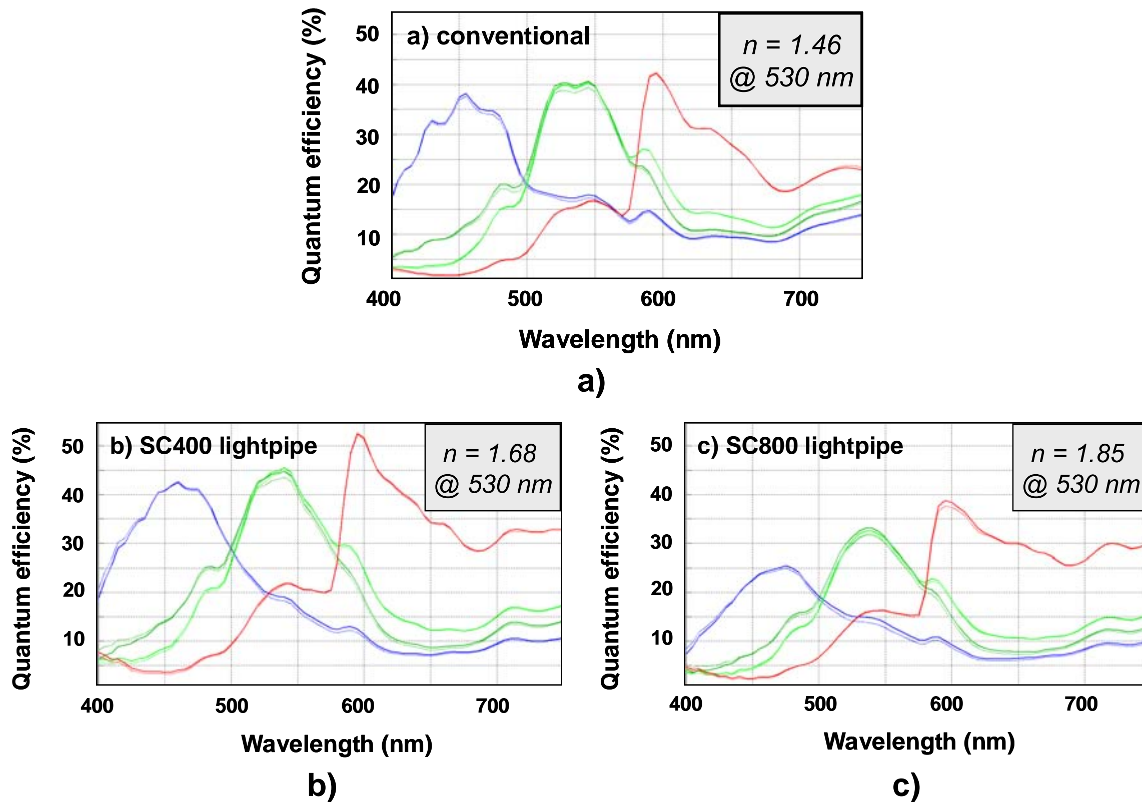

Figure 10-4. Quantum efficiencies measured from a) conventional b) SC400 lightpipe and c) SC800 lightpipe structures [21].

In the case of the SC400 in Figure 10-4 (b), the quantum efficiency can be seen to have significantly improved for all the primary colors compared to the reference structure shown in Figure 10-4 (a). The improvement is due to higher collection efficiency for off-axis light as the focal point is shifted from the photodiode surface to the lightpipe entrance. Also reflections from the bottom of the color filter and silicon wafer surface have reduced due to better index matching. According to Equation 3.7, the reflectances at the bottom of the lightpipe for normally incident light at 530 nm are 1.8% and 2.6% lower with SC400 and SC800, respectively, compared to when using silicon dioxide. See Table 10-2 for the calculated reflectance values.

Table 10-2. Reflectance for normally incident light at 530 nm.

Interface	*Reflectance (%)*
SiO_2 / Si_3N_4 / Si (n = 1.46 / 2.05 / 4.14)	14.2
SC400 / Si_3N_4 / Si (n = 1.68 / 2.05 / 4.14)	12.4
SC800 / Si_3N_4 / Si (n = 1.85 / 2.05 / 4.14)	11.7

Although theoretically the higher refractive index SC800 polymer should give better performance compared to the SC400, the optical measurements show the quantum efficiency to be significantly lower even when compared to the conventional structure. Transmittance curves for the SC400 and SC800 polymers shown in Figure 10-5 for the visible part of the electromagnetic spectrum provide an explanation for this. To measure transmittance the films were coated and cured on a 2 mm thick B270 crown glass substrate which is highly transparent down to approximately 360 nm. The measurement was done using a Perkin Elmer Lambda 950 UV/Vis/NIR spectrometer with an integrating sphere.

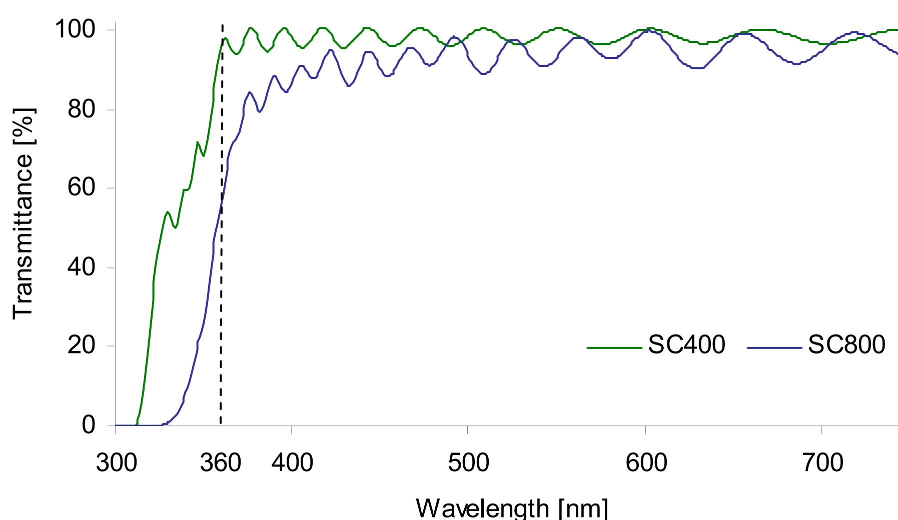

Figure 10-5. SC400 and SC800 transmittance at 1.85 μm film thickness.

While the SC400 can be seen to exhibit excellent transmittance throughout the visible spectrum, the SC800 has lower transmittance especially at shorter wavelengths. This can be explained by light scattering from the metal oxide nanoparticles dispersed into the SC800 polymer film. Some absorption of light may also be taking place. The scattering of light in the SC800 occurs not only because of physical inhomogeneity in the film but also because of the large difference in

refractive index between the polymer and the nanoparticles. A surface coating on the nanoparticles is used to prevent agglomeration which could lead to increased optical scattering. To verify that the nanoparticles in SC800 are uniformly dispersed and no agglomeration is actually taking place, cross-section TEM analysis of the SC800 solution and a cured film were made. The TEM images are presented in Figure 10-6 and show no significant nanoparticle clustering or agglomeration.

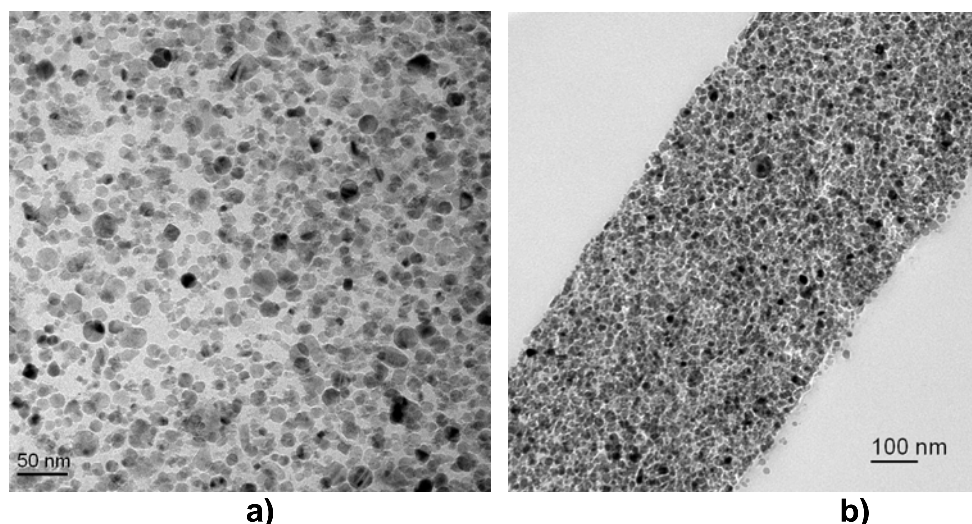

Figure 10-6. TEM images of SC800 a) solution b) cured film.

The diameter of the nanoparticles in SC800 can be seen to be in the order of tens of nanometers which results in reduced transmittance especially at short wavelengths due to Rayleigh scattering. As discussed in Chapter 4.1, Rayleigh scattering occurs when the particle size is approximately one-tenth of the wavelength of light. Rayleigh scattering is highly wavelength dependent and is about ten times stronger for blue light compared to red light. This can be seen in Figure 10-5 where the transmittance of SC800 is the lowest in the blue end of the visible spectrum and increases with wavelength as the scattering power reduces and more light passes through the film without being scattered or redirected from its original path. The effect of Rayleigh scattering can also be seen in the quantum efficiency measurements shown in Figure 10-4 as shorter wavelengths yield clearly lower quantum efficiency for the SC800.

Surface scattering induced by surface roughness is another scattering mechanism which can lead to additional optical losses. To characterize the SC800 film surface roughness, an atomic force microscope (AFM) scan was made. Figure 10-7 shows an AFM scan image from a 1 µm x 1 µm surface area of the SC800 film.

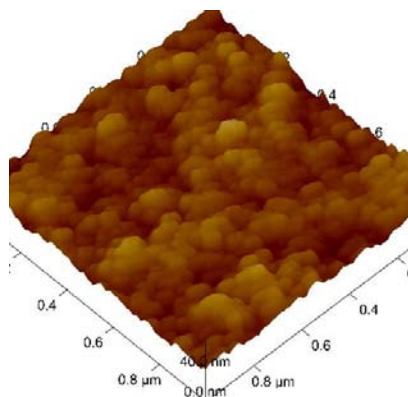

Figure 10-7. An AFM scan image of SC800 film with RMS of 4.6 nm.

The root mean square (RMS) roughness parameter was found to vary between 3-6 nm, which is high enough to create some scattering also at the film surface. [1, 52]

The angular dependency of the IBM 2.2 µm pixel size sensor with conventional and lightpipe structures using the SC400 and SC800 materials were measured at 450 nm, 535 nm and 610 nm wavelengths. The same test setup as in the quantum efficiency measurements was used with varying the angle of incident light. The light intensity as a function of incident angle for blue and red light is shown in Figure 10-8.

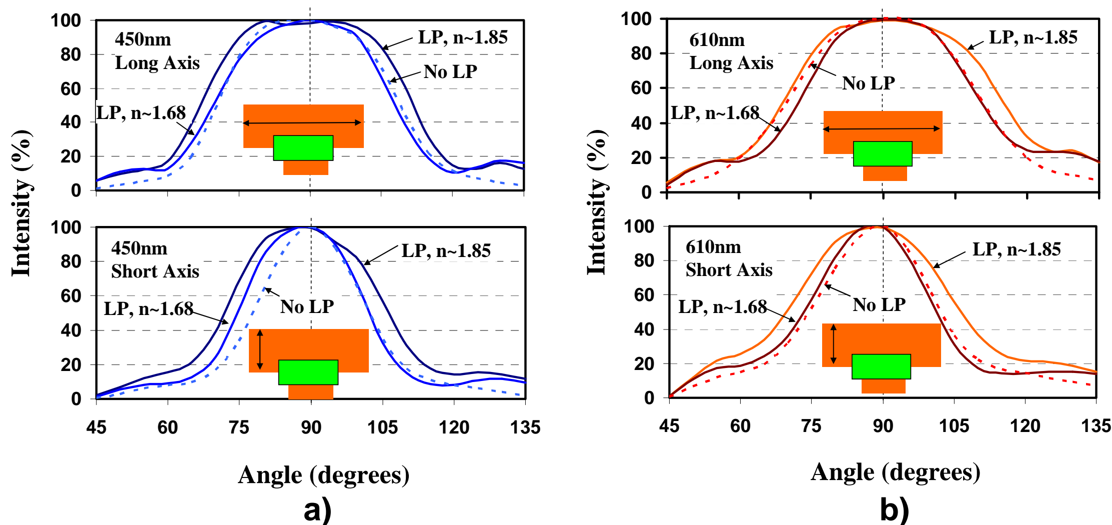

Figure 10-8. Angular response measured for a) blue light and b) red light [21].

The angular response of the rectangular pixel was measured in both the short and long axis directions. For blue and red light a clear improvement was seen especially when using the higher refractive index SC800 material. The lower critical angle achieved with the SC800 clearly increased the collection efficiency of off-axis light. Crosstalk values calculated from the quantum efficiency measurements are shown in Table 10-3 for the SC400 and SC800 lightpipe structures and compared against the conventional structure.

Table 10-3. Crosstalk in IBM 2.2 µm pixel size sensor.

Crosstalk	***No lightpipe (n = 1.46)***	***SC400 lightpipe (n = 1.68)***	***SC800 lightpipe (n = 1.85)***
Green @ 450 nm	31%	26%	25%
Red @ 550 nm	54%	51%	52%
Green @ 650 nm	31%	30%	30%

A clear improvement was found especially at 450 nm wavelength where the amount of green light detected by blue pixels had reduced by 5-6%. The improvement in crosstalk is a clear indication of better light guiding due to the high refractive index lightpipe structure. The differences in crosstalk between the SC400 and SC800 were not however very significant.

In summary, the lightpipe structure with a highly transparent SC400 high refractive index (n = 1.68 @ 530 nm) fill material was found to significantly improve the quantum efficiency and reduce crosstalk in the IBM 2.2 µm pixel size CMOS image sensor. The performance was improved compared to what has previously been reported by Gambino *et. al* when using an organic polymer lightpipe with a refractive index of 1.60 in a similar structure. Although the SC800 material (n = 1.85 @ 530 nm) showed clear improvement in angular response, the quantum efficiency was measured to be low. This was considered to be because of the low transmittance especially at short wavelengths due to scattering and possible absorption effects. Further material optimization is needed to increase the SC800 optical performance especially at short wavelengths.

11 Microlens overcoat layer

An overcoat layer on top of the microlens array found in modern CIS and CCD devices can improve the image sensor performance in several ways. By tuning the refractive index and film thickness, the overcoat can act as an anti-reflective coating decreasing the amount of light reflected from the microlens surface. Furthermore, the refractive index can be used to adjust the focal length of the microlenses giving some additional freedom in the lens design. The overcoat layer can also act as a passivation layer and protect the microlenses against silicon particles originating from the die sawing process resulting in improved yield. Materials such as silicon dioxide and organic photoresists have been previously used for the overcoat application. Both materials have, however, relatively high refractive indices (n ~1.46 and n ~1.55) and are, therefore, not very effective anti-reflection layers on top of a microlens film. Organic photoresists are also very soft and can absorb light if not removed after the die sawing process. [15, 42]

11.1 Anti-reflection coating

The refractive index of a typical commercially available microlens film is approximately 1.6 in the visible spectrum of light. When light is incident from air to the lens surface, significant reflections can occur due to the large refractive index mismatch. An overcoat layer with a suitable refractive index and film thickness can be used to effectively suppress reflections thus increasing the amount of light received by the sensor. Figure 11-1 shows the reflectance for an air/overcoat/microlens layer as a function of overcoat thickness and refractive index. Although both the microlens and overcoat layers were assumed to be flat and fully transparent in the calculations, a good approximation of the reflectance as a function of film thickness, refractive index and incident wavelength can be made.

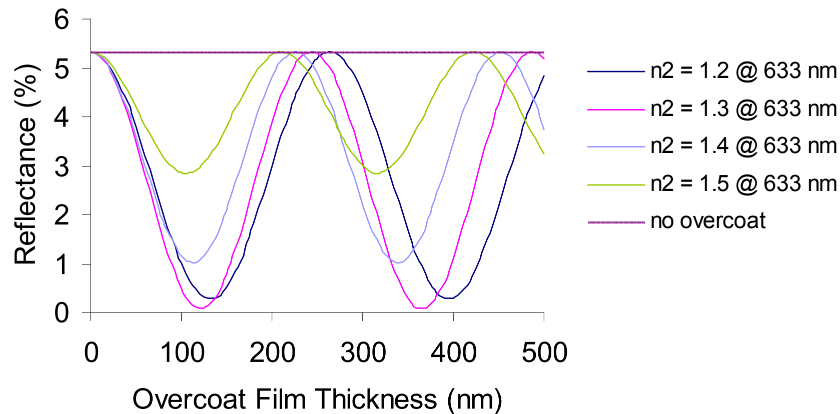

Figure 11-1. Reflectance in an air/overcoat/microlens interface as a function of overcoat film thickness and refractive index (n_1 = 1.0, n_3 = 1.6, λ = 633 nm, θ_i = 0°).

As seen from Figure 11-1, film thickness as well as refractive index of the overcoat needs to be optimized to achieve minimum reflectance. The peaks and valleys result from constructive and destructive interference as discussed in Chapter 3.2.1. The lowest reflectance for normally incident light is reached when the optical thickness of the film is exactly one quarter of the incident wavelength (according to Equation 3.8) satisfying the condition for destructive interference. The highest reflectance, which is equal to having no overcoat, on the other hand is achieved when the film thickness is half of the incident wavelength in which case constructive interference occurs. The optimum refractive index and film thickness values for an anti-reflection coating on a microlens layer with refractive index of 1.60 were calculated to be 1.26 and 126 nm, respectively. The calculation was done at 633 nm wavelength. Figure 11-2 shows how the reflectance varies with the incident wavelength and angle when using the optimum film thickness and refractive index values.

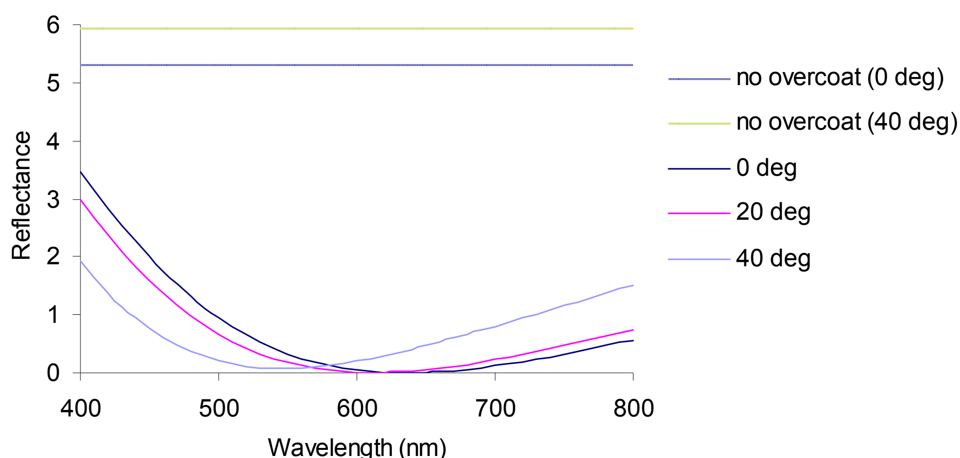

Figure 11-2. Reflectance in an air/overcoat/microlens interface as a function of wavelength for various angles of incidence (n_1 = 1.0, n_2 = 1.26, n_3 = 1.6).

The lowest reflectance for normally incident light is reached at 633 nm for which the anti-reflection coating was optimized to. Both longer and especially shorter wavelengths can however be seen to have increased reflectance. This is due to the fact that the quarter wavelength thickness rule cannot be satisfied for all wavelengths simultaneously leading to incomplete destructive interference due to phase changes between light reflected from the surface of the anti-reflection coating and the underlying film. The angle of incident light also affects the amount of reflected light because the distance light travels in the anti-reflection coating material changes which again leads to phase changes. Despite the above, the overcoat layer still manages to significantly reduce the reflectance across the visible spectrum.

11.2 Silecs spin-on overcoat materials

The selection of suitable overcoat materials for the CIS application is narrowed down not only by the low refractive index requirement but also by the need for low temperature deposition as both the color filter and microlens materials start to typically degrade at temperatures exceeding 250°C. Figure 11-3 shows the dispersion curves for two Silecs siloxane based spin-on materials designed for the microlens overcoat application. Silicon dioxide is included as a reference. Both SC200 and SC500 films can be fully cured at approximately 200°C and have refractive indices between 1.0 and 1.60 making them highly suitable for the microlens overcoat application.

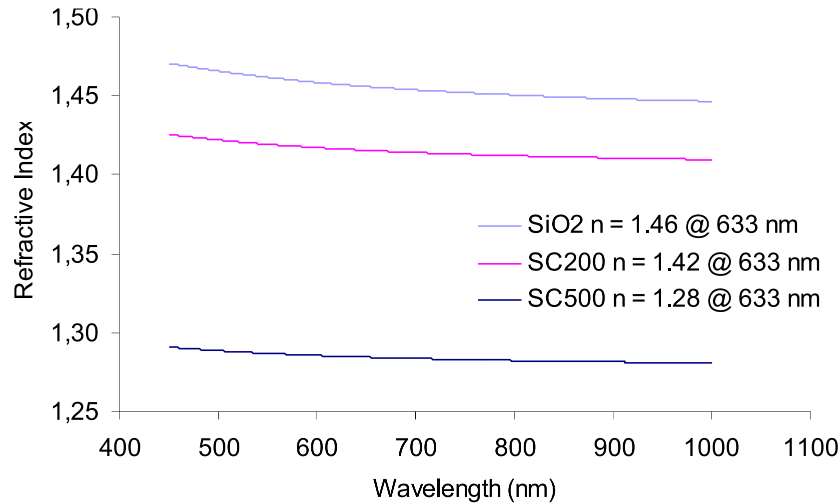

Figure 11-3. SiO_2, SC200 and SC500 dispersion curves.

The refractive indices of SC200 and SC500 can be seen to remain fairly constant throughout the visible spectrum and only a slight increase is detected at shorter wavelengths. The Abbe number, which is used to describe the dispersion of glasses, was calculated to be 40, 54 and 58 for SiO_2, SC200 and SC500, respectively. Low dispersion, i.e. high Abbe number, is highly desirable for an anti-reflection coating since it helps to reduce the wavelength dependency of reflectance.

Figure 11-4 shows the calculated reflectance values from the air/overcoat/microlens interface when using the SC200 and SC500 films as the overcoat material. The reflectance without using an overcoat layer is shown as reference. As before, the microlens curvature was not taken into account in the calculations and all layers were assumed fully transparent.

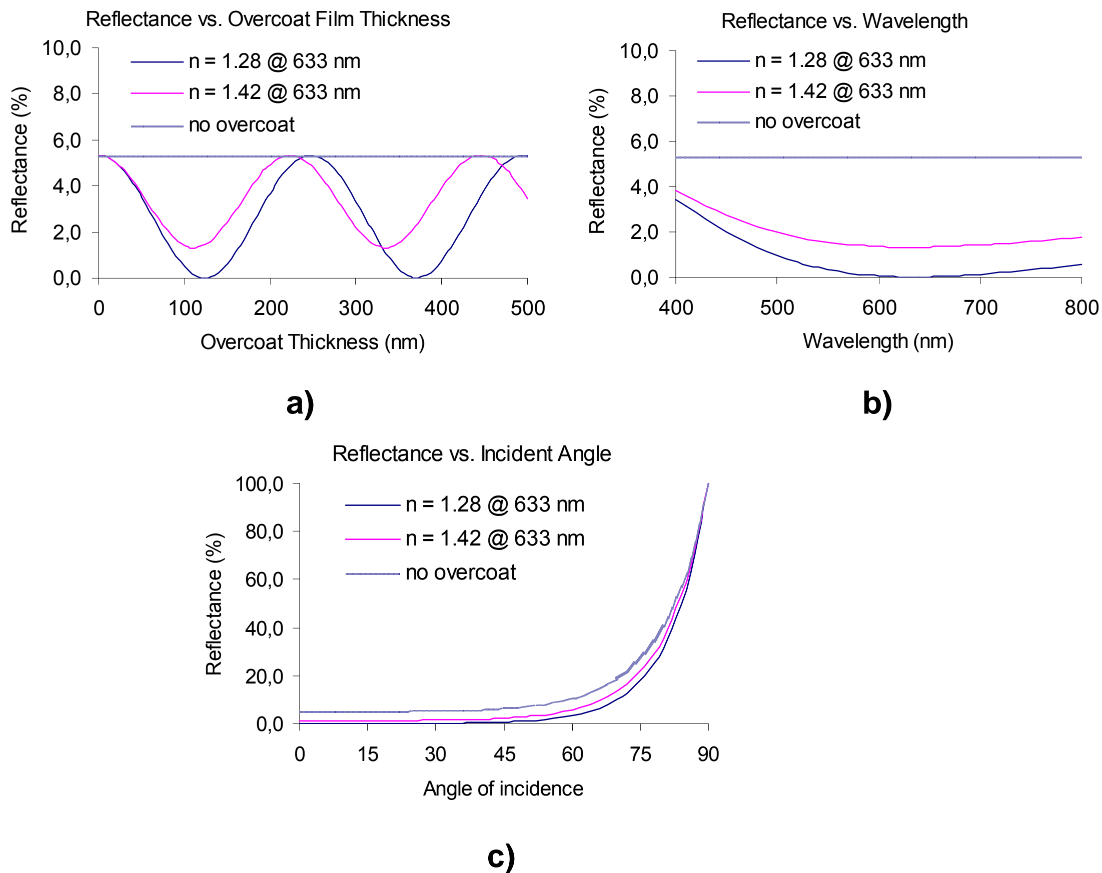

Figure 11-4. Reflectance in an air/overcoat/microlens interface as a function of a) overcoat film thickness (λ = 633 nm, θ_i = 0°) b) incident wavelength (θ_i = 0°) c) angle of incidence (λ = 633 nm).

The reflectance plotted as a function of film thickness in Figure 11-4 (a) can be seen to reach a much lower level with the SC500 since its refractive index is closer to the optimum value of 1.26. In Figure 11-4 (b), the reflectance is shown as a function of wavelength for normally incident light. Film thicknesses yielding the lowest reflectance at 633 nm according to Equation 3.8 were used in the calculations. The reflectance can be seen to vary slightly which is typical for single coat anti-reflective coatings that can be optimized only for a specific wavelength. Finally, the reflectance is shown as a function of angle of incidence in Figure 11-4 (c). As seen from Figure 11-4 (a) to (c), the reflectance can be significantly reduced with the use of a low refractive index overcoat with optimized film thickness. The SC500 material yields lower reflectance compared to the SC200 due to better refractive index match for anti-reflection with the microlens material. The SC200 offers some process simplification through its possibility for direct photopatterning which removes the need for lithography and etch processes used for contact pad

opening. Photopatternable polymers will be discussed with more detail in Chapter 11.3. A cross-section SEM image of a 2.8 µm pixel size CMOS image sensor with an SC200 overcoat layer on the microlens array is shown in Figure 11-5.

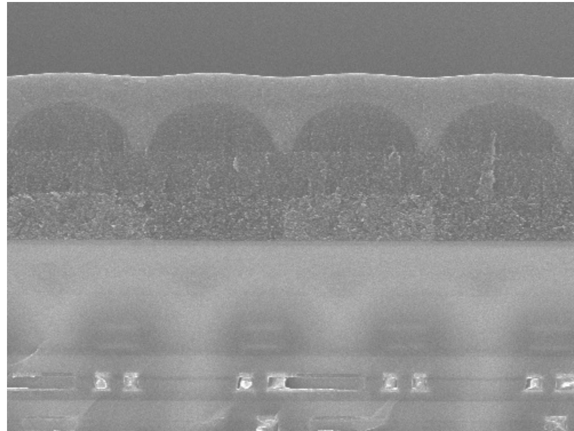

Figure 11-5. SC200 coated on top of Tower Semiconductor 2.8 µm pixel size CIS microlens array [42].

The SC200 overcoat layer is planarizing the microlens array thus providing both passivation and protection for the soft lens material as well as an easy to clean surface. As discussed earlier, the reflectance is reduced as the overcoat has a refractive index between 1.0 and 1.60. It should be however noted that the focal length of the microlenses will also be affected by the overcoat as the angle of refraction changes according to Snell's law when the refractive index of the medium from which light enters the microlens increases. Conformal rather than planarizing overcoat layers can be used to reduce the impact on the focal length but in this case the film needs to be very thin to be able to retain the shape of the microlens. Furthermore, a thin overcoat may not be an effective passivation layer and the surface may be more difficult to clean from silicon dust and particles after the die sawing process. The deposition of a conformal overcoat layer can also be challenging using spin coating and the alternative chemical vapor deposition (CVD) has limitations regarding the deposition temperature and the achievable refractive index range.

Spin coating of highly transparent low refractive index materials with good mechanical and passivation properties can result in a significant improvement in device performance due to reduced reflectance. Improvements in yield through better protection of the microlens array and reduced cost of processing with spin coating and direct photopatterning are additional key benefits.

11.3 Photopatternable overcoat

The microlens overcoat is the last layer deposited on the wafer before die sawing and packaging. The overcoat layer above the bonding pads needs however first to be removed to allow wire bonding to electrically connect the CIS chip to the package leads. Typically this is done using standard lithographic and etching techniques but a photopatternable overcoat material can greatly simplify the process. Resist coating, etching, resist strip and cleaning steps can all be omitted if the overcoat film can be directly patterned to form the desired topography on the substrate thus leaving the areas directly above the bond pads clear.

Photopatternability can be achieved in siloxane based polymers provided that certain UV-sensitive functional groups such as acrylates or epoxies are present in the polymer matrix and a photoinitiator is added to initiate the polymerization of the said functional groups. The photoinitiator is typically either of radical or cationic type. The radical type initiators function by absorbing UV-light and producing free radicals which start the polymerization or cross-linking process. Rapid curing occurs when using a high intensity UV-light source. The free radical curing is sensitive to oxygen which can inhibit the curing process but an inert atmosphere or oxygen scavengers in the polymer can be used to prevent this. Cationic type initiators, on the contrary, form an acid catalyst molecule upon exposure to UV-light which then initiates the cross-linking process in which monomers and oligomers form a high molecular weight polymer structure. The cross-linking process continues after the UV-light is removed and until all the photoinitiator has been depleted. A short bake step after the UV exposure is often done to speed up and complete the process. An inert atmosphere is not required as in the free radical case since the cationic type curing is not sensitive to oxygen. Commonly used cationic type photoinitiators include arylsulfonium hexafluoroantimonate ($Ar_3S^+SbF_6^-$) and arylsulfonium hexafluorophosphate salts ($Ar_3S^+PF_6^-$). In both radical and cationic photoinitiator cases the cross-linked or exposed areas become insoluble to the developer and the material behaves essentially like a negative tone photoresist.

Silecs photopatternable microlens overcoat materials, such as the SC200, offer enhanced device performance as well as process simplification. After coating the film is softbaked and selectively exposed to UV light to initiate the polymerization of the exposed areas. A post exposure bake renders the exposed areas insoluble to the developer solution while the non-exposed areas can be washed off. The film can be developed with a standard aqueous 2.38w% tetramethylammonium hydroxide (TMAH) solution making it highly compatible with standard lithographic processes. Finally the patterned film is cured for further cross-linking thus allowing the film to reach a final stable form. A typical contrast or response curve used to determine the sensitivity of a material to UV-light is shown in Figure 11-6. The films

were exposed using a Canon FPA-2500 i3 i-line stepper with exposure doses ranging from 0-260 mJ/cm^2 with 20 mJ/cm^2 increments. The final cure was performed at 210°C on a hotplate under nitrogen ambient.

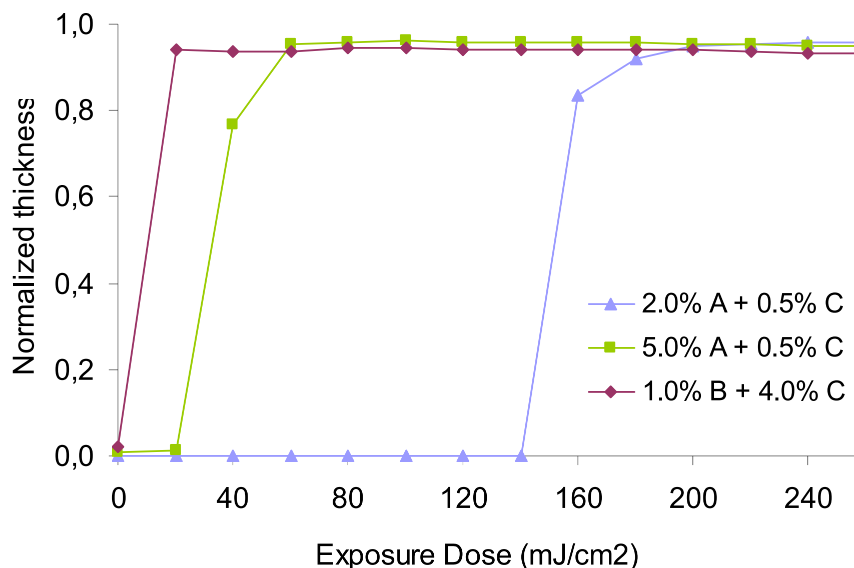

Figure 11-6. Contrast curve normalized to the remaining thickness (A & B = photoinitiator, C = thermal catalyst).

The photoinitiator type and loading can be seen to have a dramatic effect on the material sensitivity as the same polymer yields very different contrast curves. Generally lower exposure doses, i.e. higher photospeed, is preferred, as the time required to fully expose the film decreases. This is especially true when using steppers and large diameter wafers where just a few seconds shorter exposure time per die can significantly increase wafer throughput. The contrast curve is not however the only parameter affected by the photoinitiator type and loading and often compromises need to be made between, for instance, sensitivity, pattern quality, resolution, electrical performance and optical properties. Figure 11-7 shows a collection of SEM images demonstrating the various challenges encountered during the research and development of photopatternable polymers at Silecs.

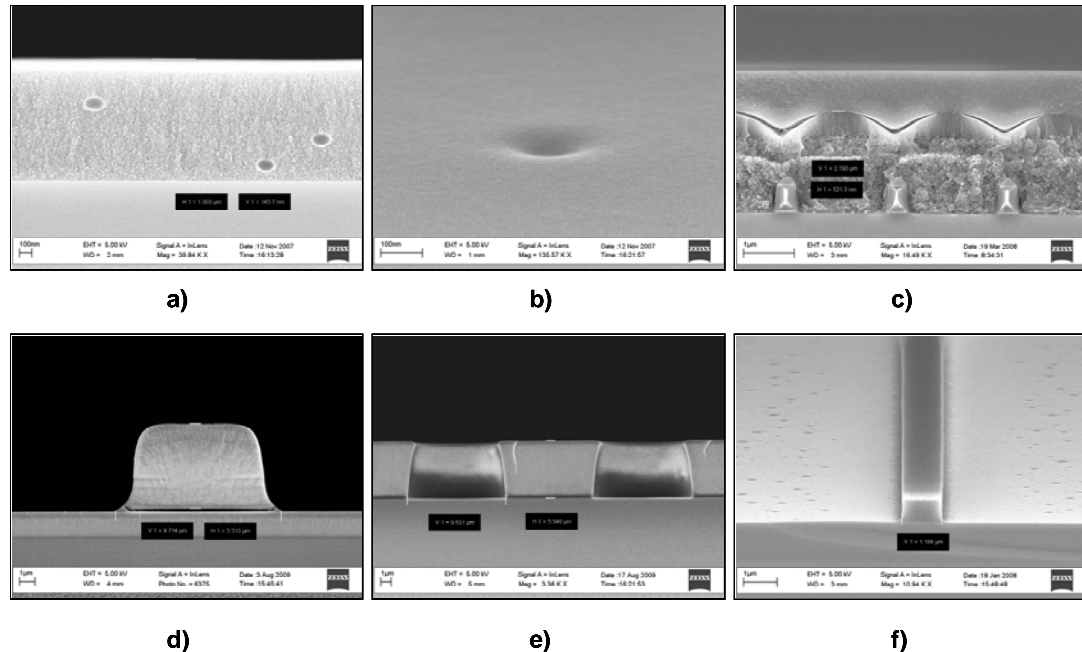

Figure 11-7. SEM images of the various issues encountered with photopatternable polymers: a) voids b) pits c) delamination d) footing e) undercutting f) residues or scum.

While the microlens overcoat application does not require very high resolution as the pad areas to be defined can be several tens of micrometers wide, the issues illustrated in Figure 11-7 are unacceptable. Voiding and pitting typically seen with using inappropriate photoinitiators or too high concentrations of them can affect the propagation of light and degrade the sensor's light collection efficiency. Additionally, the passivation capability of the overcoat layer can be compromised. Poor adhesion leading to degraded performance may be the result of having a large difference between the coefficients of thermal expansion (CTE) or due to chemical incompatibility between the overcoat and microlens layers. Footing and undercutting seen in the pattern sidewall profiles are undesirable as they can complicate the subsequent metal deposition process. Residual polymer on the pads can lead to poor electrical contacts if not removed with a proper cleaning or de-scum step. By optimizing the polymer composition, photoinitiator and process conditions it is possible to achieve a polymer which fills the application requirements and has excellent photopatternability. Figure 11-8 displays SEM images from such an optimized material with good pattern profile and adhesion to the microlens layer. [50, 51, 53]

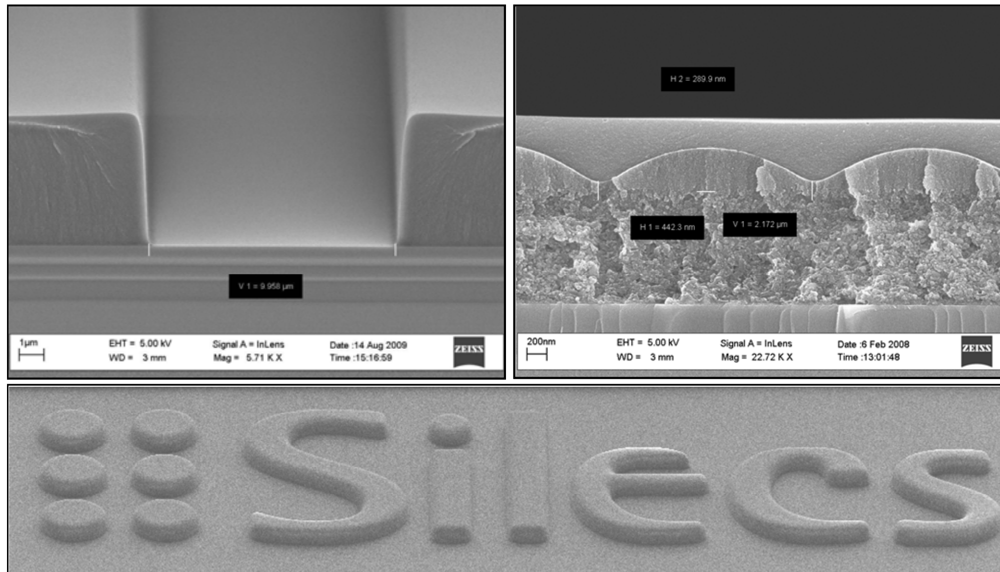

Figure 11-8. SEM images from an optimized photopatternable overcoat material.

Low refractive index, high transparency in the visible spectrum and photopatterning capability makes Silecs' siloxane based spin-on polymers highly attractive to the microlens overcoat application. The films can be cured well below the thermal degradation point of typical microlens and color filter materials and provide excellent protection to the lens array. Lower reflectance leading to higher light collection efficiency can also be achieved.

12 Stability of polymer films

During their lifetime image sensors are exposed to solar radiation as well as to changes in temperature and humidity conditions. Solar radiation and especially the high energy UV portion of the electromagnetic spectrum can cause changes in polymer material properties leading to changes in device performance. Compared to other applications such as solar panels the image sensor is however exposed to sunlight only for very short periods of time during the image exposure cycle. Most of the time, the sensor is protected from sunlight by either a mechanical shutter or a lens cap. Also the optical glass used in camera lenses does not typically transmit light at below 350 nm wavelength providing efficient UV-light protection for the image sensor.

The effects of solar radiation on Silecs SC-series polymer film properties were investigated by exposing the films to direct UV light up to 96 hours. The films were also subjected up to 96 hours to increased temperature and humidity conditions during the industry standard 85/85 test to find out how readily they absorb moisture. Although the four day test period is a relatively short one, the test performed was considered to be quite aggressive since the films coated and cured on bare silicon wafers were directly exposed to the conditions without any protective layers on top as would be the case in real life. The solar radiation test was performed according to SFS-EN ISO 4892-3 by exposing the films to UV radiation with 100 ± 5 W/m^2 intensity peaking at approximately 335 nm wavelength. The ambient temperature was kept at 40 ± 2°C. The solar radiation received by the samples during the 24h and 96h time periods corresponds to the mean solar radiation energy received in southern Finland during 0.5 and 2.1 months, respectively. The 85/85 test was performed in an ESPEC type PR-4KP test chamber at 85°C temperature and 85% relative humidity according to the IEC60068-2-67 standard. The thickness and refractive indices of the films were measured after the cure and after 24h and 96h exposure to the test conditions. Figure 12-1 shows a summary of the results for the SC300, SC400 and SC800 films.

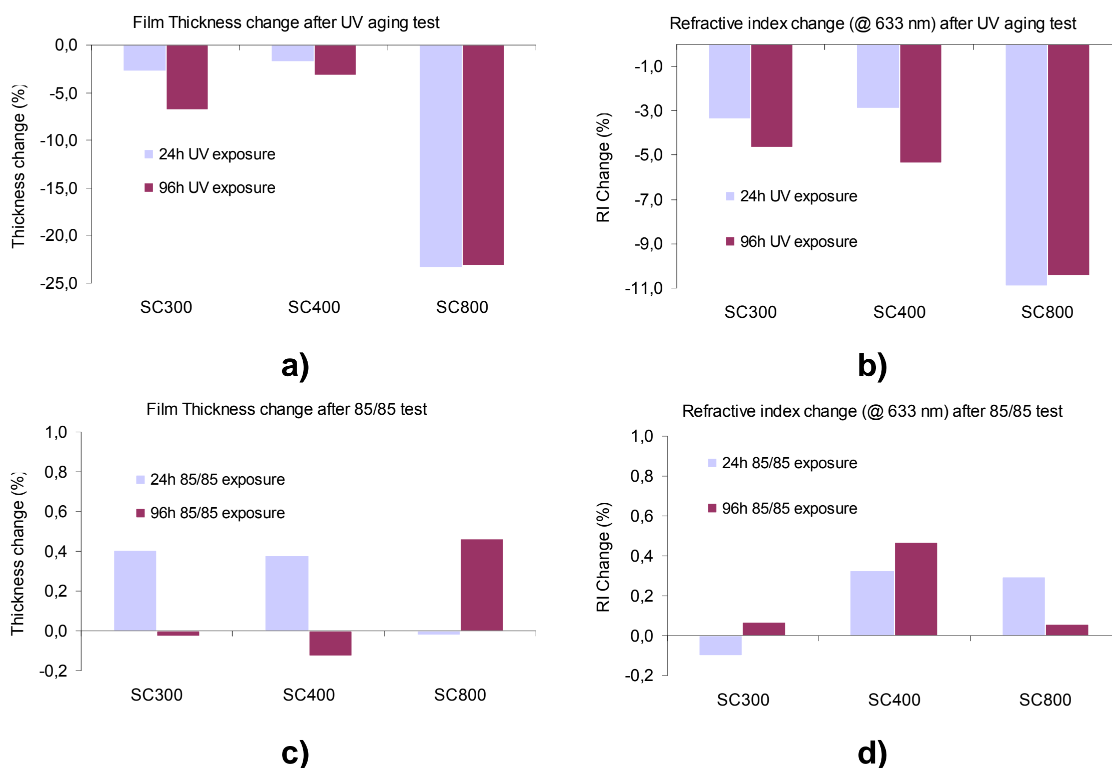

Figure 12-1. SC300, SC400 and SC800 film thickness and refractive index change during environmental testing.

As seen from Figure 12-1 (a) and (b), both the film thickness and refractive index of the SC300, SC400 and SC800 materials decrease upon prolonged exposure to UV-light. The SC300 and SC400 have a fairly similar response which can be explained by the relatively similar composition of the polymers. Some thickness decrease in the range of a few tens of nanometers was measured as well as a decrease in the refractive index of the film. A fourier transform infrared spectroscopy (FTIR) measurement revealed also changes in the absorption spectra indicating that there was some amount of decomposition occurring during the UV-light exposure. A portion of the networked siloxane (Si-O-Si) bonds had been broken and replaced by silanols (Si-OH). The SC800 was found to have the most significant changes in film thickness and refractive index due to UV exposure. This result is in line with the transmittance data shown in Figure 10-5 where the SC800 can be seen to have increased absorption at wavelengths of 400 nm and below. Figure 12-1 (c) and (d) show the changes in film thickness and refractive index after exposure to increased temperature and humidity conditions. The thickness changes can be considered insignificant as only up to 3 nm differences in film thickness before and after the 85/85 test were measured. The refractive index showed slight increase suggesting that some moisture absorption may have

occurred. The differences in film thickness and refractive indices were however so small that the measurement tool variation is likely to bring some error into the results.

The effects of UV radiation and increased temperature and humidity conditions were tested also for the SC200 and SC500 overcoat materials. The experiments were performed similarly to the lightpipe materials. Figure 12-2 below shows a summary of the results.

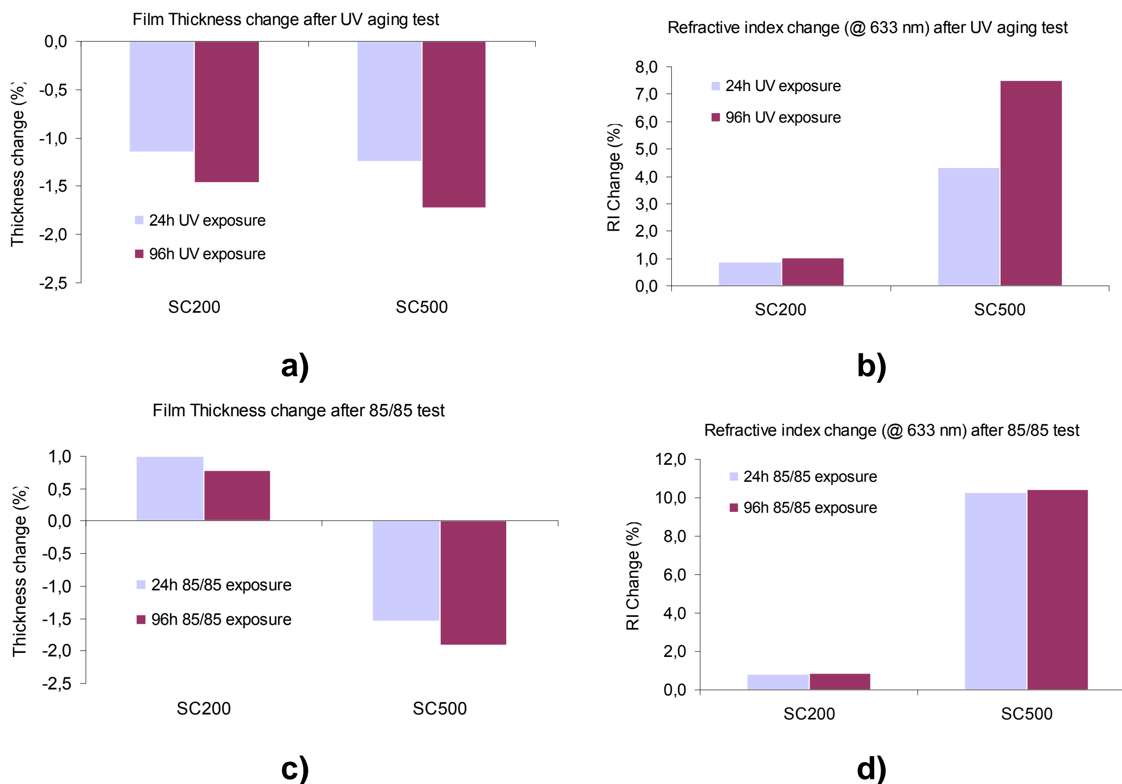

Figure 12-2. SC200 and SC500 film thickness and refractive index change during environmental testing.

During the exposure to UV-light, the SC200 and SC500 films lost less than 2% of their original thickness as shown in Figure 12-2 (a). The refractive index, however, increased especially with the SC500 whereas the SC200 remained within 1% of the original value measured after curing. The SC500 can clearly be seen as more sensitive to UV-radiation compared to the SC200 although no major changes were detected in the FTIR analysis. The 85/85 test showed minor changes in film thickness and refractive index for SC200 but significant changes especially in the refractive index for the SC500. This indicates that the SC500 material has a higher

degree of porosity compared to the SC200 allowing it to absorb water which then increases the refractive index of the film.

Overall, the SC300 and SC400 materials were found to behave very similarly in the solar radiation test while the SC800 showed clearly stronger response to the UV-light most likely due to the presence of the metal oxide nanoparticles. The 85/85 test did not cause significant changes in the film properties indicating very low or negligible moisture absorption. The overcoat material SC200 was found to be very insensitive to both UV-light and increased temperature and humidity conditions, while the SC500 showed some changes especially in the refractive index. Although the environmental test data presented in this chapter cannot be used as a direct indicator of how the films would behave in the actual image sensor application, the results can be used as a reference point for future work.

13 Summary

The fundamental laws of optics focusing especially on the behavior of light at an interface of two or more transparent layers were presented. Snell's law was used to demonstrate how the direction of light arriving at a plane interface of two optically dissimilar materials can be controlled by adjusting the refractive indices. Total internal reflection, in which case all light is reflected, was found to occur when light arrives at an interface from a layer with a higher refractive index to a layer with a lower refractive index. The angle of incidence has to however exceed the critical angle or otherwise some of the light will be transmitted across the interface. This phenomenon has found many uses in optical applications such as optical fibers and planar waveguides where light is guided along a high refractive index core and used to carry information across long distances. The reflectance of light was shown to be highly dependent on the angle of incidence and the refractive index of the media on both sides of the interface. An anti-reflection coating with a specifically tuned refractive index and film thickness can be used to completely eliminate the reflecting wave through destructive interference. In this case all light is transmitted and passed through the interface. A single layer anti-reflective coating is able to eliminate reflections at a specific wavelength only where as multiple layers with alternating high and low refractive indices can be used to reduce the reflections at a broader wavelength range. The same principle can also be used to create a highly reflecting surface by simply adjusting the layer thicknesses and refractive indices. Scattering and absorption were found to attenuate the signal intensity of the propagating wave via redirecting it from its original direction or by converting it to heat. The concept of total internal reflection was further discussed with the fundamentals of optical fibers. The modes of propagation and the evanescent wave traveling parallel to the core-cladding interface were examined along with the conditions needed to transport light inside a step-index fiber.

The photoelectric effect in which photons are converted into electrons was introduced and an example of its practical use in detecting light with silicon based technologies was given. The basic structures of photodiodes and photogates and how they are used to convert light into an electrical signal in modern image sensors were explained. The charge coupled device and the complementary metal oxide semiconductor based structure, which are two of the most widely used image sensor types in digital imaging, were reviewed in order to establish an understanding of their basic operation and characteristics. Both have an array of photoactive sites or pixels used to detect light and generate a signal but the way the signal is collected and the structure of the detector is different. The charge coupled device was found to have the advantage of better image quality and low noise while the complementary metal oxide semiconductor based sensor consumes less power and can be integrated with other functionalities. Both

technologies are used today in scientific, industrial and commercial applications. Some of the parameters used to define the sensor performance such as sensitivity and spectral response were reviewed and the effects of pixel downscaling to the sensor performance analyzed. Smaller pixels were shown to have better spatial resolution but at the same time suffer from lower sensitivity and higher noise as it is becoming increasingly difficult to collect light when the pixel dimensions approach the wavelength of light. The use of new integration schemes such as lightpipes and backside illumination were shown to significantly increase the performance of small pixel size sensors.

Optical modeling was used to demonstrate the difficulties arising from pixel size reduction and prove the feasibility of a high refractive index lightpipe especially in small pixel size sensors. The lightpipe was shown to effectively increase the amount of light reaching the photodiode thus increasing the sensor performance. Light incident at off-axis angles was effectively guided by the lightpipe due to total internal reflection which both increased the amount of light reaching the photodiode and reduced crosstalk between pixels. A comparison between various lightpipe structures was made and the high refractive index core approach was found to be the most effective one. The effect of a microlens overcoat layer was also modeled and shown to improve the sensor performance especially for off-axis light.

Siloxane based spin-on polymers and the advantages they can offer to CMOS image sensors were presented. Silecs's high refractive index polymers and their fundamental properties demonstrating their suitability for the lightpipe application were introduced. A high refractive index lightpipe structure in an IBM 2.2 μm pixel size sensor utilizing Silecs' spin-on polymer material was demonstrated to guide light more efficiently to the photodiode thus increasing the image sensor performance. Higher quantum efficiency and lower crosstalk were measured compared to the conventional structure with a standard dielectric stack above the photodiode. The SC400 polymer also outperformed the lower refractive index organic polymer which has previously been reported by IBM. The increased performance resulted mainly from the high refractive index and excellent optical transparency of the SC400 polymer. Additionally, deposition by spin-on coating provides a high degree of planarization and excellent gapfill along with high wafer throughput making it ideal also for high volume production. The ultra-high refractive index polymer SC800 was also tested but the sensor quantum efficiency was found to decrease due to insufficient transparency especially at shorter wavelengths. An increase in the angular response was however detected showing that a higher refractive index can be used to increase sensor performance provided that the transparency is sufficiently high. The feasibility of using spin-on siloxane based polymers for microlens overcoat application was also studied. A low refractive index film such as the SC500 was found to act as an effective anti-reflection coating, while at the same time providing mechanical protection to the soft lens

structure. This results in both improved performance and higher die yield. Moreover, a photosensitized polymer offers process simplification as the pad areas can be defined by direct photopatterning rather than using conventional technology relying on photoresist and etch processes for pattern transfer.

14 Conclusions

Despite their improved resolution and small die size resulting in lower cost and reduced power consumption, small pixel image sensors suffer from lower sensitivity and higher crosstalk compared to sensors with large pixels. In order to maintain good performance, new structural pixel design solutions such as the lightpipe and backside illumination have been implemented. The lightpipe extends the usability of the conventional frontside illuminated sensor by guiding the incident light more efficiently to the photodiode. Backside illumination relies on a completely different type of approach where the dielectric stack and metal layers have been removed from the optical path which in turn increases the amount of light reaching the photodiode. The lightpipe and backside illuminations concepts are especially beneficial for image sensors with small pixel sizes used typically in mobile phone applications. For image sensors found in digital still cameras, the chip size is not as critical as there are less space constraints allowing the use of larger pixel sizes with a conventional dielectric stack structure. It is likely that the mobile phone application with continuously decreasing pixel size remains as the main application for the CIS while the CCD type sensor continues to be used mainly in DSC applications.

Both the frontside illuminated sensor with a lightpipe structure and the backside illumination approach are currently used to mass produce 1.4 µm pixel size sensors with comparable performance and it remains to be seen which technology will be the first to reach and extend beyond the 1.0 µm pixel size limit. The frontside illuminated sensor with a high refractive index lightpipe is likely to remain as a highly attractive solution since it does not require significant modifications to the conventional image sensor manufacturing flow and is cheaper to manufacture compared to the BSI sensor. Although the Silecs SC400 polymer was demonstrated to give significant improvement to sensor performance and is currently used in manufacturing state-of-the art image sensors, development of even higher refractive index materials is required in order to be able to compete with the backside illuminated structure. The ultra-high refractive index SC800 polymer remains to be a viable candidate but needs to be further developed to increase the film's optical transparency. Such an ultra-high refractive index film is also required in the back-side illuminated architecture as an anti-reflection coating on silicon. As it turns out, a film with a refractive index in the range of 1.8-2.0 could be used to improve the performance of both FSI and BSI sensors. A CVD type process for depositing for example silicon nitride which has a sufficiently high refractive index and good transparency cannot be used in either case due to poor gapfill and high deposition temperature. Therefore a high refractive index spin-on polymer with a curing temperature in the range of 300-400°C remains as a highly attractive product and one of the key focus areas of Silecs' material development.

Low refractive index materials such as the SC500 are also needed in both FSI and BSI architectures as a microlens overcoat layer. Although a CVD process can achieve highly conformal coatings, it cannot produce a film with low enough refractive indices required to reduce reflections from the microlens surface. Additionally, siloxane based spin-on polymers offer the possibility of direct photopatterning which eliminates the need for standard resist and etch processes. This functionality is highly beneficial for both ultra-high and low refractive index polymers.

References

[1] Kenyon, I. The light fantastic, a modern introduction to classical and quantum optics. Oxford, Oxford University Press, 2008.

[2] Harris, R. Modern physics. 2nd edition. San Francisco, Pearson Addison-Wesley, 2008.

[3] http://serc.carleton.edu/images/quantskills/methods/e-m_spectrum.gif accessed 16.5.09.

[4] Sihvola, A. Lindell, I. Sähkömagneettinen kenttäteoria 2. Dynaamiset kentät. Otatieto, 2004.

[5] http://www.corning.com/docs/specialtymaterials/pisheets/H0607_hpfs _Standard_ProductSheet.pdf. accessed 21.5.09.

[6] http://www.islandnet.com/~see/weather/almanac/arc2008/alm08oct.htm. accessed 24.5.09.

[7] Kaivola, M. Tfy-125.4321 Laser Technology and Optics lecture notes, Helsinki University of Technology, 2009.

[8] Nakamura, J. Image sensors and signal processing for digital still cameras. Boca Raton, Taylor & Francis Group, 2006.

[9] The Evolution of Digital Imaging: From CCD to CMOS. A Micron white paper http://www.ericfossum.com/Articles/Cumulative%20Articles%20about%20EF/Micron%20White%20Paper%20on%20CCDs%20and%20CMOS.pdf. accessed 17.6.2009.

[10] Bigas, M. Cabruja, E. Forest, J. Salvi, J. Review of CMOS image sensors. Microelectronics Journal 37 (2006) 433–451.

[11] Blanksby, A. Loinaz, M. Performance analysis of a color CMOS photogate image sensor. IEEE Transactions on electron devices, VOL 47, NO. 1, January 2000.

[12] Litwiller, D. CMOS vs. CCD: Maturing Technologies, Maturing Markets. Photonics Spectra, August 2005.

[13] Mathur, S. Okincha, M. Walters, M. What Camera Manufacturers Want. 2007 International Image Sensor Workshop. Ogunquit Maine, USA June 7-10, 2007.

[14] Adkisson, J. Gambino, J. Hoague, T. Jaffe, M. Kyan, J. Leidy, R. McGrath, D. Rassel, R. Sackett, D. Stancampiano, C. V. Optimization of Cu Interconnect Layers for 2.7 µm Pixel Image Sensor Technology: Fabrication, Modeling, and Optical Results. Electron Devices Meeting, 2006. IEDM ’06. International, 11-13 Dec. 2006 Page(s):1 – 4.

[15] Oh, H.S. Hong, H.J. Lee, J.I, Park, S.J. Kwon, K.K. Hwang, J. Enhancement of Wafer Test/Package Yields by Oxide-Capping of Microlens in CMOS Image Sensor ASICs, 2000. AP-ASIC 2000. Proceedings of the Second IEEE Asia Pacific Conference, 28-30 Aug. 2000.

[16] Agranov, G. Berezin, V. Tsai, R.H. Crosstalk and Microlens Study in a Color CMOS Image Sensor. IEEE Transactions on Electron Devices, VOL. 50, NO. 1, January 2003.

[17] Rhodes, H. Agranov, G. Hong, C. Boettiger, U. Mauritzson, R. Ladd, J. Karasev, I. McKee, J. Jenkins, E. Quinlin, W. Patrick, I. Li, J. Fan, X. Panicacci, R. Smith, S. Mouli, C. Bruce, J. CMOS Imager Technology Shrinks and Image Performance. Microelectronics and Electron Devices, 2004 IEEE Workshop. 2004.

[18] El Gamal, A. Eltoukhy, H. CMOS Image Sensors. An Introduction to the technology, design and performance limits, presenting recent developments and future directions. IEEE Circuits & Devices Magazine, May/June 2005.

[19] Cohen, M. Roy, F. Herault, D. Cazaux, Y. Gandolfi, A. Reynard, JP. Cowache, C. Bruno, E. Girault, T. Vaillant, J. Barbier, F. Sanchez, Y. Hotellier, N. LeBorgne, O. Augier, C. Inard, A. Jagueneau, T. Zinck, C. Michailos, J. Mazaleyrat, E. Fully Optimized Cu based Process with Dedicated Cavity Etch for 1.75µm and 1.45µm pixel pitch CMOS Image Sensors. Electron Devices Meeting, 2006. IEDM ’06. International, 11-13 Dec. 2006 Page(s):1 – 4.

[20] Holst, G.C. CCD Arrays, Cameras and Displays. Winter Park, Florida. JCD Publishing. Bellingham, Washington. SPIE Optical engineering press, 1996.

[21] Gambino, J. Leidy, B. Watts, A. Musante, C. Ackerson, K. Mongeon, S. Adkisson, J. Rassel, R.J. Ogg, K. Ellis-Monaghan, J. Jaffe, M. Laukkanen, M. Karaste, K. McLaughlin, W. Gädda, T. Rantala, J. CMOS image sensor with high refractive index lightpipe. 2009 International Image Sensor Workshop (IISW), Bergen, Norway, June 26th 2009.

[22] Hakkarainen, T. S-104.3310 Optoelectronics lecture notes, Helsinki University of Technology, 2009.

[23] Coghill, J. Digital Imaging Technology 101. https://classes.yale.edu/04-05/enas627b/lectures/EENG427l07DigitalImaging.pdf. accessed 13.7.2009.

[24] Kasap, S.O. Optoelectronics and Photonics: Principles and Practices. Upper Saddle River, NJ., Prentice Hall, 2001.

[25] Image Sensor Architectures for Digital Cinematography. http://www.dalsa.com/public/dc/documents/Image_Sensor_Architecture_Whitepaper_Digital_Cinema_00218-00_03-70.pdf. accessed 24.8.2009.

[26] Iwabuchi, S. Maruyama, Y. Ohgishi, Y. Muramatsu, M. Karasawa, N. Hirayama, T.
A Back-Illuminated High-Sensitivity Small-Pixel Color CMOS Image Sensor with Flexible Layout of Metal Wiring. 2006 IEEE International Solid-State Circuits Conference.

[27] Joy, T. Pyo, S. Park, S. Choi, C. Palsule, C. Han, H. Feng, C. Lee, S. McKee, J. Altice, P. Hong, C. Boemler, C. Hynecek, J. Louie, M. Lee, J. Kim, D. Haddad, H. Pain, B. Development of a Production-Ready, Back-Illuminated CMOS Image Sensor with Small Pixels. Electron Devices Meeting, 2007. IEDM 2007. IEEE International., 10-12 Dec 2007.

[28] Prima, J. Roy, F. Coudrain, P. Gagnard, X. Segura, J. Cazaux, Y. Herault, D. Virollet, N. Moussy, N. Giffard, B. Gidon, P. A 3Mega-Pixel back-illuminated sensor in 1T5 architecture with 1.45μm pixel pitch. 2007 International Image Sensor Workshop. Ogunquit Maine, USA June 7-10, 2007.

[29] Gambino, J. Ackerson, K. Guthrie, B. Leidy, B. Adabeer, W. Mongeon, S. Meatyard, D. Adkisson, J. Rassel, R.J. Ellis-Monaghan, J. Jaffe, M. Reliability of CMOS image sensor with polymer lightpipe. 2007 International Image Sensor Workshop. Ogunquit Maine, USA June 7-10, 2007.

[30] Hsu, T.H. Fang, Y.K. Lin, Y. Chen, S.F. Lin, C.S. Yaung, D.N. Wuu, S.G. Chien, H.C. Tseng, C.H. Lin, J.S. Wang, C.S. Light Guide for Pixel Crosstalk Improvement in Deep Submicron CMOS Image Sensor. IEEE Electron Device Letters, VOL. 25, No. 1, January 2004.

[31] Hsu, T.H. Fang, Y.K. Yaung, D.N. Wuu, S.G. Chien, Wang, C.S. Lin, J.S. Tseng, C.H. Chen, S.F. Color Mixing Improvement of CMOS Image Sensor With Air-Gap-Guard Ring in Deep-Submicrometer CMOS Technology. IEEE Electron Device Letters, VOL. 26, No. 5, May 2005.

[32] Lee, J.S. McKee, J.A. Mouli, C. Method and Apparatus Providing and Optical Guide in Image Sensor Devices. United States Patent US 7,511,257 B2. Mar 31. 2009.

[33] Adkisson, J.W. Gambino, J.P. Jaffe, M.D. Leidy, R.K. Rassel, R.J, Stamper, A.K. CMOS Imager with Cu Wiring and Method of Eliminating High Reflectivitty Interfaces Therefrom. United States Patent US 2008/0108170 A1. May 8. 2008.

[34] Yamamoto, K. Image Sensor Having Micro-Lenses With Integrated Color Filter and Method of Making. United States Patent US 2005/0098842 A1. May 12. 2005.

[35] Komoguchi, T. Enomoto, Y. Solid-State Imaging Device and Production Method Therefor. United States Patent US 7,442,973 B2. Oct. 28, 2008.

[36] Olkkonen, J. Hiltunen, M. FDTD modeling of CMOS image sensors. Valtion Teknillinen Tutkimuskeskus, 2008.

[37] Ciccarelli, A. Davis, B. Des Jardin, W. Doan, H. Meisenzahl, E. Pace, L. Putnam, G. Shepherd, J. Stevens, E. Summa, J. Wetzel, K. Front-illuminated full-frame charge-coupled device image sensor achieves 85% peak quantum efficiency. Eastman Kodak Company, Rochester, NY.

[38] http://www.sony.net/sonyinfo/news/press. accessed 17.7.2009.

[39] Norris, A. DeGroot, J. Kowalczyk, T. Baugher, A. Blum, R. Ogawa, T. Watanabe, T. Siloxane Materials with High Reliability for Use as Polymer Waveguides. http://www.dowcorning.com. Accessed 13.9.2009.

[40] Norris, A. DeGroot, J. Nishida, F. Pernisz, U. Kushibiki, N. Ogawa, T. Silicone Materials for Optical Applications. http://www.dowcorning.com. Accessed 13.9.2009.

[41] Wang, C-C. A Study of CMOS Technologies for Image Sensor Applications. Massachusetts Institute of Technology. 2001.

[42] Reznik, H. Edelstein R.S, Shach-Caplan, M. Dulberg, F. Kamenetzky V. Karaste, K. Rantala J.T. Integration and characterization of spin on dielectric materials in image sensor devices. Photonics in Multimedia II, Proceedings of SPIE volume 7001. 28.5.2008.

[43] Yoshikawa, H. Kawasaki, A. Iiduka, T. Nishimura, Y. Tanida, K. Akiyama, K. Sekiguchi, M. Matsuo, M. Fukuchi, S. Takahashi, K. Chip Scale Camera Module (CSCM) Using Through-Silicon-Via (TSV). 2009 IEEE International Solid-State Circuits Conference. 8-12 Feb, 2009.

[44] Theuwissen, A. CMOS Image Sensors: State-Of-The-Art and Future Perspectives. Solid State Device Research Conference, 11-13 Sept. 2007, pages: 21-27.

[45] Sumi, H. Low-Noise Imaging System with CMOS Sensor for High-Quality Imaging. Electron Devices Meeting. 11-13 Dec. 2006, pages: 1-4.

[46] Fesenmaier, C. Catrysse, P. Mitigation of pixel scaling effects in CMOS image sensors. Proc. of SPIE-IS&T Electronic Imaging, 2008.

[47] Nakayama, N. Hayashi, T. Preparation and Characterization of TiO_2 and Polymer Nanocomposite Films with High Refractive Index. Journal of Applied Polymer Science, Vol. 105, 3662-3672, 2007.

[48] Schnabel, W. Polymers and Light, Fundamentals and Technical Applications. Weinheim, Wiley-VCH Verlag GmbH & Co. KGaA, 2007.

[49] Rantala, J. Semiconductor Optoelectronic Devices. World Intellectual Property Organization, International publication number WO 2007/144371 A2, 21.12.2007.

[50] Junarsa, I. Stoykovich, M.P. Nealey, P. F. Ma, Y. Cerrina, F. Hydrogen silsesquioxane as a high resolution negative-tone resist for extreme ultraviolet lithography. J. Vac. Sci. Technol. B 23(1), Jan/Feb 2005.

[51] Wang, P-I. Nalamasu, O. Ghoshal, R. Ghoshal, R. Schaper, C. Li, A. Lu, T-M. Novel photocurable epoxy siloxane polymers for photolithography and imprint lithography applications. J. Vac. Sci. Technol. B 26(1), Jan/Feb 2008.

[52] Mont, F.W. Kim, J.K. Schubert, M.F. Schubert, E.F. Siegel, R.W. High-refractive-indec TiO_2-nanoparticle-loaded encapsulants for light-emitting diodes. Journal of Applied Physics 103, 2008.

[53] Licari, J.J. Coating Materials for Electronic Applications. Norwich, New York, William Andrew Publishing, 2003.

[54] http://www.toshiba.com/taec/news/media_resources/news_mr_gallery.jsp accessed 14.10.2009.